FACULTY OF SCIENCE AND TECHNOLOGY

MASTER'S THESIS

Study programme:
Marine and Offshore Technology

The spring semester, 2023

Open / ~~Confidential~~

Author:
Dennis Beier

Supervisor: Prof. Muk Chen Ong
Co-supervisors: Marek Jan Janocha, PhD; Naiquan Ye, PhD

Thesis title:
Dynamic and Fatigue Analyses of Suspended Power Cables for Multiple Floating Offshore Wind Turbines

Credits (ECTS): 30

Keywords: inter-array power cable, suspended cable, floating offshore wind turbine, fatigue analysis, OrcaFlex

Pages: 115

Stavanger, 11.06.2023

Abstract

Floating offshore wind turbines (FOWTs) are installed to effectively capture energy from offshore wind in deeper water areas where building bottom-fixed offshore wind turbines is not practical. The present study focuses on the application and fatigue life of suspended inter-array power cables in floating offshore wind farms. A spar type and a semi-submersible type FOWTs are modeled in the dynamic analysis software OrcaFlex and validated against reference studies. The power cable connecting the FOWTs is installed fully suspended with attached buoys. The impacts of marine growth on the power cable and the non-linear bending behavior of the cable are considered in the analyses. Representative environmental conditions for the North Sea are applied to assess the dynamic responses of the model. Different cable configurations connecting two spar FOWTs are evaluated based on Fitness Factors using static and dynamic analyses. The number of buoys is identified as the main parameter determining the maximum effective tension and the minimum bending radii of the cables. The vertical excursion of the suspended cable depends on the buoy spacing. The effect of cable length and marine growth on cable tensions and curvatures is small. Two semi-submersible FOWTs are connected using the most suitable cable configuration obtained for the two spar FOWTs. The impact of the floater type on the tension and curvature of the power cable is determined to be very small. A two-turbine configuration with various environmental load directions is identified to be representative of the suspended power cables design in whole wind farms, according to analyses of power cable behavior in various offshore wind farm layouts. To investigate the fatigue life of the power cable, the relationships between the axial tensions and curvatures of the power cable and its stresses are obtained by cross-section analysis in UFLEX. The optimum cable in the spar setup has a fatigue life of 85 years, with curvature-induced stresses being identified as the primary cause of the fatigue damage. The power cable's fatigue life reduces when marine growth effects are considered. A decrease in the number of buoys attached to the cable and the use of semi-submersible FOWTs increase the fatigue life. The armor wires are the critical components, and the highest fatigue damage always occurs adjacent to the buoys. The largest fatigue damage results from environmental loads approaching the power cable from a crossflow direction.

Acknowledgments

I would like to thank my supervisor Professor Muk Chen Ong for his guidance and help during the entire master thesis project. Completing this work without his support would not have been possible.

I would also like to thank Post-Doctoral Researcher Marek Jan Janocha for his advice and support in carrying out the simulations and for editing the papers related to this master thesis.

I would like to acknowledge Naiquan Ye from SINTEF Ocean for his support in the use of UFLEX as well as for providing and checking information about the power cable.

I would like to thank Izwan Bin Ahmad who has previously worked on this topic at UiS for his help with the OrcaFlex model as well as for sharing his Python codes with me.

Also, I would like to express my gratitude for the great companionship and support from my fellow students during the entire master's degree program.

Last, but not least I would like to thank my family for their infinite love and support during all my life.

Table of Contents

List of Figures

List of Tables

Chapter 1 - Introduction

In this chapter, the background and motivation for the topic, the objectives of this work, and an outline of the thesis are provided.

1.1 Background and Motivation

In the Paris Climate Agreement (United Nations, 2015) the member states of the United Nations agreed to limit global warming by reducing greenhouse gas emissions. The use of renewable energy sources, such as wind, instead of fossil energy sources will be a key parameter to achieve this goal. Offshore wind farms differ from onshore wind farms by higher average wind speeds, a lower environmental impact, no restrictions due to populated areas and the possibility for larger turbines. The demand for offshore wind turbines is expected to increase significantly in the future (GWEC Global Wind Energy Council, 2022b). Currently, the majority of the existing offshore wind farms consists of bottom-fixed wind turbines. However, these concepts are not suitable for projects in deeper water. Therefore, FOWTs will be used for deeper water locations. Figure 1-1 shows several different proposed FOWT concepts. The barge concept consists of a concrete or steel hull and maintains its stability through distributed buoyancy and a large waterplane area. Semi-submersible FOWTs are made of several partially submerged columnar tubes. The spar concept consists of a long cylinder and is very stable due to its low center of gravity. These three substructures have in common that they are kept in position using catenary mooring lines. The tension-leg-platform (TLP) concept is anchored to the seabed by taut vertical tendons, limiting the pitch and roll motions.

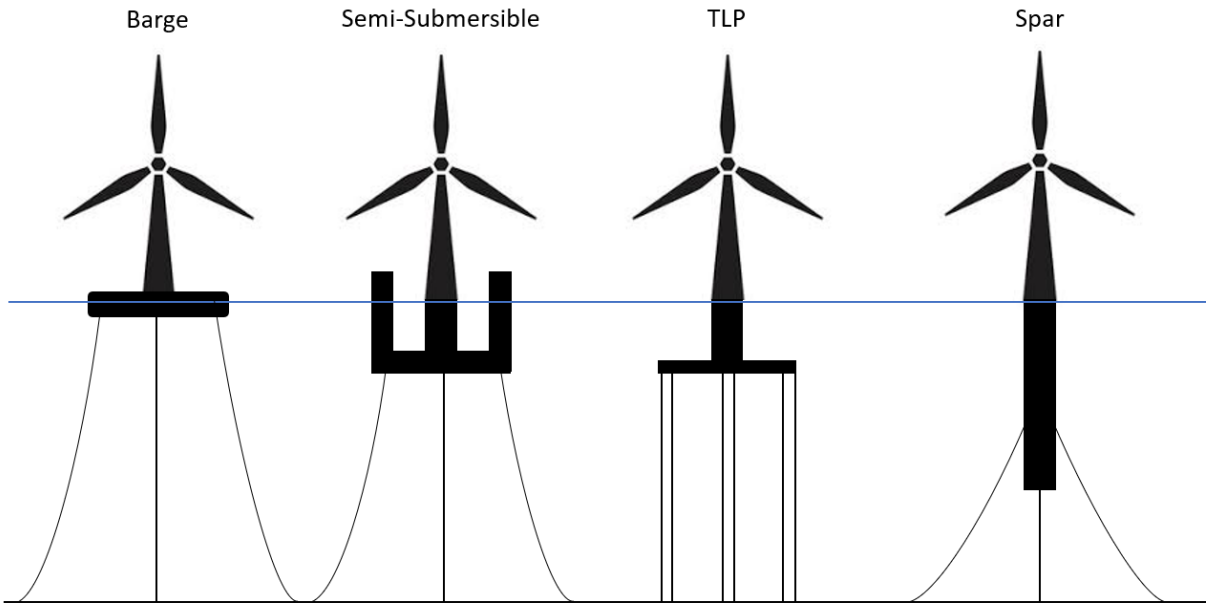

Figure 1-1: FOWT concepts.

Some projects with FOWTs have already been implemented, including the wind farms Hywind Scotland (Eldøy, 2017), WindFloat Atlantic (Principle Power Inc., 2022) and Hywind Tampen (Equinor ASA, 2019). Recently, an increasing number of areas with deeper water is included in the concession rounds for offshore wind farm licenses, e.g. Utsira Nord (Olje- og energidepartementet, 2023) and several parts of ScotWind (Crown Estate Scotland, 2023). As a result, the improvement of FOWT farms will be very important. One possible improvement measure is to reduce the length of the inter-array power cables by directly connecting the FOWTs with suspended cables. Figure 1-2 shows several possible inter-array power cable configurations for FOWTs. The currently most common types are the catenary and the lazy-wave shape (Ikhennicheu et al., 2020). For both shapes, the cables are laid on the seabed, resulting in long cable lengths for large water depths. The lazy-wave configuration differs from the catenary configuration due to an attached buoyancy section, aiming at a reduction in the cable tension. In a suspended configuration, several buoys are used to keep the cable floating at a specific depth and to limit the maximum cable tension.

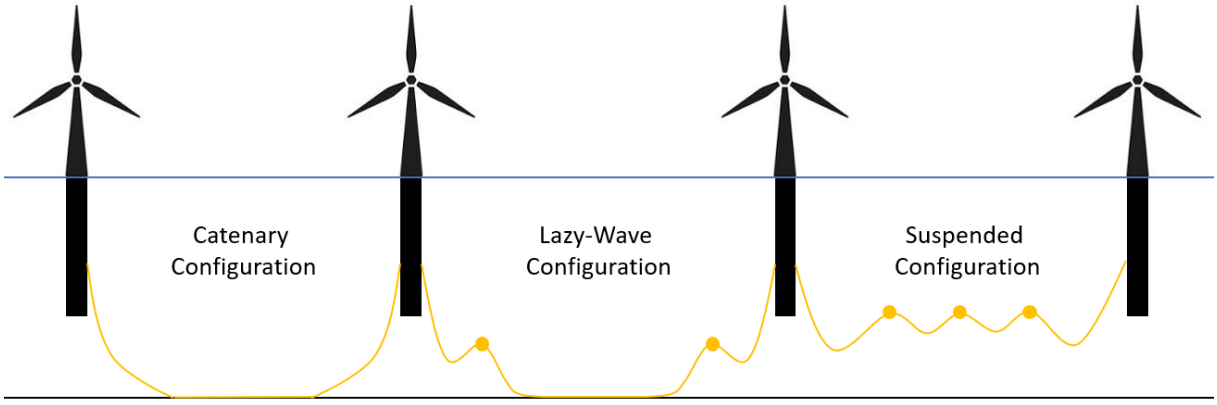

Figure 1-2: Power cable configurations for FOWTs.

1.2 Objectives

In this master thesis, the optimum configuration of buoys and the optimum length for a real dynamic offshore power cable connecting two FOWTs suspended should be determined. Also, the marine growth effects on the power cable should be considered in the investigation. Moreover, the effects of different types of floaters on the suspended power cable should be elaborated and the influences on power cables connecting multiple floaters, like in a realistic wind farm, should be investigated. Added to that, the fatigue life of the suspended power cable for exemplary environmental conditions should be assessed.

1.3 Master Thesis Structure

The master thesis is organized as follows:

- **Chapter 1 – Introduction:**
  This chapter contains the context of the topic and the motivation for the thesis as well as the objectives and the structure of the work.

- **Chapter 2 – Theory:**
  This chapter demonstrates the system theory for FOWTs and offshore power cables. It presents the theory of environmental conditions and the fatigue assessment.

- **Chapter 3 – Methodology and Numerical Setup:**

  In this chapter, the numerical setup of the FOWTs and the suspended inter-array power cable is explained. The applied environmental conditions and marine growth effects are described. Also, the procedure of the case study including the fatigue assessment procedure is explained.

- **Chapter 4 – Application of a Suspended Inter-Array Power Cable in Floating Offshore Wind Farms:**

  This chapter presents the case study of the suspended power cable application in FOWT farms. The chapter is under reviews as:

  Beier, D., Ong, M. C., Janocha, M. J., & Ye, N. (2023). Application of a Suspended Inter-Array Power Cable in Floating Offshore Wind Farms.

- **Chapter 5 – Fatigue Assessment of a Suspended Offshore Power Cable in Floating Offshore Wind Farms:**

  In this chapter, the fatigue assessments for different suspended power cable setups are presented. This chapter is under review as:

  Beier, D., Janocha, M. J., & Ye, N., Ong, M. C. (2023). Fatigue Assessment of Suspended Inter-Array Power Cables for Floating Offshore Wind Turbines.

- **Chapter 6 – Conclusions:**

  This chapter contains a summary of the thesis as well as the conclusions of the work.

- **Chapter 7 – Recommendations for Future Works:**

  In this chapter, recommendations for future studies related to this topic are elaborated.

Chapter 2 - Theory

A fundamental understanding of the entire system is required to comprehend the dynamic response as well as the fatigue examination of a suspended inter-array power cable in floating offshore wind farms. This chapter provides general wind turbine theory, specific information about the included FOWT concepts, an overview of subsea power cables and background about the modeling in the numerical softwares OrcaFlex and UFLEX. It also contains theories about offshore environmental conditions, marine growth, and fatigue life determination.

2.1 Floating Offshore Wind Turbines

As mentioned in chapter 1.1, several different concepts for FOWTs exist. They all share the advantage of a possible installation in deeper waters (water depth larger than 60 m). Moreover, larger wind turbines enabling the capturing of more energy can be installed using FOWTs and areas with higher average wind speeds can be developed. However, the costs for FOWTs are currently significantly higher than the costs for bottom-fixed turbines and the more complex dynamics of floating systems need to be accounted for. Nevertheless, FOWTs are expected to experience significant growth in the future (GWEC Global Wind Energy Council, 2022a).

2.1.1 Mathematical Background of Wind Turbines

The basic concept of wind turbines is to convert the kinetic energy available in the wind into mechanical energy. This mechanical energy is then used by a generator to create electrical energy. According to Schaffarczyk (2014), Albert Betz and Hermann Glauert were the first to transfer theoretical models developed for ship and aeroplane propellers to wind turbines. This theory contains several restrictions but has been proven to be very useful for calculations due to its low implementation efforts. The following part on wind turbine theory is based on Schaffarczyk (2014).

Albert Betz Momentum Theory:

Kinetic energy *E* is determined by:

$$E = \frac{1}{2}mv^2 \tag{2-1}$$

where *m* is the mass and *v* is the velocity of an air flow for a wind energy converter. The mass flow $\dot{m}$ is given by:

$$\dot{m} = \rho_{air} A v \tag{2-2}$$

where ρ_{air} is the density of air and *A* is the cross-section area covered by the rotor. Therefore, the energy amount *P* passing through the area per unit time is:

$$P = \frac{1}{2}\dot{m}v^2 = \frac{1}{2}\rho_{air} v^3 A \tag{2-3}$$

The wind turbine removes energy from the air flow by reducing the wind velocity. The change in the velocities around the wind turbine is shown in Figure 2-1. The amount of the extracted energy P_T can be obtained by the following formula:

$$P_T = \frac{1}{2}\dot{m}(v_1^2 - v_3^2) = \frac{1}{2}\rho_{air}(A_1 v_1^3 - A_3 v_3^3) \tag{2-4}$$

where v_1 and A_1 are the flow velocity and the area before the energy extraction and v_3 and A_3 refer to the flow velocity and the area after the energy extraction.

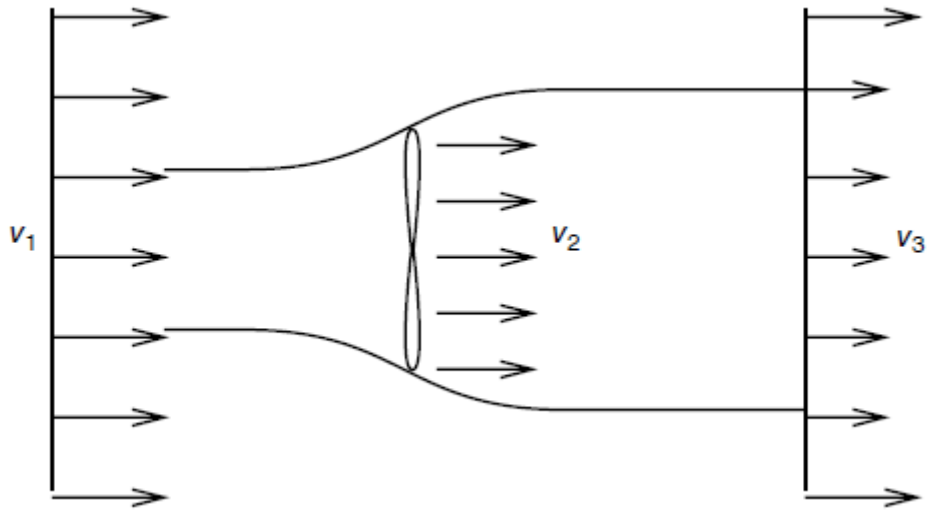

Figure 2-1: Flow relationships for a wind turbine (taken from Schaffarczyk (2014)).

The maximum amount of energy can be extracted from the wind for an optimal relationship of the flow velocities before and after the turbine, $\frac{v_1}{v_3}$. The power coefficient c_p was established as a reference for the power output:

$$c_p = \frac{P_T}{P_0} \tag{2-5}$$

where P_0 is the energy contained in a free-flowing stream without extraction. The maximum value of this coefficient is usually referred to as Betz limit:

$$c_{p,max} = \frac{16}{27} = 0.5926 \tag{2-6}$$

Airfoil Theory:

The blades are a key component of the wind turbine. The function of the foil-shaped blades is to transfer the kinetic energy available in the wind into the rotational movement of the rotor. As illustrated in Figure 2-2, the foil causes a separation of streamlines above and below it when placed in an airflow. The curved shape of the foil leads to a longer path for the streamlines above it than for the streamlines below it. Consequently, the flow velocity will increase above the foil to reach the trailing edge at the same time as the particles flowing below the foil. Bernoulli's principle states that an increasing velocity must be balanced by decreasing pressure. Therefore, a pressure difference between the top and bottom sides of the foil exists, leading to a lift force in upwards direction. The foil also experiences a drag force at the same moment.

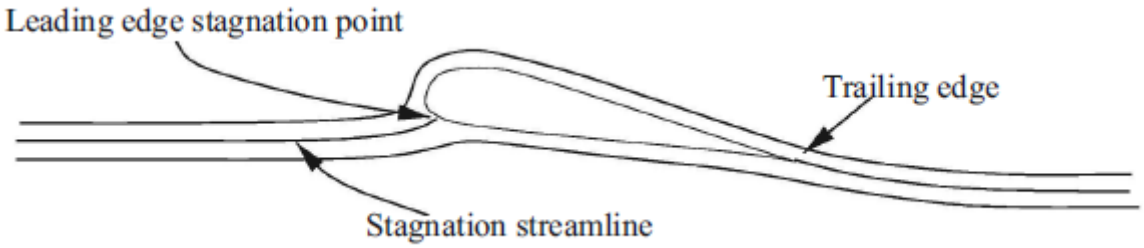

Figure 2-2: Flow around an airfoil (taken from Hansen (2015)).

Figure 2-3 shows a two-dimensional drawing of an exemplary airfoil. Here, α denotes the angle of attack of the resulting wind speed V_∞ and c denotes the cord length. L and D are the lift and drag forces, that combined result in the overall force F.

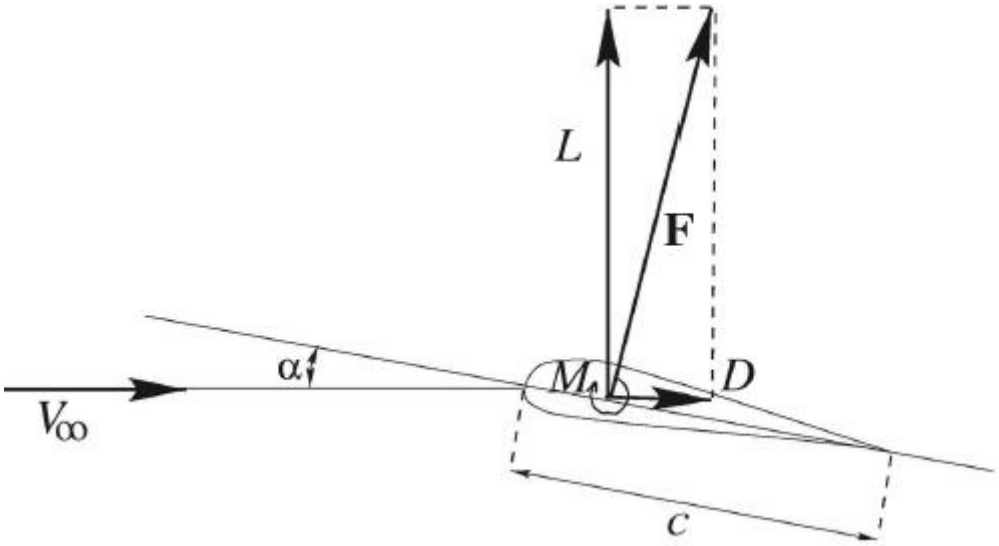

Figure 2-3: Cross-section of an airfoil (taken from Hansen (2015)).

The lift force *L* and the drag force *D* are defined as:

$$L = \frac{1}{2} C_l \rho_{air} V_\infty^2 c \qquad (2\text{-}7)$$

$$D = \frac{1}{2} C_d \rho_{air} V_\infty^2 c \qquad (2\text{-}8)$$

where C_l is the lift coefficient and C_d is the drag coefficient. These non-dimensional coefficients mainly depend on the geometry of the foil and the angle of attack of the flow. The drag force on the blade is always parallel to the resulting wind velocity, while the lift force acts tangential to the drag force. Therefore, when applying this theory to wind turbines, the ratio between the lift and drag forces, *L/D,* should be maximized since only the lift force will contribute to creating a rotational speed of the rotor.

Power Curve for Wind Turbines:

The power curve is divided into four different regions based on the incoming wind speed. For each region, a different control strategy is applied. In Region 1, the wind speed is very low, and the turbine does not produce energy. When the wind velocity increases above the cut-in wind speed, operating Region 2 is reached. In this region, the energy output increases together with the wind speed and generator torque control is used to optimize the production. When the wind speed exceeds the rated wind speed, blade pitch control is applied

to keep a constant energy output for the entire Region 3. If the wind speed is higher than the cut-out wind speed, this is referred to as Region 4. Here, the blades are pitched to feather, and the turbine operation is stopped to prevent damage resulting from the high wind loads. Figure 2-4 shows the different operating stages for the NREL 5 MW reference wind turbine. The vertical lines represent the cut-in, rated and cut-out wind velocities.

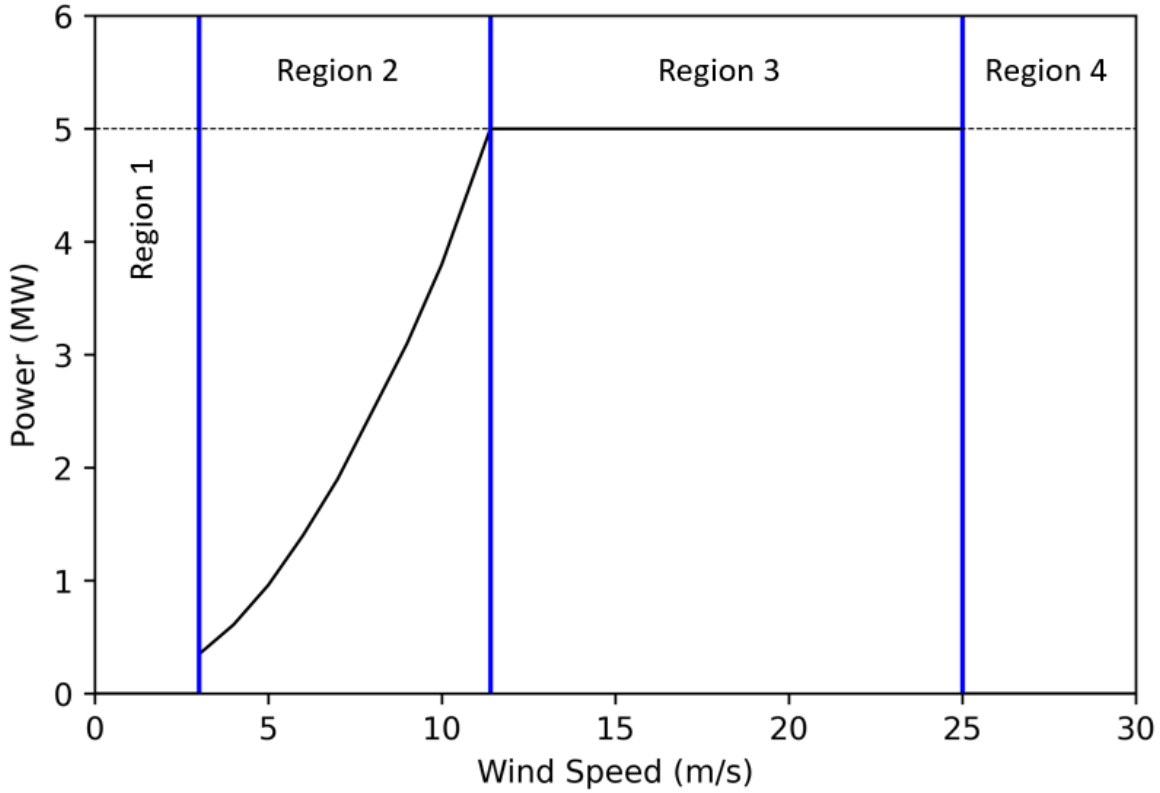

Figure 2-4: Power curve of the NREL 5 MW wind turbine (reproduced from Jonkman et al. (2009)).

2.1.2 OC3-Hywind 5 MW Concept

The OC3-Hywind 5 MW FOWT concept is based on a spar-buoy substructure. This type of floater has a large draft, and its center of gravity is located below the center of buoyancy, making it a very stable design. This type of floating platform has been used in the oil and gas industry for several decades and was developed as a FOWT concept by Equinor in their Hywind project (Nielsen, 2017). A full-scale model of this concept was implemented for the first time in 2009 and was installed as Hywind DEMO next to Karmøy in Norway (Equinor ASA, 2009). It

was the first FOWT with a rated energy output of more than 1 MW and was therefore extensively investigated in the following years. In 2017 and 2022, Equinor launched operations to the two wind parks Hywind Scotland (Eldøy, 2017) and Hywind Tampen (Equinor ASA, 2019), both consisting of several spar-type FOWTs. A spar structure based on the Hywind FOWTs suitable to support the NREL 5 MW reference wind turbine (Jonkman et al., 2009) was described by Jonkman (2010). As part of the Offshore Code Comparison Collaboration (OC3), this FOWT was studied very detailed (Jonkman & Musial, 2010; Ramachandran et al., 2013). Figure 2-5 shows a model of the wind turbine supported by a spar buoy. The wind turbine model is denoted as OC3-Hywind in this study.

Figure 2-5: OC3-Hywind 5 MW FOWT (reproduced from Jonkman (2010)).

2.1.3 CSC 5 MW Concept

The CSC 5 MW FOWT concept is based on a braceless steel semi-submersible substructure. The concept was proposed by Luan et al. (2016) and consists of a central column, three pontoons and three side columns. In 2015, a 1:30 model of the CSC FOWT was examined in a hybrid model test by Marintek (Luan et al., 2016). As for the OC3-Hywind FOWT, the NREL 5 MW reference wind turbine (Jonkman et al., 2009) is included in the design. Figure 2-6 shows a model of the CSC concept. This FOWT obtains its stability through ballast water in the pontoons, as usual for semi-submersible platforms. The small waterplane area of this type of floater makes it less affected by wave loads like for example ships. Several similar semi-

submersible FOWT concepts have been developed, and some designs are already implemented in projects, such as the WindFloat FOWTs in the Kincardine wind farm (Principle Power Inc., 2023).

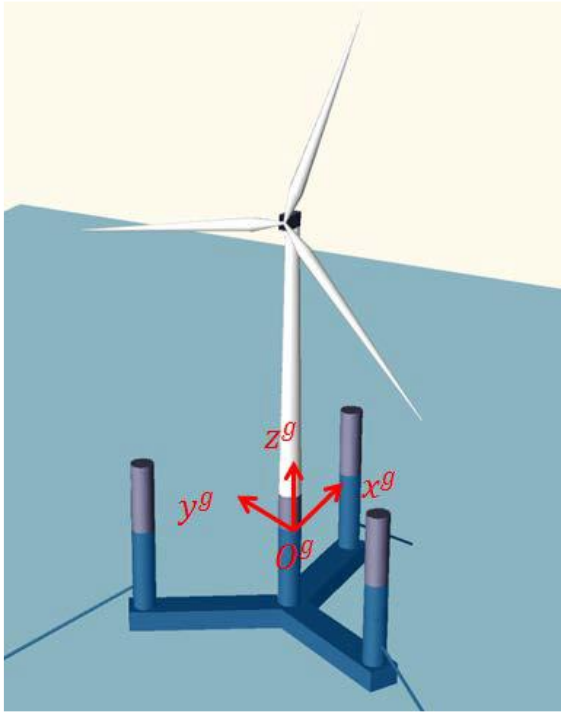

Figure 2-6: CSC 5 MW FOWT (reproduced from Luan et al. (2016)).

2.2 Offshore Power Cables

Offshore power cables are key components within offshore wind farm developments since they are used to transfer energy from the turbines to the onshore consumers. Typically, several turbines are connected by cables in a string, which ends at an offshore substation. These cables are called inter-array power cables. The cable connecting the offshore sub-station with the shore is called an export cable. It is usually designed to transport more power than the inter-array cables (Ikhennicheu et al., 2020). Figure 2-7 shows a typical cabling infrastructure for an offshore wind farm providing energy to consumers onshore. While bottom-fixed wind farms use static cables laid on the seabed, FOWT farms must use dynamic cables or a combination of both types to connect the individual turbines. In the design of dynamic cables, both electrical and mechanical performance requirements must be considered (Ikhennicheu et al., 2020).

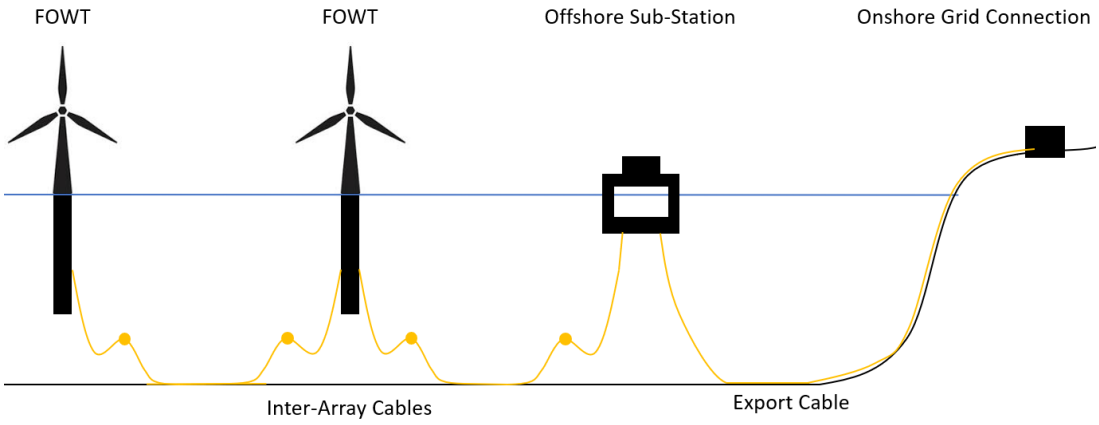

Figure 2-7: Inter-array and export cables in a FOWT farm.

2.2.1 Design of Dynamic Power Cables

To prevent damage during installation, where longer cable lengths are handled under high stresses, dynamic power cables must be of optimal bend stiffness and torsional balanced. Moreover, they must be able to tolerate increased fatigue during operation (Ikhennicheu et al., 2020). Figure 2-8 shows the typical components of a dynamic offshore power cable (Thies et al., 2012). The conductor core consists of copper or aluminum wires and transmits the electrical current. An electrical insulation layer often made of cross-linked polyethylene (XLPE) is surrounding the conductor core. The cable may contain an optical fiber to transfer data and fillers to support the structure. The inner sheath around the core acts as a water barrier and protection against fault currents. Mechanical strength and protection against impacts are provided through an armor layer made of steel. An outer sheath made of polypropylene ensures the abrasion resistance of the power cable.

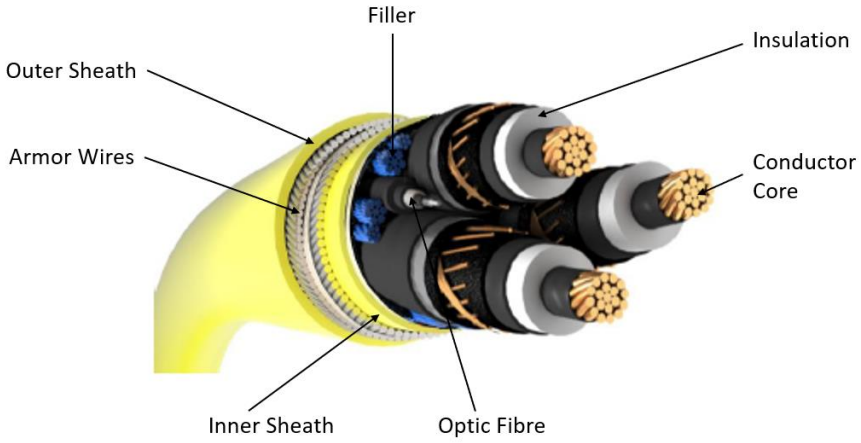

Figure 2-8: Dynamic power cable (adopted from Ikhennicheu et al. (2020)).

Marine power cables can have different types of ancillaries used for various purposes. Two of the most common ancillaries, bend stiffeners and buoyancy devices are included in this study. Bend stiffeners limit the curvature of a cable to a minimum by increasing the local stiffness. As a result, the bending stresses will be significantly reduced in the region where the bend stiffener is attached to the cable (Vaz et al., 2007). Buoyancy devices are connected to the cable to create an upward force. The size and the amount of buoyancy elements can be adjusted to meet specific design requirements (Thies et al., 2012).

2.2.2 Dynamic Power Cable Configurations

The offshore risers and umbilicals used in the oil and gas industry to transport fluids from the seabed wells to the platforms served as inspiration for the development of dynamic power cable configurations for FOWTs. Currently, the catenary and the lazy-wave shape shown in Figure 1-2 are the most common cable configurations (Ikhennicheu et al., 2020). According to Srinil (2016), the buoyancy modules used in lazy-wave setups must be carefully designed to result in the best shape with low tension and an optimized bending radius. By dissociating the motion of the floating structure from the cable contact with the seabed, the lazy-wave shape also aids in reducing the dynamic response of the cable. In this scenario, the buoyancy distribution is essential. Thies et al. (2019) investigated a lazy-wave power cable configuration connecting a FOWT to the seabed. They identified the motion response of the floater as the main contributor to the loads on the power cable. A configuration with a lowered buoyancy section was determined as the most suitable shape considering hang-off tensions and induced

bending stresses. A design optimization technique for inter-array cable configurations for FOWTs was described by Rentschler et al. (2019). They applied the technique on lazy-wave configurations in various water depths, leading to smaller buoyancy sections and a lower placement of the wave shape than in the original design. By utilizing a Fitness Factor in the static analysis, Rentschler et al. (2020) also optimized the lazy-wave shape for a power cable connecting a FOWT to the seabed. The normalized minimum breaking load plus the normalized minimum bend radius were combined to form the Fitness Factor. With this optimization technique, the maximum cable tension in the lazy-wave design in water depths up to 200 m was reduced by 50%.

A new configuration type, the suspended power cable connecting FOWTs directly as shown in Figure 1-2, was described by Rapha and Domínguez (2021). Schnepf et al. (2023) examined several suspended power cable designs between two FOWTs. They found that compared to cables with buoyancy modules, cables with buoys have much lower effective tensions. Shi et al. (2022) assessed the performance of short dynamic inter-array power cables with attached buoyancy modules connecting two FOWTs in extreme conditions. Buoyancy elements were identified to have the largest impact on the curvature and tension of the power cable. Schnepf et al. (2022) investigated a suspended power cable supplying power generated by a FOWT to a floating production storage and offloading unit (FPSO). Evenly distributed buoys attached to the power cable were identified as a measure to reduce the cable tensions in comparison to setups with freely hanging power cables or cables with buoys only attached to their middle section. Ahmad et al. (2023) developed a Fitness Factor based design procedure for suspended inter-array power cables connecting two FOWTs. Increasing the number of attached buoys was found to be a measure to reduce the maximum tensions in the power cable. Furthermore, the use of copper conductors was identified to be more suitable for suspended power cables than the use of aluminum conductors.

2.2.3 Fatigue of Dynamic Power Cables

Karlsen et al. (2009) investigated the general fatigue characteristics of a copper conductor inside a dynamic offshore power cable. Due to the restricted applicability of conventional stress-cycle (S-N) curves for copper conductors, they recommended employing strain-cycle

curves instead. The loads and fatigue life of a dynamic power cable utilized at floating offshore renewable energy projects were evaluated by Marta et al. (2015). In copper conductors, fretting has been found to be a significant crack-initiation process that leads to fatigue failure. Fatigue was the predominant failure mode in all their simulations. With the use of experimental data and FE simulations, Nasution et al. (2012) produced a S-N curve for a copper conductor in a dynamic power cable used in offshore wind farms. Nasution et al. (2014) also investigated the impacts of tension and bending loads on copper conductors. They found that inter-layer friction occurring due to curvature is the main reason for copper conductor fatigue failures in dynamic power cables.

Thies et al. (2012) investigated the effective tension as well as the fatigue life of a dynamic power cable in lazy-wave and catenary shapes connecting a wave energy converter to the seabed. A lower maximum tension and a lower number of fatigue cycles were determined for the lazy-wave configuration compared to the catenary configuration. A significant extension of the fatigue life of the dynamic power cable was achieved by reducing the maximum effective tension. Using the computational programs SIMA and Bflex, Bakken (2019) determined the fatigue life of a dynamic power cable connecting a FOWT to the seabed. The copper conductor's fatigue life was lowest where the largest tension range occurred. Local friction effects were determined as the principal causes leading to fatigue damage. Hu et al. (2022) performed experimental and numerical investigations of the bending behavior of a copper wire inside a dynamic power cable. They identified the nonlinear bending of the dynamic power cable as the main parameter causing fatigue failures. Svensson (2020) created prediction models for the fatigue of dynamic power cables using experiments and finite element simulations. In the assessment of the power cable's fatigue life, interlayer friction forces were determined as an important influence. Zhao et al. (2021) investigated the behavior and fatigue of power cables attached to a FOWT in shallow water in the lazy-wave and double-wave configurations. Regarding the tension and fatigue of the power cable for both designs, they found that the hang-off point was the most crucial location. The fatigue life of the double-wave configuration was determined by the second buoyancy section. The fatigue life of a power cable attached to a wave energy converter in the lazy-wave shape was estimated by Ballard et al. (2020). Fatigue damage resulting from cycles in the cable curvature was found to be the critical parameter in their study. Beier et al. (2023b) determined the fatigue life for a suspended dynamic power cable connecting two FOWTs using the numerical

software OrcaFlex and UFLEX. They obtained a very long fatigue life for their cable, with the copper conductor being the critical component. As the main factor leading to fatigue damage, stress components resulting from curvature variations were identified. They stated that along the cable the largest fatigue damage occurs near the hang-off locations.

2.3 Computational Software

In this section, the computational software utilized for this master thesis are explained.

2.3.1 OrcaFlex

The numerical software OrcaFlex is able to perform global static and dynamic analysis of different types of offshore systems as well as finite element modeling of line structures (Orcina Ltd, 2022). Objects can be modeled by different representations, including vessels, lines, 6D and 3D buoys, shapes, and turbines. The individual objects can be connected, or can be defined as fixed, anchored, or free. External functions, for example Python codes, can be loaded to model the generator torque and blade pitch control of a wind turbine. In this section, the working principles and theories of OrcaFlex that are used for the model in this study are described.

Lines

Line objects can be represented in OrcaFlex as “finite element” or “analytic catenary”. Figure 2-9 shows the finite element representation of a line. The line is discretized into several segments, which are modeled as straight massless lines with a node at each end. Only the axial and torsional properties of the line are modeled by the segments. Additional characteristics, such as mass, weight, and buoyancy, are all grouped at the nodes. To determine the tension of a segment, OrcaFlex uses its initial length, the rate of change of its length as well as the segments axial direction.

The analytic catenary representation is used to simplify the quasi-dynamic mooring analysis. In this method, the mooring line loads are determined based on analytic catenary equations. These equations consider the entire line, so a discretization into segments is not necessary. This representation calculates the static configuration of the line for a given set of input

parameters. However, it does not consider dynamic effects and thus can only be used for cases, where the inertia, as well as bend stiffness of the mooring lines, can be neglected, and the damping can be accounted for by an additional vessel.

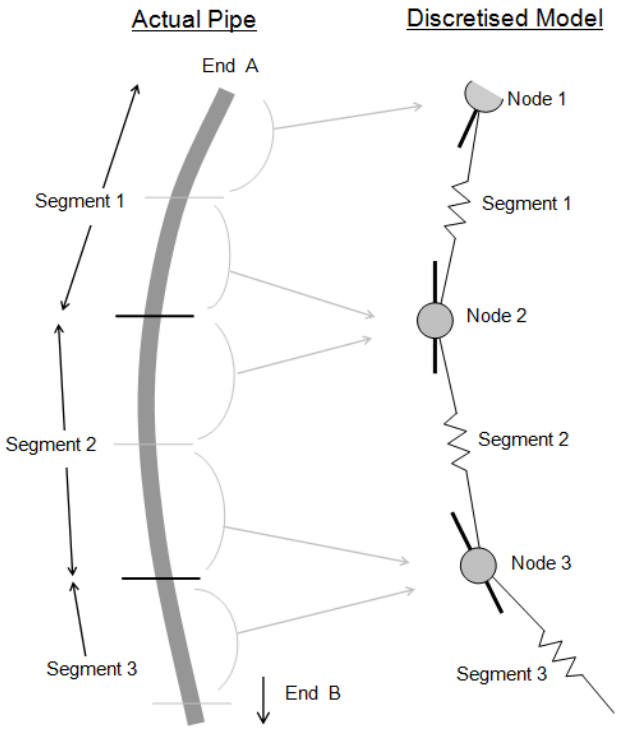

Figure 2-9: OrcaFlex finite element line representation (Orcina Ltd, 2022).

Buoys

6D buoys are rigid bodies with 6 degrees of freedom (DOFs) and a specified weight force applied at the center of gravity. Lumped mass buoys are the simplest buoy type in OrcaFlex. They don't have any shape but can be assigned several properties such as volume, damping or drag coefficients. Spar buoys are used for modelling axisymmetric buoys with a vertical axis and significant surface-piercing effects. They are represented by a series of co-axial cylinders placed along the local vertical axis. Surface-piercing effects, for example righting moments in pitch and roll, are determined based on the intersection of the water surface with the individual cylinders, considering the instantaneous position and orientation of each cylinder segment in the wave. For each cylinder, the slam forces are calculated and applied separately. The buoyancy force on an individual cylinder of the spar buoy is calculated by:

$$Buoyancy\ Force = \rho * g * WettedVolume \quad (2\text{-}9)$$

where ρ is the water density, g is the gravitational acceleration and *WettedVolume* is the submerged volume of the cylinder. The buoyancy force is applied upwards at the centroid of the submerged volume.

The hydrodynamic loads for lines and spar buoys are determined in OrcaFlex by an extended form of Morison's equation:

$$F = \left(C_m \Delta a_f - C_a \Delta a_b\right) + \frac{1}{2}\rho C_d A |v_r| v_r \quad (2\text{-}10)$$

where F is the fluid force per unit length on the body, C_m is the inertia coefficient for the body, Δ is the mass of the displaced fluid, a_f is the fluid acceleration relative to the earth, C_a is the added mass coefficient for the body, a_b is the body acceleration relative to the earth, C_d is the drag coefficient for the cylindrical object, A is its drag area and v_r represents the fluid velocity relative to the body.

Vessels

OrcaFlex's vessel type serves as one of the model's boundary conditions. Very basic data sources, such as time histories, prescribed or harmonic motion, or even external calculations, can be used to determine a vessel's motion. OrcaFlex vessels are primarily designed to simulate rigid entities, such as semi-submersibles, floating platforms, barges, and ships, that are large enough for wave diffraction to be noticeable. The vessel object needs a lot of information to define its properties in order to simulate a floating body. The output of hydrodynamic diffraction analyses performed with OrcaWave or other similar softwares can be imported to OrcaFlex. When doing this, added mass, damping and response amplitude operators (RAOs) will be used by OrcaFlex to model the vessel behavior. On the vessel data type form, case-specific information is provided, including the vessel's position and the method for calculating motion.

Turbines

Horizontal-axis wind turbines are modelled using turbine objects. The generator, gearbox, hub, and blades have their own specific models assembling to the OrcaFlex turbine object. Blades can either be represented as rigid objects or allowed to be flexible to include the influence of aeroelastic coupling. The structural model for blades is comparable to that for lines. An adaptation of the AeroDyn (Jonkman et al., 2017) blade element momentum (BEM) method is used in OrcaFlex to calculate aerodynamic loading. The induction factors for each blade segment are recalculated at each time step as a result of the instantaneous relative flow conditions in a quasi-steady BEM model or equilibrium wake.

Static Analysis

Static analysis determines the positions and orientations for all elements in an OrcaFlex model such that all forces and moments are in equilibrium. The analysis is performed in two steps, both using an iterative process. First, only the equilibrium positions of lines are calculated. Afterwards, the DOFs of all objects are released and the whole system's static equilibriums are determined. The static analysis includes the self-weight of the structural model, buoyancy forces as well as hydrodynamic drag forces due to constant wind and current. The results of the static analysis are used as the starting configuration for the dynamic analysis.

Modal Analysis

The undamped natural modes of a system can be determined by modal analysis and are denoted by their modal frequency and mode shape. The analysis can be performed either for the whole system or only for individual lines. The added mass of vessel objects is considered for only one frequency which must be specified to receive realistic natural periods. The modal analysis in OrcaFlex is based on a discretized form of standard modal theory.

Dynamic Analysis

The time domain dynamic analysis simulates the movements of the model over a predetermined period starting from the initial position determined by the static analysis. A dynamic analysis is conducted to obtain the motion response of the system due to the interaction of wave, wind, and current loads as well as other design characteristics. The period of simulation is represented by a series of subsequent stages in the dynamic analysis, as shown

in Figure 2-10. Before the main simulation stage, there is a build-up phase where the vessel and wave motions ramp up to their full amplitude from zero. This phase gives the simulation a smooth start and shortens the time needed for the transition from static to fully dynamic motion. To solve the equation of motion, OrcaFlex implements an explicit and an implicit dynamic integration scheme. Both approaches recompute the system geometry at each time step. As a result, the simulation fully accounts for all geometric non-linearities, including the spatial variation of wave and contact loads.

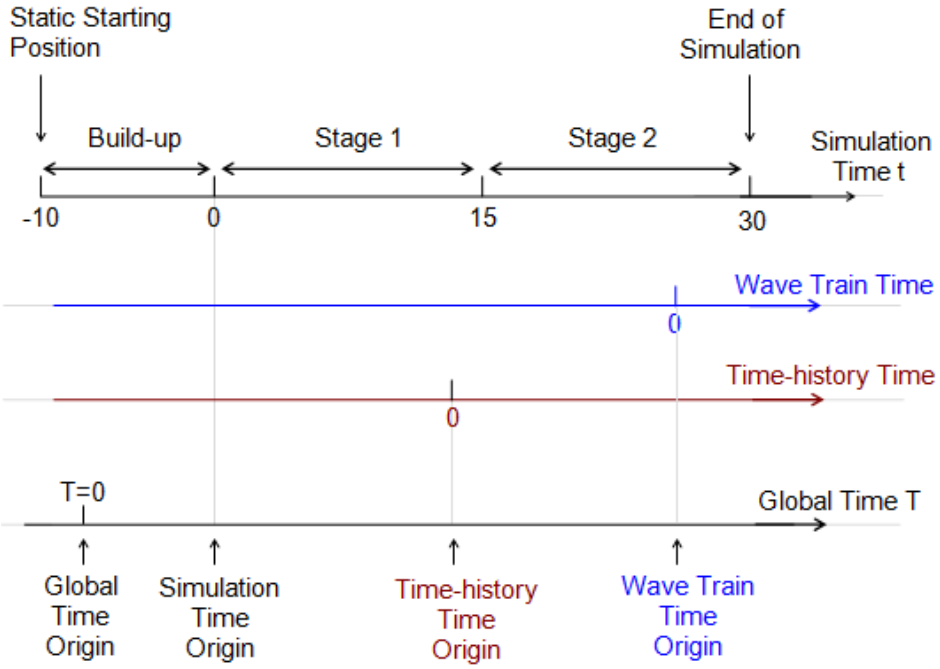

Figure 2-10: Time and simulation stages in the dynamic analysis (taken from Orcina Ltd (2022)).

Fatigue Analysis

The fatigue analysis in OrcaFlex is a post-processor tool which determines the fatigue damage based on dynamic simulation results using different methods. Based on S-N curves, the fatigue is calculated for metal risers using homogenous pipe stress and for cables using stress factors. Mooring line fatigue damage is determined from effective tension ranges using tension-cycle curves. The obtained damage is accumulated by either deterministic regular wave fatigue analysis, deterministic irregular wave fatigue analysis based on Rainflow cycle counting methods, or stochastic irregular wave fatigue analysis using spectral methods. To account for

different environmental conditions, several load cases can be included in the fatigue analysis. Typically, this is done using wave scatter tables.

2.3.2 UFLEX

The finite element modelling (FEM) software UFLEX developed by SINTEF Ocean is a numerical tool used to estimate the stresses of different components in complex umbilical or power cable cross-sections (SINTEF, 2018). UFLEX has been validated by comparing the results of stress analyses with the results of full-scale laboratory tests (Sævik & Bruaseth, 2005). Actual conditions can be modelled by applying a combination of different loads. The load types included in UFLEX are tension, torsion moment, bending moment, internal and external pressure as well as contact loads. Regarding the tension, torsion, and pressure loads, it is assumed that the problem is two-dimensional and axisymmetric. It is also assumed that the bent pipe can be represented by a torus for which differential geometry can be used to get closed-form solutions for the bending and torsion of helix elements. UFLEX considers contacts between different layers as well as contacts between components inside the same layer, such as armor wires inside one helical layer. The cable cross-section consists of two different body types, filled bodies and tubulars. Filled bodies are usually represented by the element type beam, while the shell type is used for tubulars. The beamshell element type can be used for both body types. All nodes in a model are assumed to move in the same two-dimensional plane and all bodies are connected to a super node. The general node structure in UFLEX is shown in Figure 2-11. The degrees of freedom (DOFs) of the super nodes in the longitudinal and transverse directions are connected to the longitudinal movement and the torsional rotation of the center node of the model. Therefore, only the DOF in the radial direction remains free to move. Figure 2-12 shows the coordinate systems of the beam and shell elements. The super node of the components is always located at the respective cylinder or tube center. During the simulation of a case in UFLEX, an iterative numerical procedure is used to solve the finite element equations.

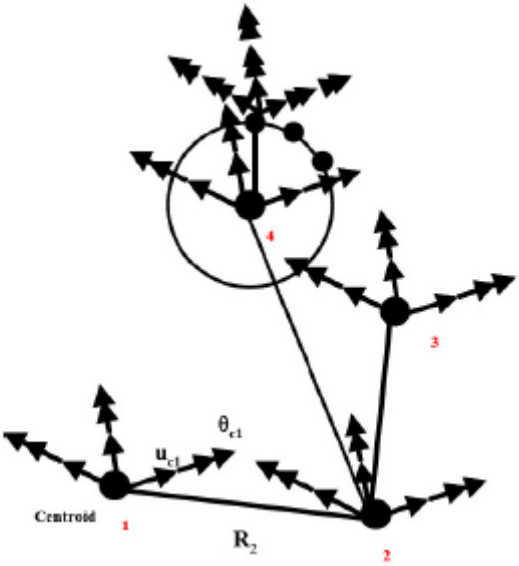

Figure 2-11: UFLEX node structure (taken from SINTEF (2018)).

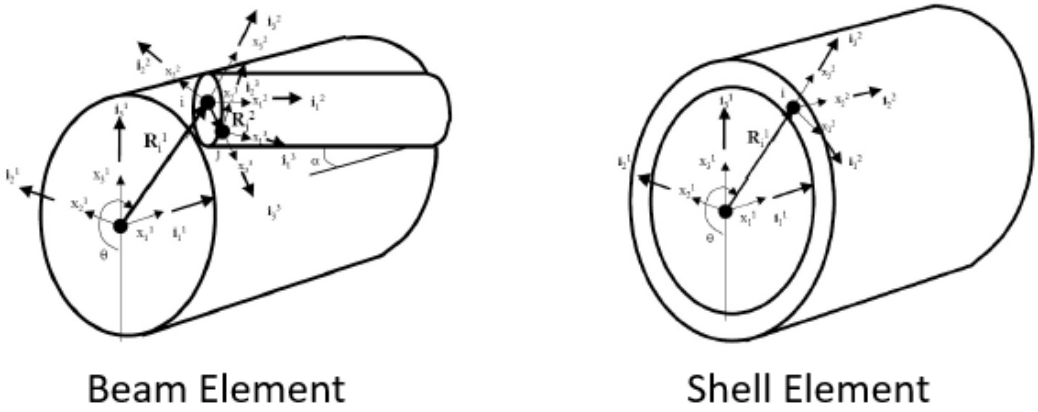

Figure 2-12: Coordinate systems for the two main element types (adapted from SINTEF (2018)).

2.4 Environmental Conditions and Marine Growth

FOWT motions are influenced by the environmental loads waves, wind and current. The suspended power cable is in addition to these loads also affected by marine growth. This section gives an overview of the environmental aspects affecting the wind turbine system in this study.

2.4.1 Waves

Ocean waves have significant impacts on floating structures as well as on submerged objects close to the sea surface. This section presents the statistical description of irregular waves, the loads waves impose on objects as well as the motion responses of structures due to waves.

Wave Energy Spectra

Irregular waves can be represented by adding together several different regular waves. The modelling of irregular waves makes use of sea-surface elevation spectra. These spectra show the energy content of a sea state based on the wave frequencies. For a long-crested irregular sea, the wave elevation can be expressed by (Journée & Massie, 2001):

$$\zeta(t) = \sum_{n=1}^{N} \zeta_{a_n} \cos(k_n x - \omega_n t + \varepsilon_n) \qquad (2\text{-}11)$$

where for each component, n, ζ_{a_n} is the wave amplitude, k_n is the wave number, ω_n is the circular frequency and ε_n is a random phase angle.

A wave energy spectrum is defined by the following formula:

$$S_\zeta(\omega_n)\, d\omega = \frac{1}{2}\zeta_{a_n}^2 \qquad (2\text{-}12)$$

Several wave energy spectra have been described by different researchers. This study uses the JONSWAP spectrum developed by Hasselmann et al. (1973) in the Joint North Sea Wave Project in 1969. The spectrum is based on two statistical properties of an irregular sea state, the significant wave height H_s and the peak period T_p. The significant wave height H_s is obtained by taking the average of the one-third highest waves in a sea condition. The JONSWAP spectrum is described by the following formula:

$$S_\zeta(\omega_n) = \frac{320\, H_s^2}{T_p^4}\omega^{-5}\exp\left\{-\frac{1950}{T_p^4}\omega^{-4}\right\}\gamma^A \qquad (2\text{-}13)$$

where γ = 3.3 is the peakedness factor and A is given as:

$$A = \exp\left\{-\left(\frac{\frac{\omega}{\omega_p}-1}{\sigma\sqrt{2}}\right)^2\right\} \qquad (2\text{-}14)$$

where ω_p is the circular frequency at the spectral peak and σ is a step function of ω. The step function σ is equal to 0.07 for ω smaller than ω_p and to 0.09 for ω larger than ω_p. Figure 2-13 shows the JONSWAP spectrum for a significant wave height H_s = 4 m and a peak period T_p = 10 s.

Wave Loads

The wave loads on the spar type FOWT can be estimated using Morison's equation. This equation is suitable for slender cylinders and consists of two terms, one for the drag force and one for the inertia force. The resultant force per unit length is given by (Journée & Massie, 2001):

$$F(t) = F_{inertia}(t) + F_{drag}(t) = \frac{\pi}{4}\rho\, C_m\, D^2\, \dot{u}(t) + \frac{1}{2}\,\rho\, C_d\, D\, u(t)\,|u(t)| \qquad (2\text{-}15)$$

where D is the diameter of the cylinder, $\dot{u}(t)$ is the flow acceleration at a given time and $u(t)$ is the flow velocity at a given time.

For the semi-submersible FOWT, a diffraction analysis needs to be performed to obtain the loads due to waves.

Response

The response spectrum of a motion $S_T(\omega)$ can be determined through the transfer function and the wave spectrum by:

$$S_T(\omega)\, d\omega = |H(\omega)|^2\, S_\zeta(\omega) \qquad (2\text{-}16)$$

where $H(\omega)$ is the transfer function dependent on the frequency ω.

In Figure 2-13 the transfer function for heave motion and a response spectrum resulting from a JONSWAP wave spectrum are shown for an exemplary case. The shape of the transfer function has a significant impact on the motion response.

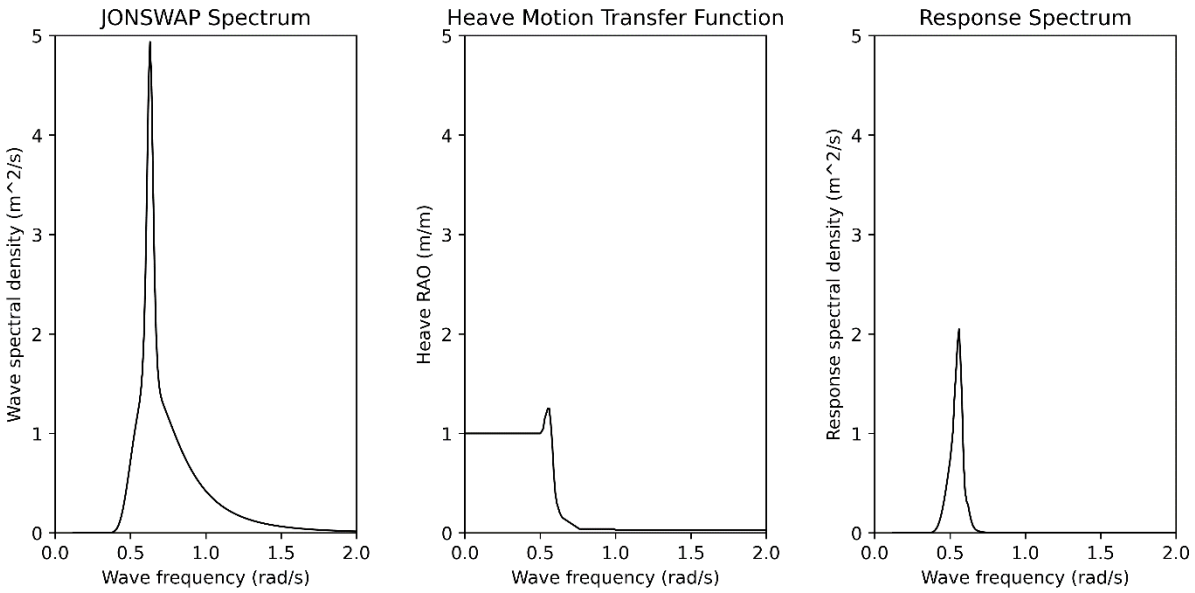

Figure 2-13: Wave spectrum, transfer function and motion response.

2.4.2 Wind

The wind speed profile can be described by several different models. Usually, the wind speed varies with the height. The gradient of the wind speed profile is influenced by both the topography and atmospheric stability. The Norwegian Petroleum Directorate (NPD) spectrum is selected as the wind speed profile (Norwegian Petroleum Directorate (NPD), 1995) because the North Sea is chosen as the reference location for this study.

The NPD spectrum is described by:

$$S(f,z) = 3.2\, U_{ref}^2 \left(\frac{z}{10}\right)^{0.45} \left[1 + \tilde{f}^n\right]^{-\frac{5}{3n}} \qquad (2\text{-}17)$$

where *n* is 0.468, U_{ref} is the 1-hour mean wind speed at 10 m above the sea surface and *z* is the height above the sea surface. $\tilde{f}$ can be obtained by:

$$\tilde{f} = 172\, f \left(\frac{z}{10}\right)^{\frac{2}{3}} \left(\frac{U_{ref}}{10}\right)^{-\frac{3}{4}} \qquad (2\text{-}18)$$

The 1-hour mean wind speed on a specific height for the NPD spectrum is:

$$U_z(z) = U_{ref} \left[1 + 0.0573 \sqrt{1 + 0.015\, U_{ref}} \ln\left(\frac{z}{10}\right)\right] \qquad (2\text{-}19)$$

2.4.3 Current

Slender structures like marine risers, mooring lines, and subsea cables can experience large current loads. Currents consist of several types, such as tidal currents (astronomical tides), circulation currents (oceanic-scale circulation patterns), storm-generated currents, currents over steep slopes, and local eddy currents (Standards Norway, 2007). However, extreme events for each of the existing components do typically not happen at the same time. For the majority of applications, the current velocity can be viewed as a continuous flow field in which the magnitude and direction of the velocity vector depend only on the depth.
The total current is a sum of several components based on DNV (2010):

$$v_c(z) = v_{c,wind}(z) + v_{c,tide}(z) + v_{c,circ}(z) + \dots \quad \textit{(2-20)}$$

where $v_c(z)$ is the total current velocity at a specific depth, $v_{c,wind}(z)$ is the wind-induced, $v_{c,tide}(z)$ the tidal and $v_{c,circ}(z)$ the circulational current velocity at the same depth.

Following the earths' harmonic astronomical motions, tidal currents are predictable. The maximum tidal current precedes or follows the highest and lowest astronomical tides. Tides in the deep ocean are typically weak currents, although coastal patterns make them stronger. Strong tidal currents can be found in coastal inlets and straights. When detailed field measurements are not available, DNV (2010) recommends applying a power law profile for the velocity variation of the tidal current with the water depth, assuming a unidirectional current:

$$v_{c,tide}(z) = v_{c,tide}(0)\left(\frac{d+z}{d}\right)^{\alpha} \quad \textit{(2-21)}$$

where $v_{c,tide}(0)$ is the tidal current at the still water level, *d* is the water depth and *α* is an exponent typically taken as $\alpha = \frac{1}{7}$.

The wind-generated currents only occur next to the sea surface and vanish below a specific water depth d_o. According to DNV (2010), a linear profile can be assumed for the wind-induced current above the depth d_o:

$$v_{c,wind}(z) = v_{c,wind}(0)\left(\frac{d_0 + z}{d_0}\right) \quad (2\text{-}22)$$

where $v_{c,wind}(0)$ is the wind-generated current at the still water level and the reference depth for the wind-generated current is typically taken as d_o = 50 m.

If statistical data is unavailable for a deep water area along an open coastline, the wind generated current at the still water level can be estimated by:

$$v_{c,wind}(0) = k\, U_{1\ hour,10\ m} \quad (2\text{-}23)$$

where k is the roughness height, taken as $0.015 < k < 0.03$, and $U_{1\ hour,10\ m}$ is the 1 hour mean wind speed at 10 m above the sea surface.

2.4.4 Marine Growth

The weight and surface roughness of a subsea structure will both increase due to marine growth. Sarpkayas (2010) research has shown that the increasing surface roughness increases the hydrodynamic load significantly and triggers the laminar to turbulent transition at lower Reynolds numbers. Spraul et al. (2017) investigated the impact of marine growth on the dynamic behavior of a version of the lazy wave design where the landing point is vertical to the bottom, a so-called steep wave. They concluded that the most important configuration parameters were the combined net buoyancies of the cable and the buoyancy modules, which mainly depend on the thickness and density of marine growth.

Increase of the Cable Diameter

The effective hydrodynamic diameter of a cylindrical object changes due to marine growth. Based on DNV (2010), the increased effective hydrodynamic diameter is given by:

$$D_{mg} = D + 2\,t \quad (2\text{-}24)$$

where D_{mg} is the effective diameter of the power cable including the marine growth and t is the thickness of the marine growth layer.

The thickness and density of the marine growth layer depend on the depth where the object is located as well as on the geographical region. Table 2-1 lists the values for the Norwegian continental shelf (59° to 72° N) based on the information provided by NORSOK (Standards Norway, 2007).

Table 2-1: Thickness and density of the marine growth layer between 59° and 72° N.

Depth (m)	Thickness *t* (mm)	Density ρ_{mg} (kg/m^3)
Above +2	0	-
-15 to +2	60	1325
-30 to -15	50	1325
-40 to -30	40	1325
-60 to -40	30	1100
-100 to -60	20	1100
Below -100	10	1100

Increase of the Cable Weight

The marine growth on the power cable also affects the weight of the power cable. The additional weight can be accounted for by using the following formula:

$$W_{mg} = \left(\rho_{mg} - \rho\right) g \qquad (2\text{-}25)$$

where W_{mg} is the weight of the marine growth layer, ρ_{mg} is the marine growth density and ρ is the water density.

Change of the Cable Drag Coefficient

The drag coefficient of the power cable is determined based on the Reynolds-number and the surface roughness. The Reynolds-number is influenced by the increasing diameter due to marine growth. Based on DNV (2010), the surface roughness for marine growth affected objects can be taken between $5*10^{-3}$ m and $5*10^{-2}$ m, while NORSOK (Standards Norway, 2007) suggests a value of $2*10^{-2}$ m. In this study, the surface roughness is assumed to be constant since small marine growth effects will occur rapidly on the cable and the inclusion of it will lead to conservative results for all considered setups (ESDU, 2007).

2.5 Fatigue Life Assessment

Damage occurring due to cyclic loading over a long time, where the stress is often lower than the yield stress for a particular material, is called fatigue. The following section introduces some basic concepts related to fatigue as well as the methods used in this master thesis.

2.5.1 Basic Fatigue Concepts

Figure 2-14 shows a cyclic loading time history with a constant amplitude.

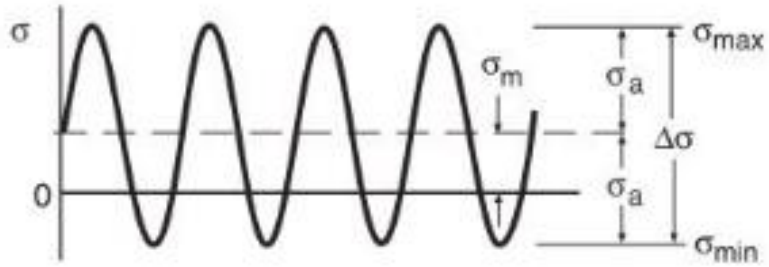

Figure 2-14: Example of a fatigue load history (taken from Dowling (2012)).

Based on Figure 2-14, the following terms can be defined:

- σ_{max} is the maximum stress in a cycle.
- σ_m is the mean stress in a cycle.
- σ_{min} is the minimum stress in a cycle.
- $\Delta\sigma$ is the stress range ($\Delta\sigma = \sigma_{max} - \sigma_{min}$).
- σ_a is the stress amplitude ($\sigma_a = \Delta\sigma/2$).

The stress ratio, R is given by:

$$R = \frac{\sigma_{min}}{\sigma_{max}} \qquad (2\text{-}26)$$

To estimate the fatigue life of a material, S-N curves are established based on experimental tests. In these curves, the stress amplitude, σ_a, is plotted versus the number of cycles, N. For some materials, no fatigue damage occurs below a specific stress amplitude, denoted as σ_e. Figure 2-15 shows an exemplary S-N curve for a material with an endurance limit at the stress amplitude σ_e.

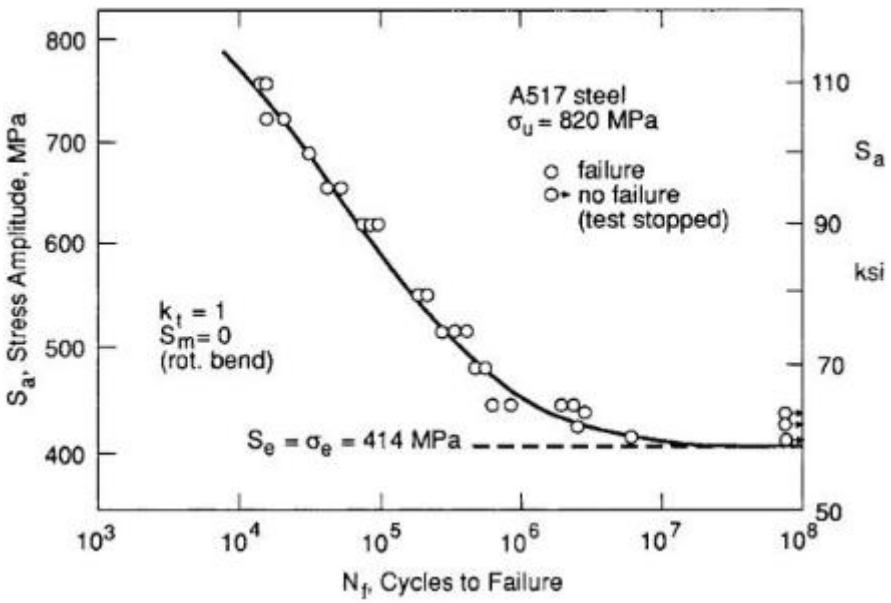

Figure 2-15: Exemplary S-N curve (taken from Dowling (2012)).

One cycle causes damage that is almost always negligible and not detectable by instruments. Fatigue failures occur due to the cumulative damage induced by cyclic loading. Cyclic loads resulting from waves, currents, motions, and vortex-induced vibrations can seriously damage marine structures. There are three stages of fatigue damage:

- Crack initiation, N_i
- Crack growth, N_g
- Fatigue failure

The number of cycles until a fatigue failure occurs can be determined by:

$$N = N_i + N_g \tag{2-27}$$

2.5.2 Irregular Loading

Irregular loading is common for marine structures, where the amplitude and the frequency of the loads vary over time. Figure 2-16 shows an exemplary irregular load history. The basic concepts of irregular loading are defined as follows (ASTM, 2011):

- Reversal: the location where the first derivative of the load-time history changes sign.
- Peak: every reversal where the sign changes from positive to negative.
- Valley: every reversal where the sign changes from negative to positive.
- Range: the difference between successive peaks and valleys.

- Mean crossing: the number of times the load-time history crosses the mean-load level with a positive first derivative.

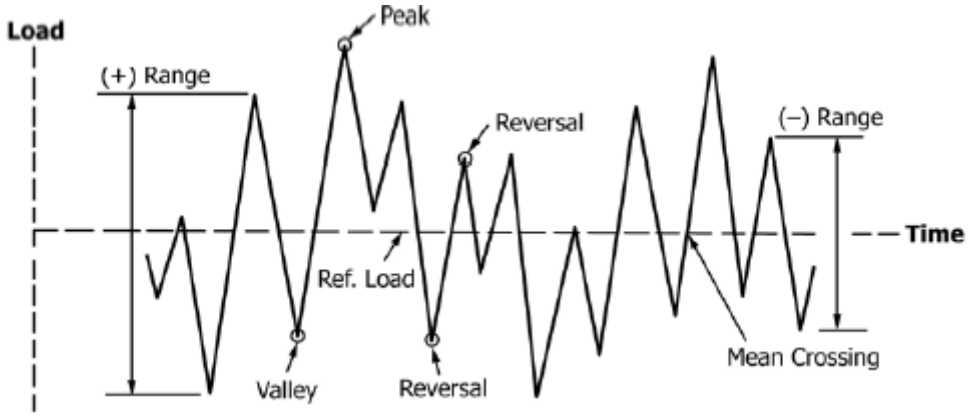

Figure 2-16: Example of an irregular load history (taken from ASTM (2011)).

2.5.3 Rainflow Counting

Several different methods exist to count the cycles in irregular load histories including Rainflow Counting. The name of this method origins from the case of rain falling on the roof of a pagoda building. In the Rainflow Counting method, the cycles are counted in a way representing the response of the material. The fatigue damage resulting from a closed cycle in the irregular loading is assumed to be equal to a cycle in a constant amplitude loading. Half cycles are neglected in this procedure, with only very few of them existing in every realistic case (Bakken, 2019). The Rainflow Counting algorithm implements the following procedure described by ASTM (2011): The counting starts at the first valley. In case the next valley is deeper or equal to the first one, a cycle count is done. In case this valley is not deeper than the previous one, it needs to be checked if the next peak is higher than the previous one. If this is true, a cycle is counted. If not, the procedure continues by considering the next valleys and peaks until a closed loop is detected. After a cycle has been counted, the procedure is repeated starting from the consecutive valley. After all cycles have been identified, the results from the Rainflow Counting can be noted based on their stress range in a histogram. Figure 2-17 shows an irregular loading and the results of a Rainflow Counting performed on this time history.

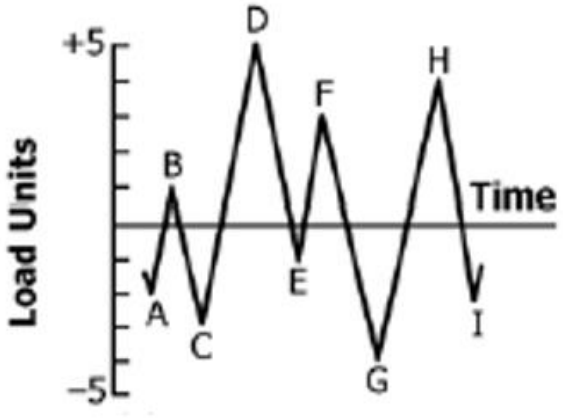

Range (units)	Cycle Counts	Events
10	0	
9	0.5	D-G
8	1.0	C-D , G-H
7	0	
6	0.5	H-I
5	0	
4	1.5	B-C , E-F
3	0.5	A-B
2	0	
1	0	

Figure 2-17: Rainflow Counting example case (adopted from ASTM (2011)).

2.5.4 Miner-Palmgren Rule

To determine the accumulated damage due to irregular cyclic loading several methods can be used. The Miner-Palmgren Rule is a simple approach that is commonly used for fatigue assessments. It assumes constant damage for a given stress range. The Miner-Palmgren Rule can be expressed through the following formula (Kauzlarich, 1989):

$$D = \sum_{j=1}^{k} \frac{n_j}{N_j} \qquad (2\text{-}28)$$

where *D* is the cumulative damage, *j* is a specific stress range, *k* is the total number of stress ranges, *n* is the number of cycles counted in a specific stress range, and *N* is the number of cycles until damage occurs in a specific stress range. The values for the number of cycles *N* can be obtained from S-N curves.

Chapter 3 - Methodology and Numerical Setup

This chapter presents the methodology of the present study and the numerical setups of the models. First, the modelling of the FOWTs is described. Second, the properties and the setup of the suspended inter-array power cable are explained. Third, the applied environmental conditions and the marine growth effects on the power cable are presented. The last part explains the procedure of the case study. The dynamic analysis software OrcaFlex version 11.2d (Orcina Ltd, 2022) is used for the modelling of the global setup, and the numerical software UFLEX 2D version 2.8 (SINTEF, 2018) is used to determine some properties based on the power cable cross-section.

3.1 Floating Wind Turbines Setup

In this section, the numerical modelling of the two types of FOWTs in OrcaFlex is described. For both setups, the same water depth of 200 m is selected to enable a better comparison of the results.

3.1.1 OC3-Hywind FOWT Setup

The OC3-Hywind 5 MW spar type FOWT modelled in this study is based on Jonkman et al. (2009) and Jonkman (2010). Figure 3-1 shows the OrcaFlex model of the OC3-Hywind 5 MW FOWT. The submerged column of the substructure is constructed as a spar buoy in OrcaFlex. Detailed information about the geometry, the properties and the mooring system of the OC3-Hywind 5 MW FOWT is presented in Chapter 4 and Chapter 5.

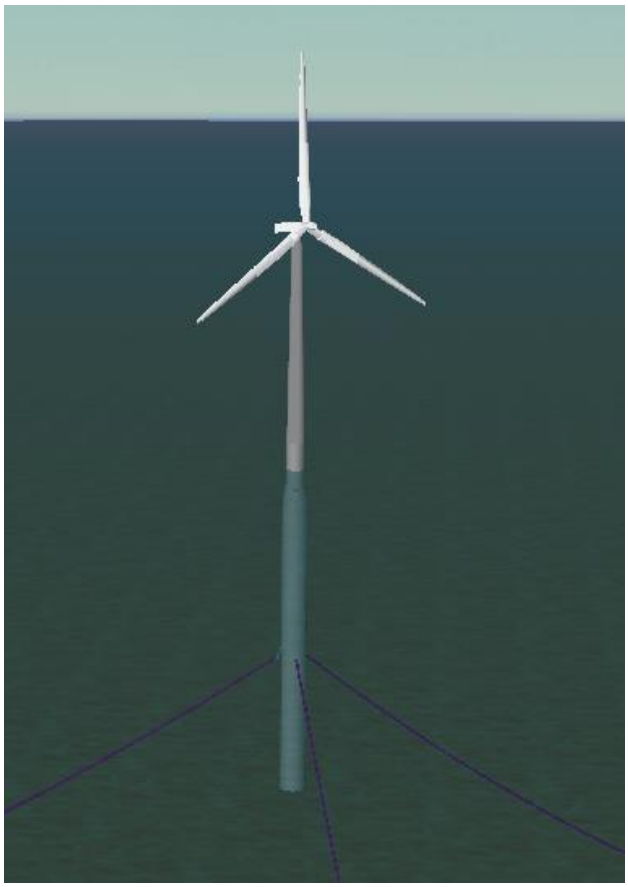

Figure 3-1: OC3-Hywind FOWT OrcaFlex model.

3.1.2 CSC FOWT Setup

The semi-submersible FOWT employed in this study is the braceless steel 5 MW CSC FOWT. The design basis for this 5 MW CSC FOWT is provided by Luan et al. (2016). A central column, three side columns, and three pontoons make up its hull. The hydrodynamic properties of the CSC FOWT are determined with the hydrodynamic analysis software Wadam neglecting the mooring lines, which are modeled in present simulations within the OrcaFlex software. These properties are imported into OrcaFlex, and a vessel object is used to represent the FOWT. The OrcaFlex model of the CSC FOWT is shown in Figure 3-2. The CSC FOWT uses the identical 5 MW NREL turbine as the OC3-Hywind FOWT. Detailed information about the geometry, the properties and the mooring system of the 5 MW CSC FOWT is presented in Chapter 4 and Chapter 5.

Figure 3-2: CSC FOWT OrcaFlex model.

3.2 Suspended Inter-Array Power Cable

The power cable used in the present study is based on Ye and Yuan (2020). They described a typical power cable used in FOWT farms. This section presents the power cable properties, the setup of the suspended power cable between the FOWTs, the cable ancillaries and the influence of marine growth on the power cable properties.

3.2.1 Cable Properties

The power cable consists of 9 copper conductors and has a total copper cross-sectional area of 1053 mm^2. Each copper conductor is made of 19 copper wires with a diameter of 2.8 mm. The cable is stabilized by 159 armor wires in two layers with a diameter of 5 mm. The armor and copper wires are kept in place by sheaths made of polyethylene, and fillers made of the same material are used to stabilize the power cable. Table 3-1 lists the general properties of

the cable. The cross-section of the utilized cable is shown in Figure 3-3. Figure 3-4 shows the non-linear bending behavior of the power cable obtained with UFLEX.

Table 3-1: Power cable properties.

Core main material	–	Copper
Voltage rating	kV	6-10
Outer diameter	m	0.158
Mass per unit length	kg/m	54.0
Torsional stiffness	kNm^2	375
Axial stiffness	MN	750
Drag coefficient	–	1.2
Added mass coefficient	–	1.0

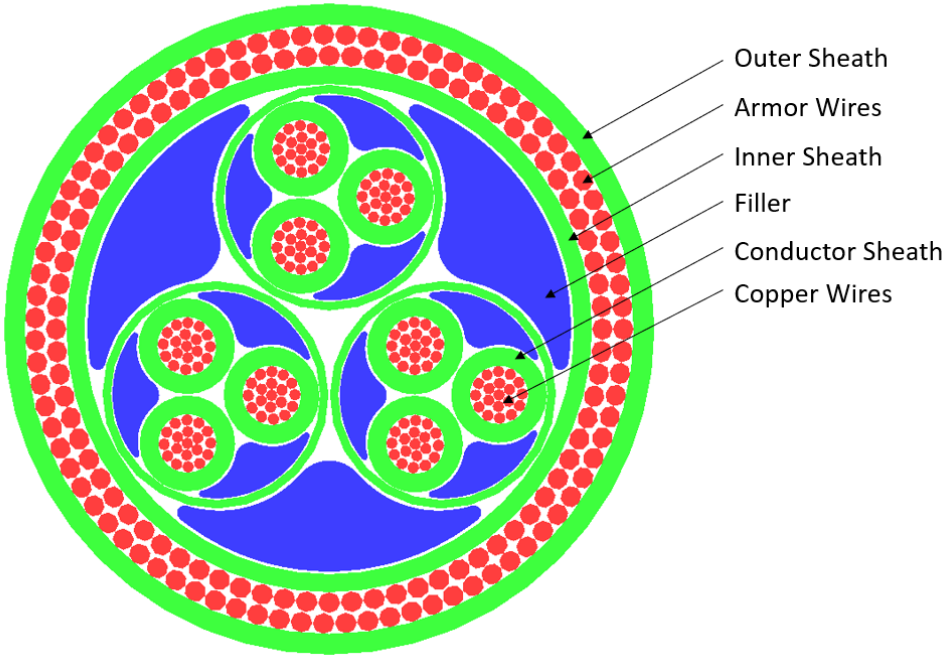

Figure 3-3: Power cable cross-section.

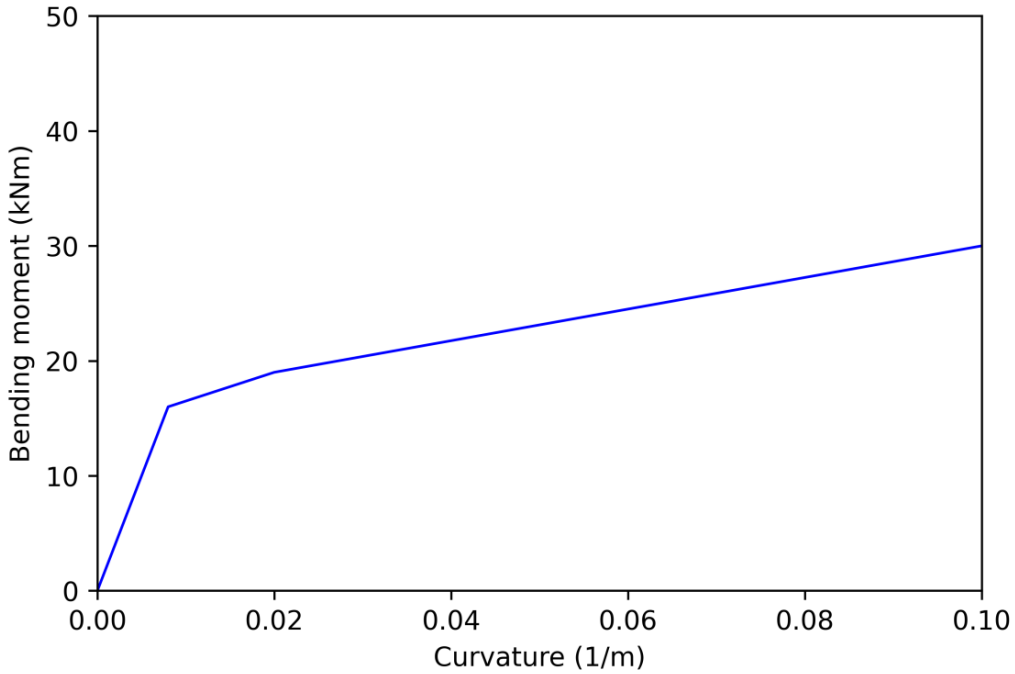

Figure 3-4: Non-linear bending behavior of the power cable.

Figure 3-5 shows the S-N curves for the two power cable components relevant for the fatigue assessment. The curve for the copper wires is taken from Nasution et al. (2014). They established the S-N curve for copper wires in dynamic offshore power cables based on extensive testing and finite element simulations. The curve for the armor wires is based on DNV (2014). Here, the S-N curve called B1 for steel used in offshore applications is selected.

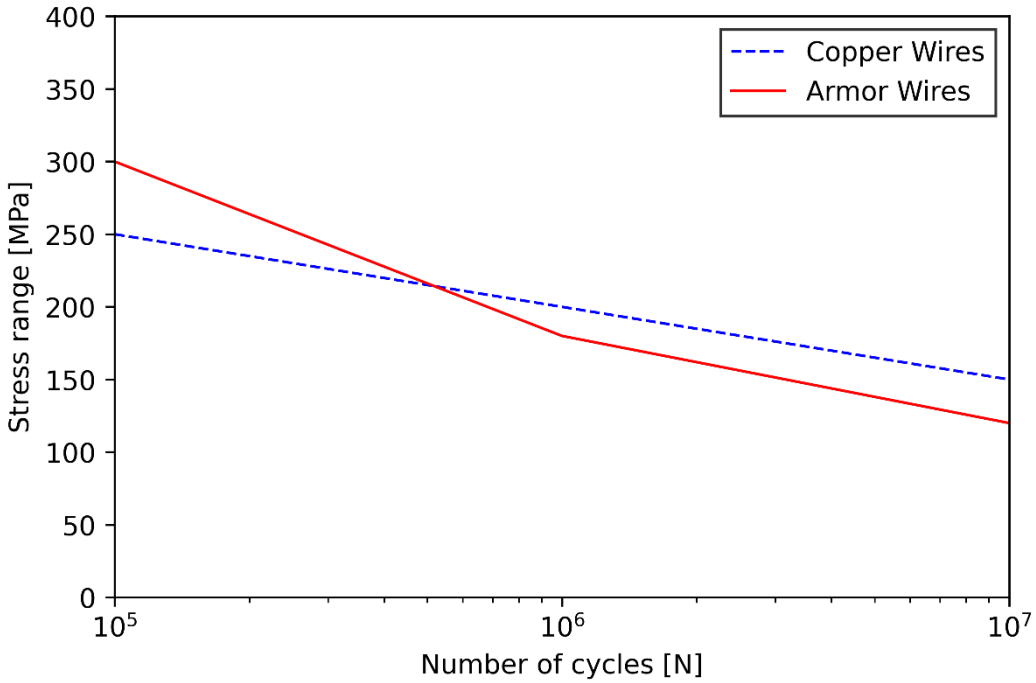

Figure 3-5: S-N curves for the copper and armor wires in the power cable.

3.2.2 Cable Setup and Ancillaries

The inter-array power cable is installed in a suspended way with attached buoys, meaning that it is fully submerged but doesn't touch the seabed. Figure 3-6 shows an exemplary suspended power cable setup. Table 3-2 lists the properties of the subsea buoys attached to the power cable and Figure 3-7 shows one of the used buoys with attached bend stiffeners. The bend stiffeners are included to prevent excessive cable bending due to the upwards force created by the buoys. The surfaces of the buoys and bend stiffeners are equipped with an anti-marine growth coating. The numerical model of the power cable is discretized into elements of different lengths, depending on their location along the cable. The free-hanging cable sections are discretized using a 1.0 m element length, and a segment of 10 m from the hang-off point has an element length of 0.1 m. The cable is separated into elements with sizes of 0.12 m at the bend stiffeners and 0.31 m at the subsea buoy connections. The hang-off point of the power cable is located 30 m below the sea surface and 5.2 m away from the spar buoy center axis. The distance between the two wind turbines is 1134 m, equivalent to 9 times the rotor diameter of the 5 MW turbine model.

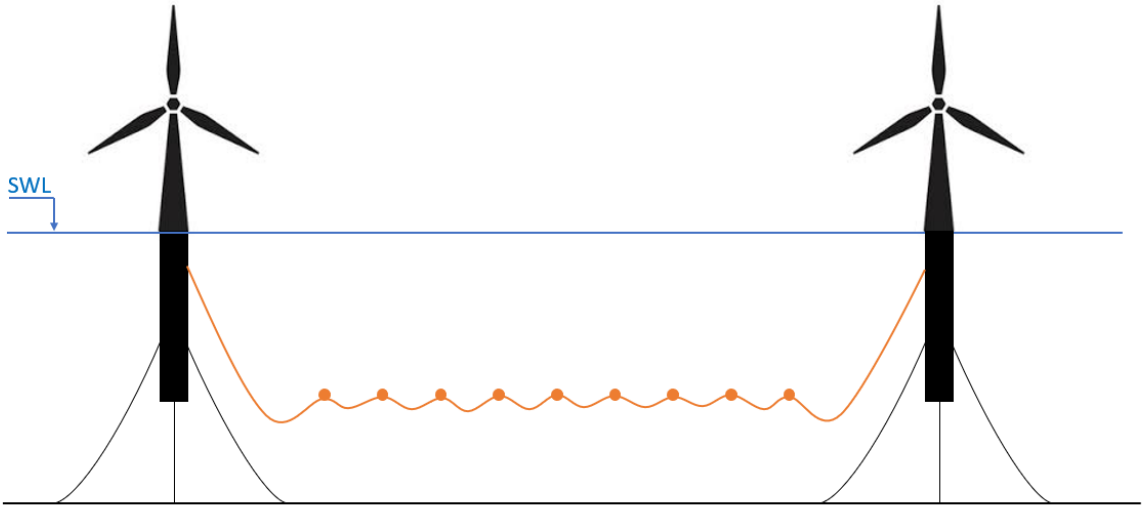

Figure 3-6: Concept of two FOWTs with a suspended power cable.

Table 3-2: Properties of the buoys (Ahmad et al. (2023)).

Length	m	2.170
Volume	m^3	8.615
Mass	kg	2700
Equivalent buoy outer diameter (cylinder shape)	m	2.248
Drag coefficient (normal)	–	0.209
Drag coefficient (axial)	–	1.000
Added mass coefficient (normal)	–	0.459
Added mass coefficient (axial)	–	0.600

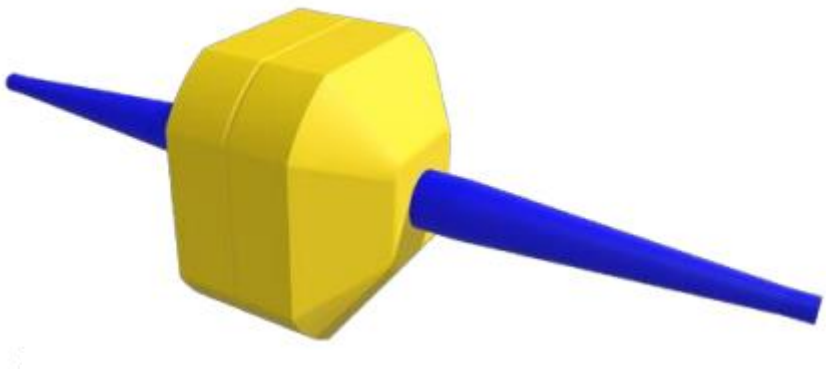

Figure 3-7: Buoy with attached bend stiffeners (reproduced from Ahmad et al. (2023)).

3.2.3 Marine Growth Effects on the Cable

The mass and the diameter of the power cable increase as described in section 2.4.4. The increase in this study is calculated based on the information provided by DNV (2010) and NORSOK (Standards Norway, 2007). Table 3-3 lists the properties of the selected power cable dependent on the marine growth state at the actual water depth. Figure 3-8 shows the drag coefficients based on the Reynolds Number for the normal flow around the cable. The Reynolds Number is here defined as follows:

$$Re = \frac{uD}{\nu} \tag{0-1}$$

where u is the flow velocity, D is the outer diameter of the power cable and ν is the kinematic viscosity of water. A conservative surface roughness of k = 0.01 m is assumed for all marine growth states. The drag coefficient in axial direction is always taken as 0.008 (Orcina Ltd, 2022).

Table 3-3: Marine growth effects on the power cable.

Marine growth state	Water depth (m)	Outer diameter (m)	Mass per unit length (kg/m)
SOL[1]	Below -100	0.158	54.0
EOL[2]1	-100 to -60	0.198	66.3
EOL2	-60 to -40	0.218	73.5
EOL3	-40 to -30	0.258	89.9

[1] SOL = start of life, [2] EOL = end of life

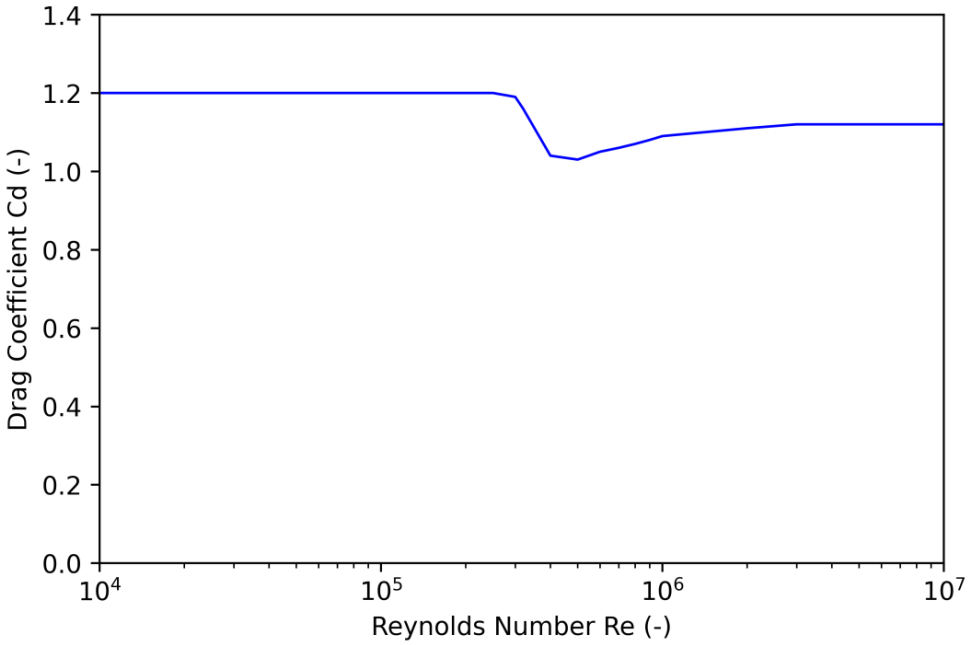

Figure 3-8: Drag coefficients for the power cable (based on ESDU (2007)).

3.3 Environmental Conditions

The environmental conditions of the present study are based on a representative location in the North Sea. The wave, wind and current conditions applied in the case study are presented in Chapter 4 and Chapter 5. One environmental case represents an extreme condition above the cut-out wind speed of the turbine. Therefore, the turbines are idling in the simulations of this load case. To represent irregular waves the JONSWAP spectrum is applied, and the NPD spectrum is applied to simulate the wind conditions. The current profile is determined based on the formulas given in section 2.4.3 and an exemplary current profile is shown in Figure 3-9. Figure 3-10 shows the directions of the environmental loads towards the suspended inter-array power cable setup. The wave, wind and current loads are aligned in all load cases. The nacelles of the FOWTs are rotated so that they always face the incoming wind direction.

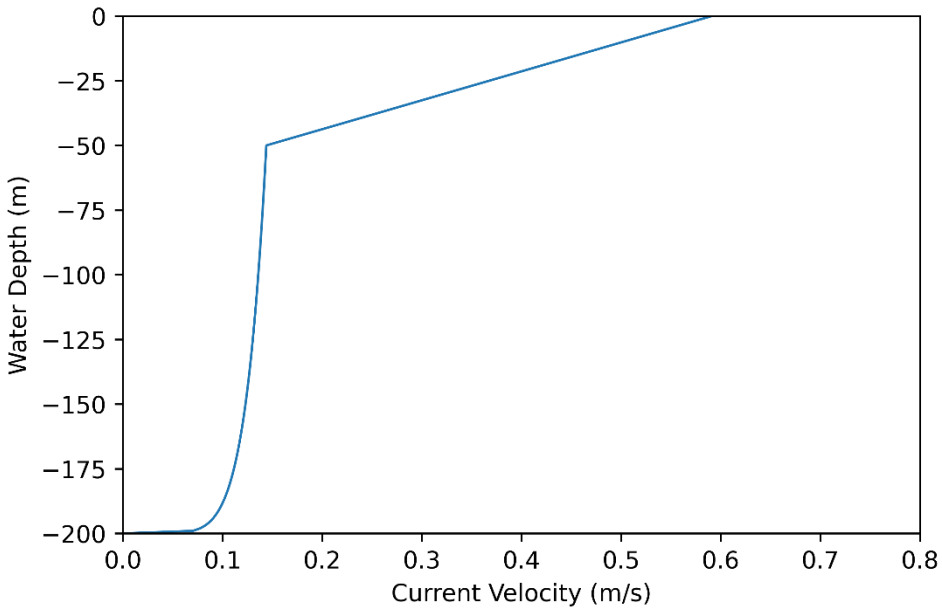

Figure 3-9: Current velocity profile for tidal current of 0.15 m/s and wind velocity of 18 m/s.

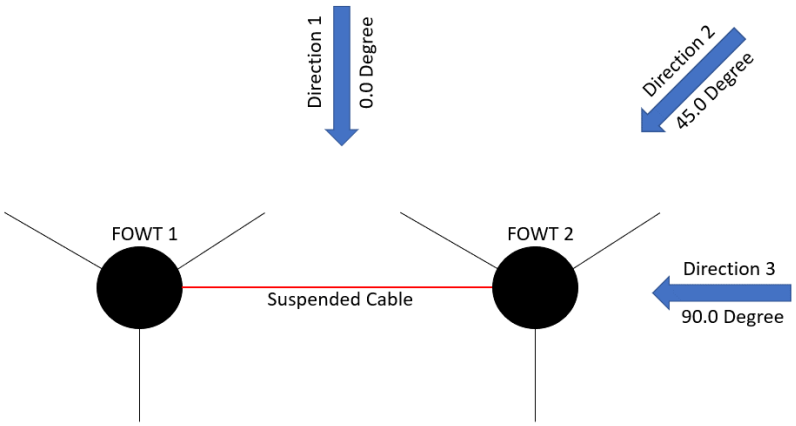

Figure 3-10: Directions of the environmental loads towards the two-turbine setup.

3.4 Case Study Procedure

In the following part, the procedure of the simulations performed during the present study is explained. Figure 3-11 shows the overall procedure of the case study.

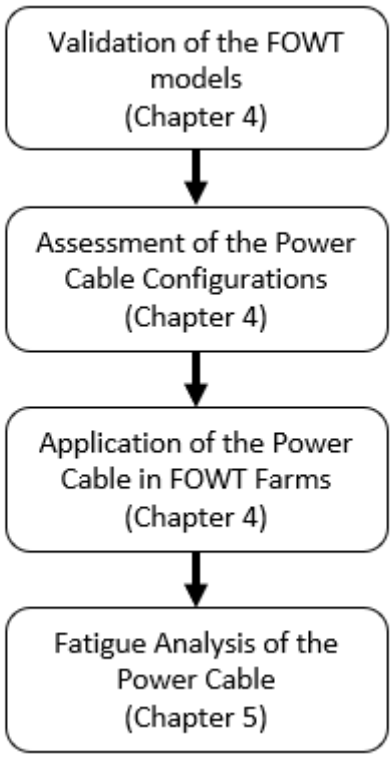

Figure 3-11: Overall case study procedure.

3.4.1 Validation of the Floating Wind Turbine Models

The OC3-Hywind and the CSC FOWT models are validated against reference studies to ensure that their motions are realistic. For both cases, a modal analysis is performed in OrcaFlex to obtain the natural frequencies of the main mode shapes. The added mass of the floaters is included in the modal analysis. Moreover, the RAOs of the FOWTs are determined through a spectral response analysis in OrcaFlex. Here, the results of a random wave time domain simulation with a defined wave frequency range are transformed into a frequency domain using a Fast Fourier Transformation (FFT).

3.4.2 Assessment of the Power Cable Configurations

To find the optimum power cable configuration between two spar type FOWTs, several possible configurations with different cable lengths, numbers of buoys and distances between the buoys are investigated. The configurations are designated according to the following scheme: length – number of buoys – buoy spacing (e.g. L1220m-10B-S100m). The investigated configurations are presented in Chapter 4. Several evaluation stages are performed to assess the suitability of the different configurations. The fitness factor method proposed by Ahmad et al. (2023) is used to determine the best configuration out of all configurations that fulfil the acceptance criteria. The evaluation procedure and the fitness factor method are explained in Chapter 4.

3.4.3 Application of the Power Cable in FOWT Farms

The present study examines the impact of multi-turbine arrangements on the connecting suspended power cables in addition to a standard two-turbine setup as employed by Shi et al. (2022) and Ahmad et al. (2023). The inclusion of these arrangements is more representative of wind farm design than basic two-turbine configurations because wind farms usually have a larger number of turbines. A triangular layout is used for three turbines and a rectangular layout for four turbines. Details about the wind farm layouts are presented in Chapter 4. The Hywind Tampen offshore wind farm's design served as the basis for the mooring lines' orientation (Equinor ASA, 2019).

3.4.4 Fatigue Analysis of the Power Cable

The fatigue assessment is conducted in several stages. First, all load cases are dynamically analyzed in OrcaFlex. Second, the relationships between the power cable's curvature, axial tension, and stresses are determined using UFLEX. Next, these correlations are used to calculate the time histories of the cable stresses. The stress cycles are calculated using the Rainflow Counting method described in section 2.5.3 and the fatigue damage is determined through the Miner-Palmgren rule presented in section 2.5.4. Further information about the fatigue assessment procedure as well as the investigated power cable configurations is presented in Chapter 5.

Chapter 4 - Application of a Suspended Inter-Array Power Cable in Floating Offshore Wind Farms

Dennis Beier [a], Muk Chen Ong [a], Marek Jan Janocha [a], Naiquan Ye [b]

[a] Department of Mechanical and Structural Engineering and Materials Science, University of Stavanger, Stavanger, Norway

[b] SINTEF Ocean, Trondheim, Norway

This content is under review in Applied Ocean Research as:

Beier, D., Ong, M. C., Janocha, M. J., & Ye, N. (2023). Application of a Suspended Inter-Array Power Cable in Floating Offshore Wind Farms.

Abstract

The aim of the present paper is to explore the use of suspended inter-array power cables in floating offshore wind farms. To achieve this, a spar type and a semi-submersible type floating offshore wind turbines (FOWTs) are modeled in the dynamic analysis software OrcaFlex. The accuracy of these models is validated against reference studies. Several different cable configurations connecting two spar FOWTs are assessed based on Fitness Factors using static and dynamic analyses. The non-linear bending behavior and the marine growth effects are considered in the analyses. The number of buoys is found to be the main parameter affecting the maximum effective tension and the minimum bending radii of the cables. The buoy spacing determines whether the cable touches the seabed, floats fully submerged, or floats at the sea surface. The influence of the cable length and the marine growth on the observed cable tensions and curvatures is small for the investigated configurations. The optimum cable configuration found for the two spar FOWTs is employed to connect two semi-submersible FOWTs. The influence of the floater type on the suspended power cable tension and curvature is found to be negligible. Analysis of power cable behavior in different offshore wind farm layouts shows that a two-turbine setup with different environmental load directions is representative of the suspended power cables design in entire wind farms.

Keywords: Suspended power cable, inter-array cable configuration, floating offshore wind turbine, offshore wind farm, OC3 Hywind, CSC FOWT

4.1 Introduction

Renewable energy sources are necessary to reduce the emissions of greenhouse gases and limit global warming. One of the most abundant sources of renewable energy is wind. Land-based and bottom-fixed offshore wind turbines have been used for several decades to provide power to consumers across the globe. In recent years, there has been a growing interest in floating offshore wind turbines (FOWTs) because they can harness higher wind speeds found in deeper waters. Several floating wind projects have already been implemented, such as Hywind Scotland and Hywind Tampen, which are based on spar platforms (Eldøy (2017); Equinor ASA (2019)) and Kincardine Offshore Wind Farm, which uses semi-submersible platforms (Principle Power Inc. (2023)). In all of these projects, the inter-array power cables are laid on the seabed. However, it is also possible to install the power cables in a submerged manner without them touching the seabed. This approach called a suspended installation, can reduce the length of the power cables, resulting in lower investment costs and a decreased inter-array energy loss (Ahmad et al. (2023)).

Ikhennicheu et al. (2020) presented different configurations for dynamic power cables connecting a floating platform to a transition joint. The two most commonly described configurations in the literature are the catenary shape and the lazy-wave shape. The lazy-wave configuration is distinguished from the catenary configuration by the inclusion of buoyancy modules attached to the power cable. Thies et al. (2019) analyzed different lazy-wave cable configurations, and found that a lowered buoyancy section (buoyancy section is installed closer to the seabed) leads to a better balance between hang-off tensions and bending stresses. In an effort to optimize the power cable configuration, Rentschler et al. (2019) proposed a genetic algorithm approach to find the optimal inter-array layout. They compared the tensions and curvatures of the cable for various buoyancy element distributions and successfully reduced the total length of the buoyancy sections significantly. Rentschler et al. (2020) conducted an optimization study for lazy-wave configurations in a steady-state condition using a fitness factor approach. The fitness factor was established based on the relation between the bending radii and the tensions of the cable with their allowable values. Their optimization study has reduced the maximum cable tensions of the lazy-wave configurations by up to 50%. Rapha and Dominguez (2021) proposed a fully suspended power

cable as an alternative solution to laid cables. Different suspended power cable configurations between two FOWTs were analyzed by Schnepf et al. (2023). They observed that cables with buoys attached at individual points have significantly lower effective tensions than cables with buoyancy modules attached along cable sections. Shi et al. (2022) evaluated the performance of short dynamic power cables with attached buoyancy modules connecting a pair of FOWTs in extreme conditions. The buoyancy elements were found to be the main parameter influencing the curvature and tension of the power cable. The behavior of a suspended power cable coupling a FOWT with a floating production storage and offloading unit (FPSO) was investigated by Schnepf et al. (2022). Their analysis showed that the configuration with evenly distributed buoys attached to the power cable was superior to configurations with a freely hanging power cable and a power cable with buoys attached to its middle section in term of observed tensions. Ahmad et al. (2023) established a design approach for suspended inter-array power cable configurations between two FOWTs. One of the proposed methods for reducing the maximum tensions in the power cable was attaching several buoys. Additionally, their study found that copper conductors were a more suitable material for suspended power cables compared to aluminum conductors.

To the best of authors' knowledge, no prior research has been conducted to evaluate the effectiveness of a suspended power cable used between varying types of floating offshore wind turbines (FOWTs), nor has there been an assessment of their performance within an entire wind farm. This study aims to fill this gap by investigating the suspended application of actual dynamic offshore power cables in wind farms, specifically for different types of FOWTs.

This paper is structured as follows: In Section 2, a detailed description of the methodology employed in this study is provided, including the physical parameters of the modeled structures and the numerical setup. The two analyzed types of FOWTs, the layouts of the wind farms under consideration, as well as the properties of the suspended power cable, and the environmental conditions considered, are outlined. In Section 3, the responses of the FOWTs and the results of the suspended power cable case study are presented and analyzed. In this section, also the implications of the present findings are discussed. Finally, the summary of the present study's key findings is presented in Section 4.

4.2 Methodology and Numerical Setup

In this section, a comprehensive description of the numerical setup utilized for the present study is provided. This includes the modeling and simulation of both the FOWTs and the suspended power cables, as well as the environmental conditions that are considered. The procedure followed for the present case study to ensure the accuracy and reproducibility of the results is also outlined. All of the simulations in the present study are carried out using the dynamic analysis software OrcaFlex version 11.2d (Orcina Ltd (2022)).

4.2.1 OC3-Hywind FOWT

The spar type FOWT considered in the present study is the 5 MW OC3-Hywind design described by Jonkman et al. (2009) and Jonkman (2010). Figure 4-1 shows the geometry of the OC3-Hywind FOWT, and Table 4-1 lists its general parameters. To facilitate a direct comparison with the second considered floater type – a semi-submersible CSC FOWT design (Luan et al. (2016)), the water depth is changed from the 320 m depth defined by Jonkman (2010) to 200 m. The mooring line properties are adjusted to values appropriate for the shallower water depth. These properties are detailed in Table 2.

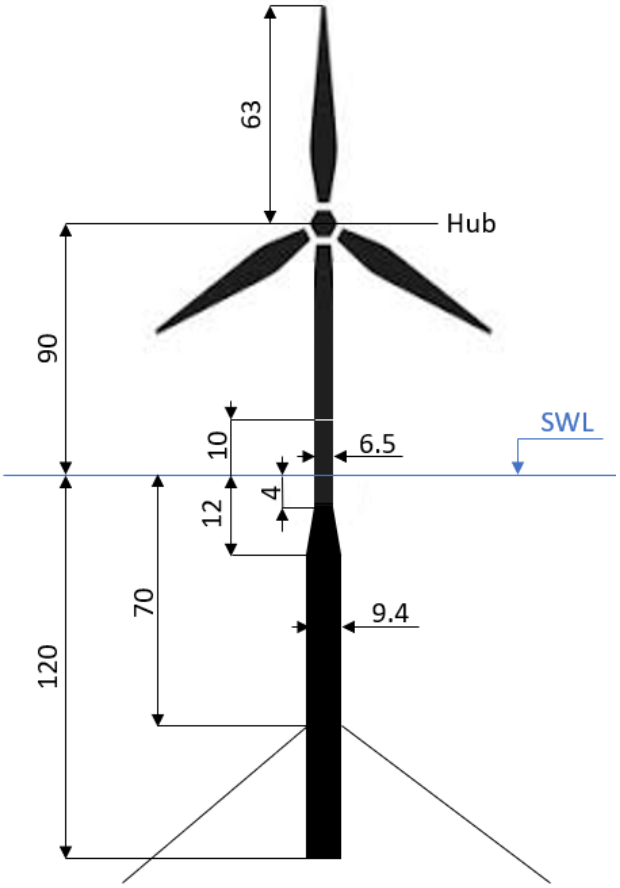

Figure 4-1: OC3-Hywind FOWT geometry. Dimensions in m.

Table 4-1: OC3-Hywind FOWT specifications (based on Jonkman et al. (2009) and Jonkman (2010)).

Rotor orientation, configuration	-	Upwind, 3 blades
Rotor diameter	m	126
Hub diameter	m	3
Hub height	m	90
Cut-in, rated, cut-out wind speeds	m/s	3, 11.4, 25
Platform diameter	m	6.5 to 9.4 (tapered)
Rotor mass	kg	110000
Nacelle mass	kg	240000
Tower mass	kg	249718
Platform mass, including ballast	kg	7466330
Spar COG[1] below SWL[2] along platform centerline	m	89.9155
Platform total draft	m	120
Water depth	m	200

[1] COG = Center of gravity, [2] SWL = Still water level

Table 4-2: OC3-Hywind FOWT Mooring Line Properties.

Number of mooring lines	-	3
Angle between mooring lines	°	120
Mass per unit length	kg/m	152.9
Mooring line length	m	502.2
Depth to fairleads below SWL	m	70.0
Radius to fairleads from platform centerline	m	5.2
Radius to anchors from platform centerline	m	473.8
Mooring line diameter	m	0.09
Mooring Line Extensional Stiffness	N	384243000
Additional Yaw Spring Stiffness	Nm/rad	98340000

4.2.2 CSC FOWT

The braceless steel 5 MW CSC FOWT is used as the semi-submersible FOWT considered in this study. This 5 MW CSC design basis is provided by Luan et al. (2016). The hull consists of a central column, three side columns and three pontoons. Figure 4-2 shows the geometry of the CSC FOWT, and Table 4-3 lists its general properties. It is equipped with the same NREL 5 MW turbine as the OC3-Hywind FOWT. The mooring line properties for the CSC FOWT are described in Table 4-4.

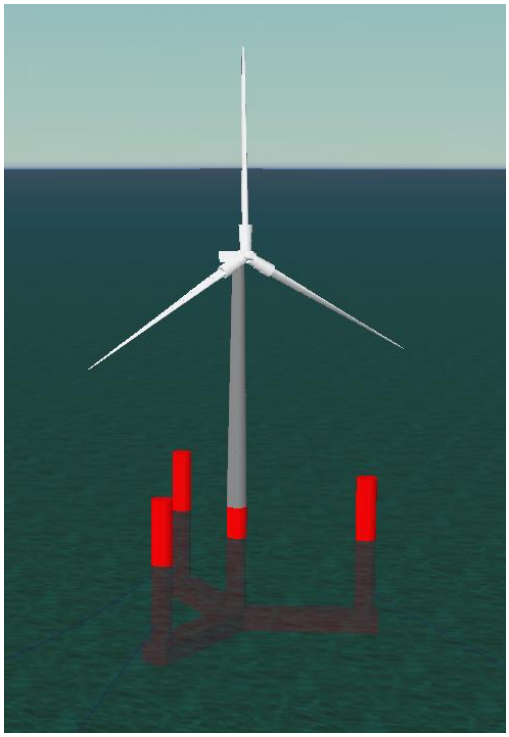

Figure 4-2: CSC FOWT geometry.

Table 4-3: CSC FOWT specifications (based on Luan et al. (2016) and Jonkman et al. (2009)).

Rotor orientation, configuration	-	Upwind, 3 blades
Rotor diameter	m	126
Hub diameter	m	3
Hub height	m	90
Cut-in, rated, cut-out wind speeds	m/s	3, 11.4, 25
Column diameter	m	6.5
Pontoon height	m	6
Pontoon width	m	9
Rotor mass	kg	110000
Nacelle mass	kg	240000
Tower mass	kg	249718
Platform mass, including ballast	kg	9738000
Platform COG below SWL along centerline	m	24.36
Platform total draft	m	30
Water depth	m	200

Table 4-4: CSC FOWT Mooring Line Properties (based on Luan et al. (2016)).

Number of mooring lines	-	3
Angle between mooring lines	°	120
Mass per unit length	kg/m	115
Mooring line length	m	1073
Depth to fairleads below SWL	m	18
Radius to fairleads from platform centerline	m	44.3
Radius to anchors from platform centerline	m	1084.4
Mooring line diameter	m	0.137
Clump weight in water	kg	15000
Distance from the attachment point of the clump weight to the fairlead (along the mooring line)	m	240

4.2.3 Wind Farm Layout

In addition to a typical two-turbine setup as used by Shi et al. (2022) and Ahmad et al. (2023), the present study also investigates the influence of multi-turbine arrangements on the connecting suspended power cables. Since wind farms usually consist of a larger number of turbines, the inclusion of these setups is more representative for wind farm design than simple two-turbine configurations. The setup and the directions of the wave, wind, and current loads for two wind turbines are shown in Figure 4-3. For three turbines, a triangular layout is

selected and for four turbines a rectangular layout. Figure 4-4 and Figure 4-5 show these setups and the directions of the considered environmental loads. The orientation of the mooring lines is based on the layout used in the Hywind Tampen offshore wind farm (Equinor ASA (2019)). The distance between the individual wind turbines is 1134 m, equivalent to 9 times the rotor diameter of the model 5 MW turbine considered in the present study.

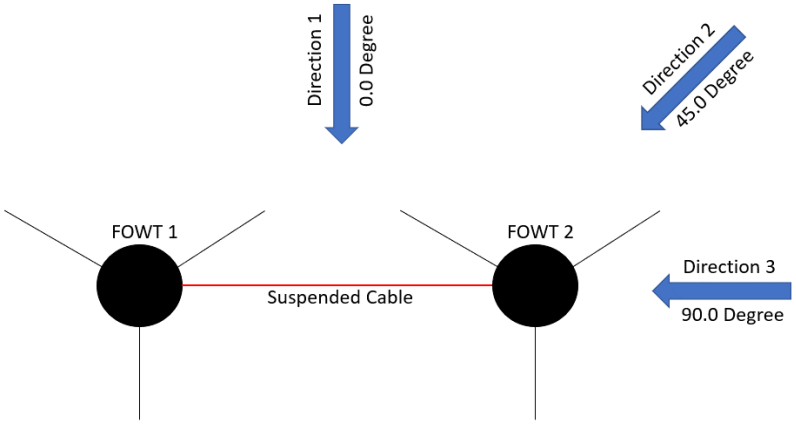

Figure 4-3: Two FOWTs setup.

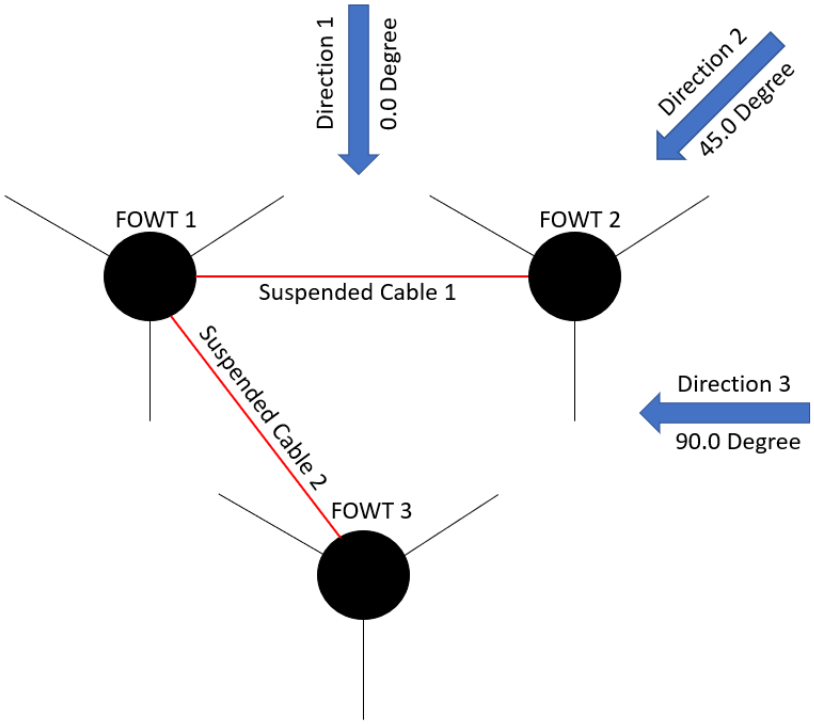

Figure 4-4: Triangular setup with three FOWTs.

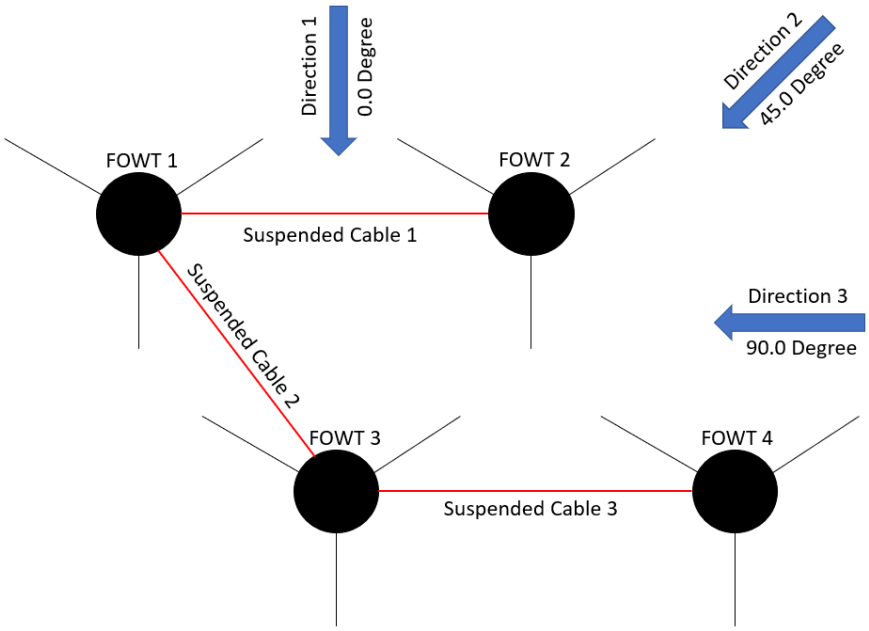

Figure 4-5: Rectangular setup with four FOWTs.

4.2.4 Environmental Conditions

The wave, wind and current conditions applied in this study are based on a representative location in the North Sea. For the dynamic simulations, two different environmental cases are considered. Table 4-5 lists all environmental parameters for these cases. Environmental case (EC) 2 represents an extreme weather condition where the wind turbine is idling. In EC1 the FOWT is in operation. The JONSWAP spectrum is used to simulate irregular waves, and the NPD spectrum is applied to model the wind (Orcina Ltd (2022)). The current velocity at a specific height *z* is estimated through the following formula given by DNV (2010):

$$v_c(z) = v_{c,tide}(0)\left(\frac{d+z}{d}\right)^{\frac{1}{7}} + v_{c,wind}(0)\left(\frac{d_0+z}{d_0}\right) \quad (4\text{-}1)$$

where $v_{c,tide}$ is the tidal current at the still water level, $v_{c,wind}$ is the wind generated current at the still water level, d is the water depth and d_0 is the reference depth for wind generated current. This reference depth is defined as 50 m. Below this depth the wind generated current is neglected, so $v_{c,wind}$ is equal to zero. The wind generated current at the still water level is determined based on the reference wind speed (DNV (2010)):

$$v_{c,wind}(0) = k * U_{1\,hour,10m} \quad (4\text{-}2)$$

where $U_{1\ hour,10m}$ is the 1 hour sustained wind speed at a height 10 m above the sea level and *k* is equal to 0.03. The three considered environmental loads directions relative to the FOWTs and power cables are shown in Figure 4-3, Figure 4-4 and Figure 4-5. Wind, waves and current are aligned in all load cases.

Table 4-5: Environmental data.

Load case	Wave H_s (m)	Wave T_p (s)	Tidal current at SWL (m/s)	Windspeed at hub height (m/s)
EC1	2.88	9.98	0.1	10
EC2	6.02	11.38	0.2	26

4.2.5 Power Cable Properties

The power cable properties used in this work are adopted from Ye and Yuan (2020). The power cable consists of 9 copper conductors with 19 wires each and has a total copper cross-section of 1053 mm^2. The properties of the power cable are listed in Table 4-6. Figure 4-6 shows the cross-section of the power cable. The bending moment versus capacity curve of the cable is computed in UFLEX (SINTEF (2018)) to include its non-linear bending behavior. The finite element software UFLEX enables the determination of power cable properties by modelling its cross-section. The resultant bending moment versus capacity curve is shown in Figure 4-7.

Table 4-6: Power cable properties.

Core main material	–	Copper
Voltage rating	kV	6-10
Outer diameter	m	0.158
Mass per unit length	kg/m	54.0
Torsional stiffness	kNm^2	375
Axial stiffness	MN	750
Added mass coefficient	–	1.0

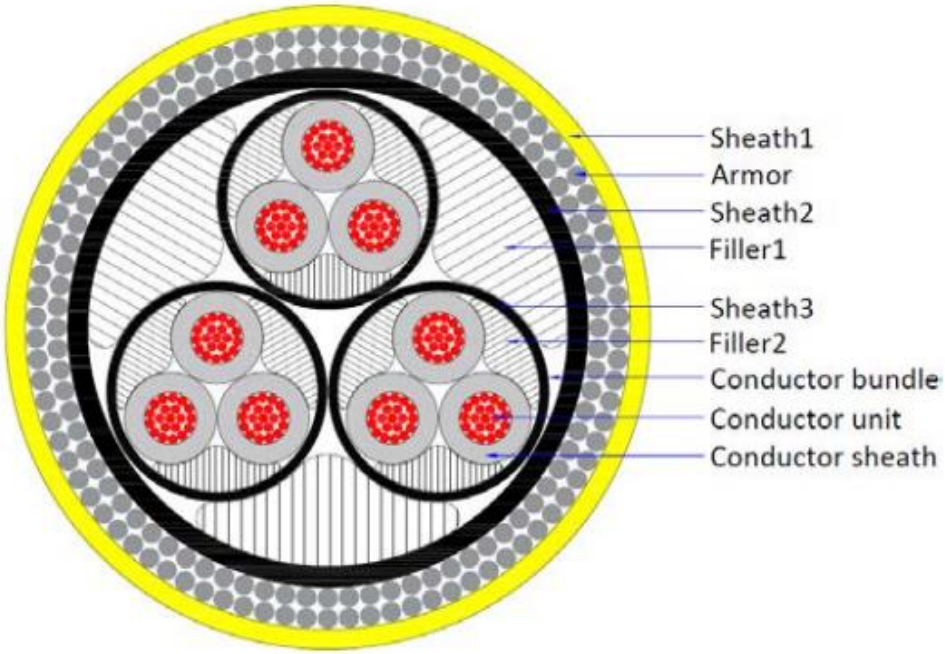

Figure 4-6: Power cable cross section (reproduced from Ye and Yuan (2020)).

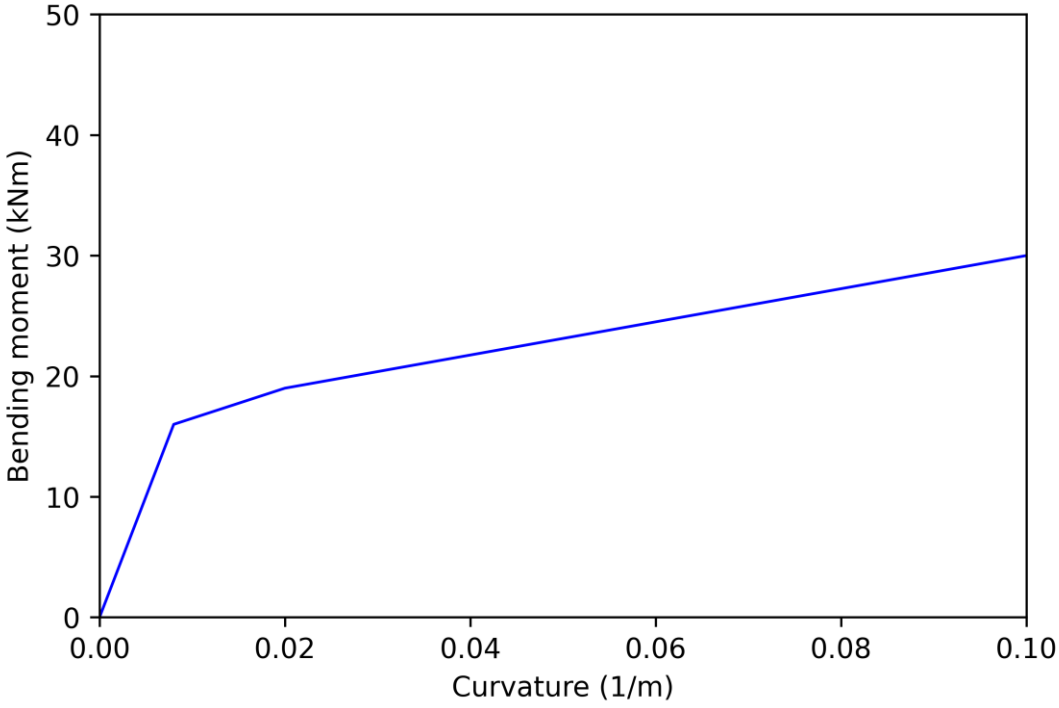

Figure 4-7: Non-linear bending behavior of the power cable.

Due to marine growth, the diameter, weight and drag coefficients of the power cable change during its lifetime. Furthermore, the marine growth is dependent on the water depth. The

marine growth effects in this study are calculated based on the information provided by NORSOK (Standards Norway (2007)) and DNV (2010). Table 4-7 lists the Start-of-Life (SOL) state and End-of-Life (EOL) state properties of the power cable. The drag coefficients in normal direction dependent on the Reynolds Number are shown in Figure 4-8. The Reynolds Number is here defined as:

$$Re = \frac{uD}{\nu} \tag{4-3}$$

where u is the flow velocity, D is the outer diameter of the power cable and ν is the kinematic viscosity of water. A conservative surface roughness of k = 0.01 m is assumed for all marine growth states. The drag coefficient in axial direction is always taken as 0.008 (ESDU (2007)).

Table 4-7: Power cable properties with marine growth.

Marine growth state	Water depth (m)	Outer diameter (m)	Mass per unit length (kg/m)
SOL	Below -100	0.158	54.0
EOL1	-100 to -60	0.198	66.3
EOL2	-60 to -40	0.218	73.5
EOL3	-40 to -30	0.258	89.9

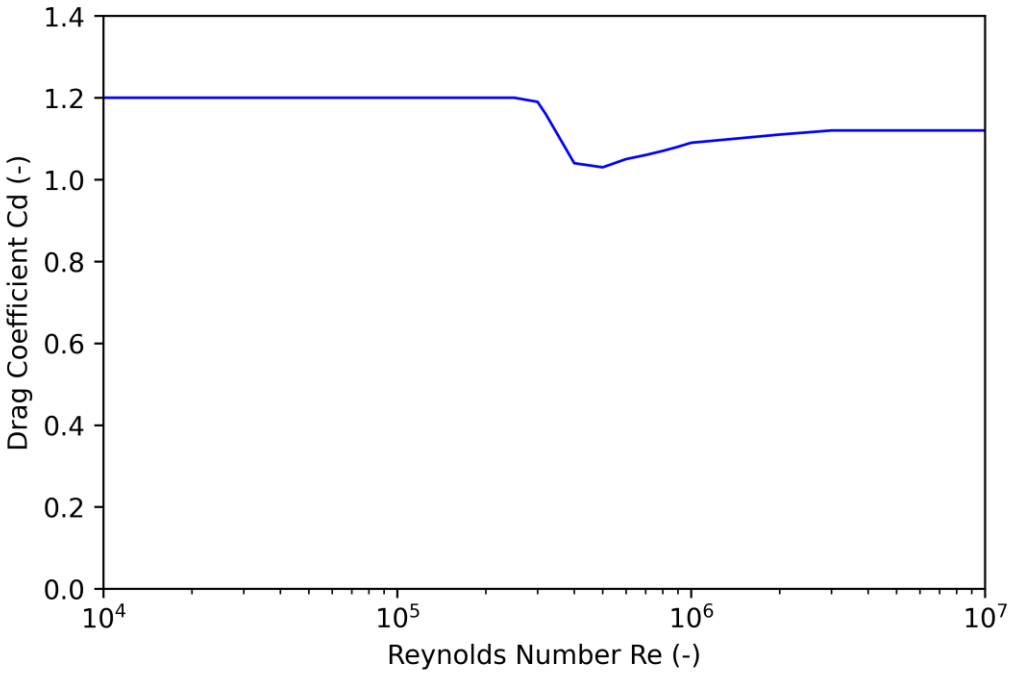

Figure 4-8: Drag coefficients for the power cable (based on ESDU (2007)).

4.2.6 Suspended Inter-Array Power Cable Setup

The inter-array power cable connecting the two FOWTs is in suspended configuration, which means that the cable does not touch the seabed or sea surface. An exemplary suspended power cable setup is shown in Figure 4-9. The different power cable configurations investigated in the present study are listed in Table 4-9. A total number of 36 cases is assessed. The cable is discretized into elements of different sizes dependent on their location along the cable. A section of 10 m from the hang-off location has an element length of 0.1 m, and the free-hanging cable sections are discretized using 1.0 m element length. There are several buoys attached to the cable. Table 4-8 lists the properties of the buoys. Bend stiffeners are attached to both ends of each buoy to prevent excessive cable bending. The cable is divided into elements with length of 0.31 m at the subsea buoy connection and 0.12 m at the bend stiffeners. The buoys and the bend stiffeners are equipped with an anti-marine growth coating. The power cable hang-off point is located 30 m below the still water level (SWL) and 5.2 m away from the column center axis. The nacelles of the wind turbines always face the incoming wind direction.

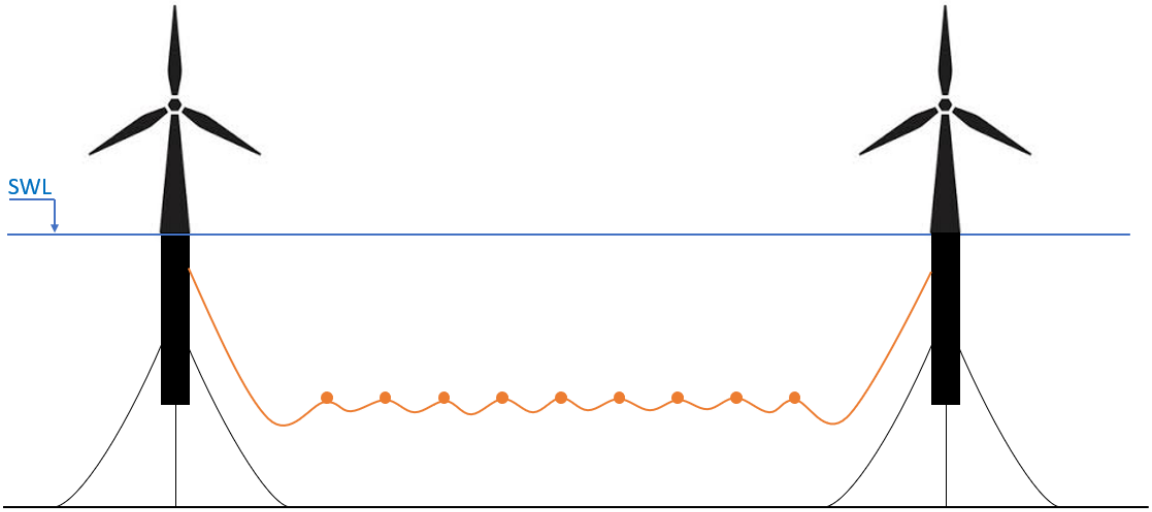

Figure 4-9: Concept of two FOWTs with a suspended power cable.

Table 4-8: Properties of the buoys (Ahmad et al. (2023)).

Length	m	2.170
Volume	m^3	8.615
Mass	kg	2700
Equivalent buoy outer diameter (cylinder shape)	m	2.248
Drag coefficient (normal)	–	0.209
Drag coefficient (axial)	–	1.000
Added mass coefficient (normal)	–	0.459
Added mass coefficient (axial)	–	0.600

Table 4-9: Suspended power cable configurations parameters.

Parameter	Unit	Min	Max	Step
Length	m	1240	1260	20
Number of buoys	-	8	10	1
Buoy spacing	m	80	130	10

4.2.7 Case Study Procedure

The different suspended power cable configurations are investigated using the procedure shown in Figure 4-10. This process is based on the approach presented by Ahmad et al. (2023). Table 4-10 lists the acceptance criteria for the analysis. To determine the optimum cable configurations, the fitness factor method proposed by Ahmad et al. (2023) is applied. The fitness factor is calculated as:

$$Normalized\ MBR = \frac{2.5\ m}{MBR} \quad (4\text{-}4)$$

$$Normalized\ MBL = \frac{MBL}{90\ kN} \quad (4\text{-}5)$$

$$Fitness\ Factor = Normalized\ MBR + Normalized\ MBL \quad (4\text{-}6)$$

The optimal configuration is found by minimizing the fitness factor value. After the procedure shown in Figure 4-10 is completed, the optimum cable configuration is investigated between the CSC turbines as well as in the triangular and rectangular wind farms.

Table 4-10: Acceptance Criteria.

Criteria	Unit	Limit
Minimum bend radius (MBR)	m	2.5
Minimum breaking load (MBL)	N	90000
Minimum seabed clearance	m	10
Minimum sea surface clearance	m	30

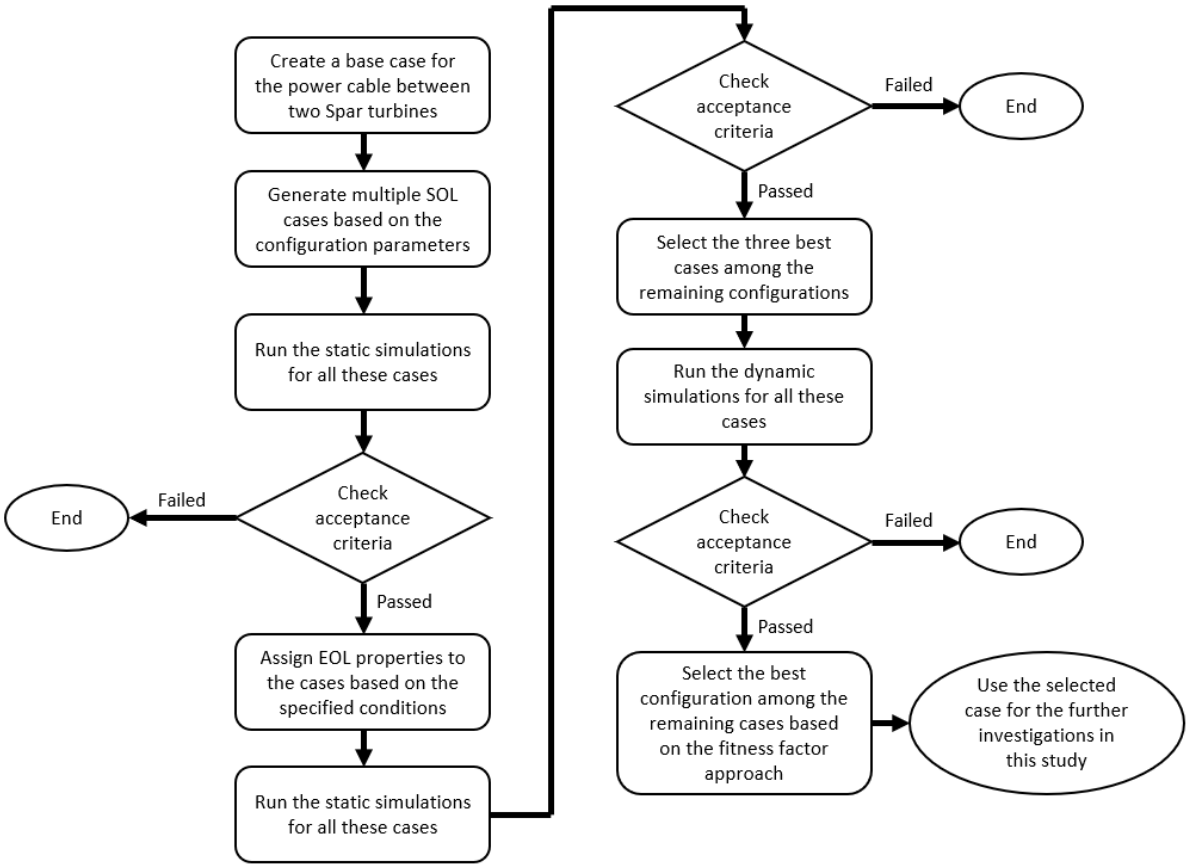

Figure 4-10: Suspended cable configuration case study procedure.

4.3 Results and discussion

This section shows the response analysis results of the two different types of FOWTs. Moreover, the suspended power cable configuration case study results are presented. Also, the outcomes of the investigation of the suspended power cable usage between semi-submersible FOWTs and in larger wind farms are shown.

4.3.1 Response of the OC3-Hywind FOWT

The response of the OC3-Hywind FOWT is calculated for two different OrcaFlex models. One model has the exact same water depth and mooring configurations as specified by Ramachandran et al. (2013). The other model uses the setup presented in Section 2.1. Table 4-11 shows the six lowest natural frequencies of the FOWT. The results from the OrcaFlex models are in close agreement with the frequencies determined by Ramachandran et al. (2013). Figure 4-11 shows the response amplitude operator (RAO) for surge motion, Figure 4-12 shows the RAO for heave motion, and Figure 4-13 shows the RAO for pitch rotation. The RAOs of the OrcaFlex models are similar to the ones determined by Ramachandran et al. (2013) with the hydrodynamic analysis software WAMIT. It should be noted that the RAOs predicted by the present model are determined using time-domain simulations. Hence the present RAOs plot is not smooth such as the RAO plot obtained from frequency domain simulations with WAMIT. In Figure 4-12, the model with a water depth of 200 m has a slightly different heave motion RAO due to its modified mooring system.

Table 4-11: OC3-Hywind Natural Frequencies.

Mode	Surge (Hz)	Sway (Hz)	Heave (Hz)	Roll (Hz)	Pitch (Hz)	Yaw (Hz)
Ramachandran et al. (2013)	0.008	0.008	0.032	0.034	0.034	0.121
320 m OrcaFlex Model	0.0077	0.0085	0.0323	0.0332	0.0334	0.1200
200 m OrcaFlex Model	0.0078	0.0089	0.0326	0.0330	0.0333	0.1177

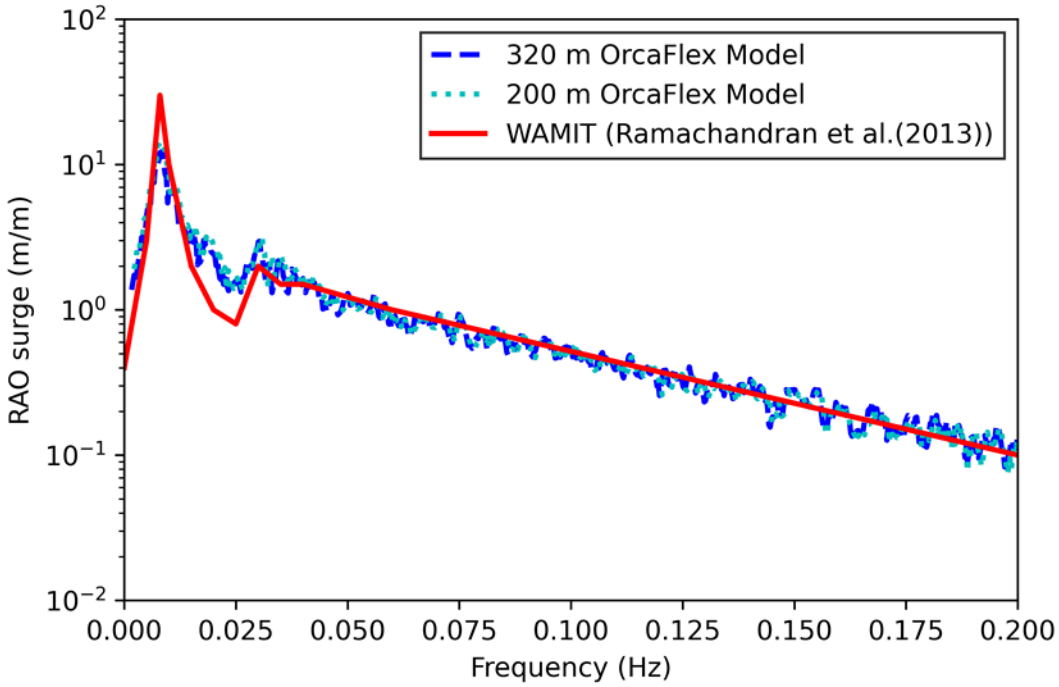

Figure 4-11: OC3-Hywind Surge RAO comparison.

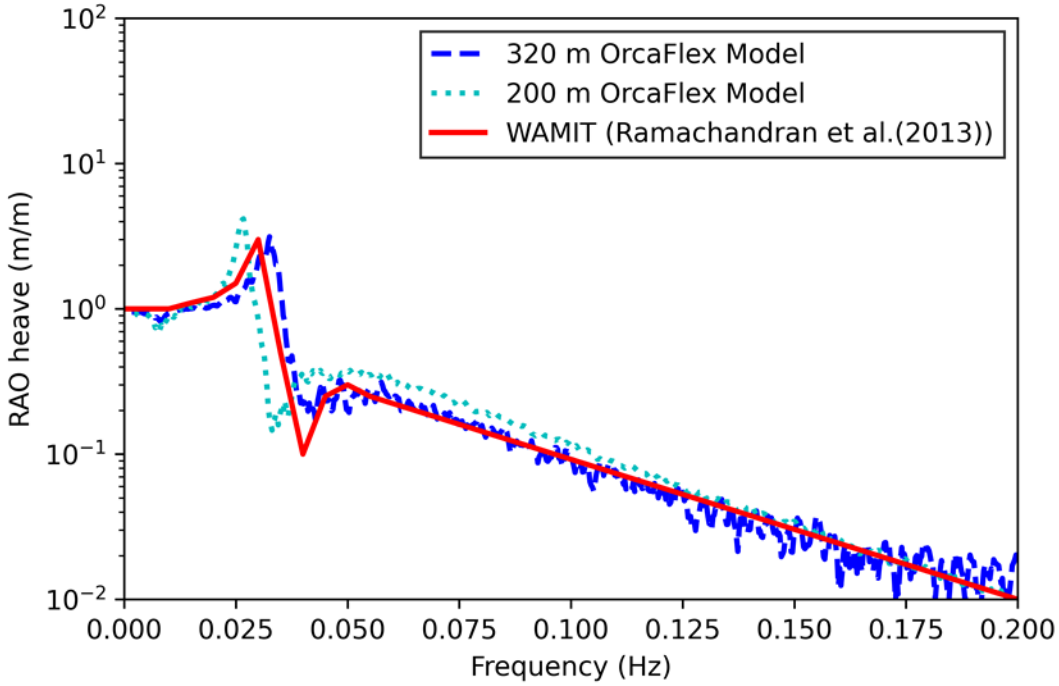

Figure 4-12: OC3-Hywind Heave RAO comparison.

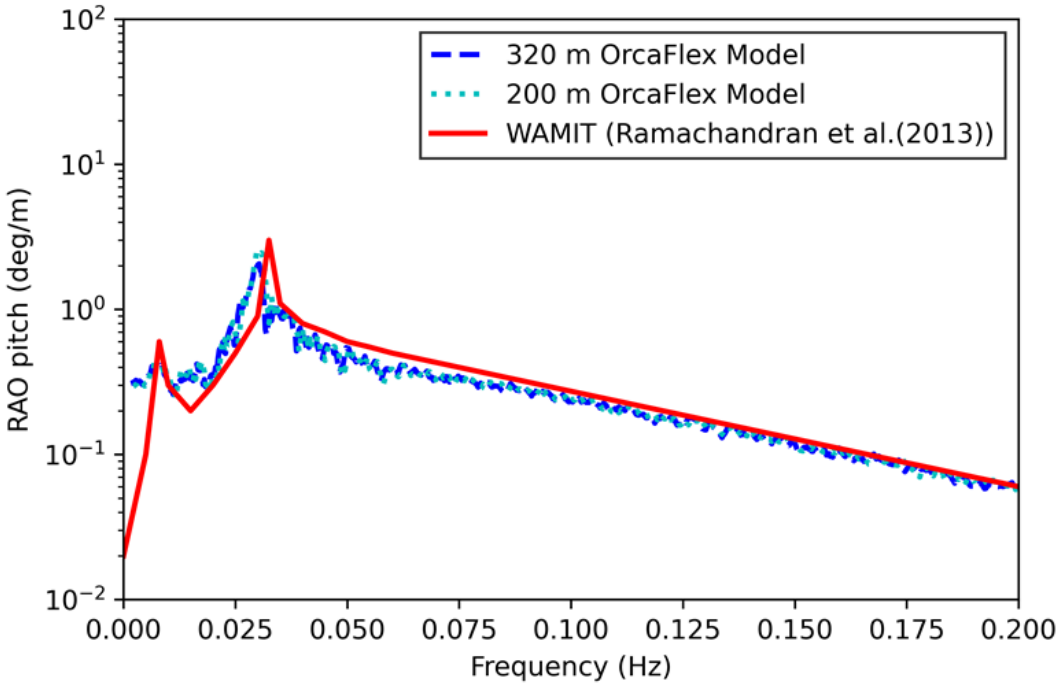

Figure 4-13: OC3-Hywind Pitch RAO comparison.

4.3.2 Response of the CSC FOWT

Table 4-12 lists the natural frequencies of the present OrcaFlex model for the CSC FOWT as well as the natural frequencies obtained by Luan et al. (2016). The results of both studies align with each other. Figure 4-14 and Figure 4-15 show the RAOs of the CSC FOWT for the present model and for the model used by Luan et al. (2016). In both cases, the mooring lines are neglected since their effect on the responses is small, according to Luan et al. (2016). The RAOs of the present OrcaFlex model are very similar to the ones obtained by the reference study (Luan et al. (2016)). Figure 4-16 and Figure 4-17 show the heave and pitch RAOs for the OrcaFlex model of the CSC FOWT for a case including mooring lines and a case neglecting the mooring lines. The effects of the mooring lines on the time-domain simulation of the responses are visible due to the oscillations in the graph. While the influence of the mooring lines on the heave RAO is small, there is a significant impact on the pitch RAO of the CSC FOWT.

Table 4-12: CSC Natural Frequencies.

Mode	Surge (Hz)	Sway (Hz)	Heave (Hz)	Roll (Hz)	Pitch (Hz)	Yaw (Hz)
Luan et al. (2016)	0.0126	0.0126	0.0388	0.0320	0.0320	0.0172
OrcaFlex Model	0.0124	0.0128	0.0387	0.0317	0.0316	0.0171

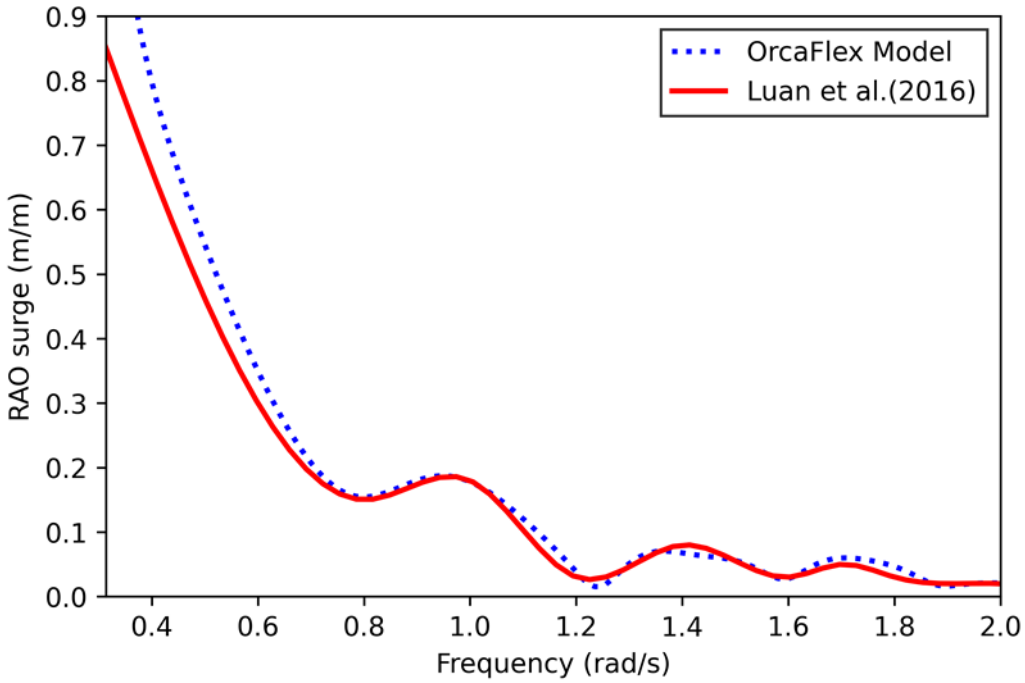

Figure 4-14: CSC Surge RAO comparison.

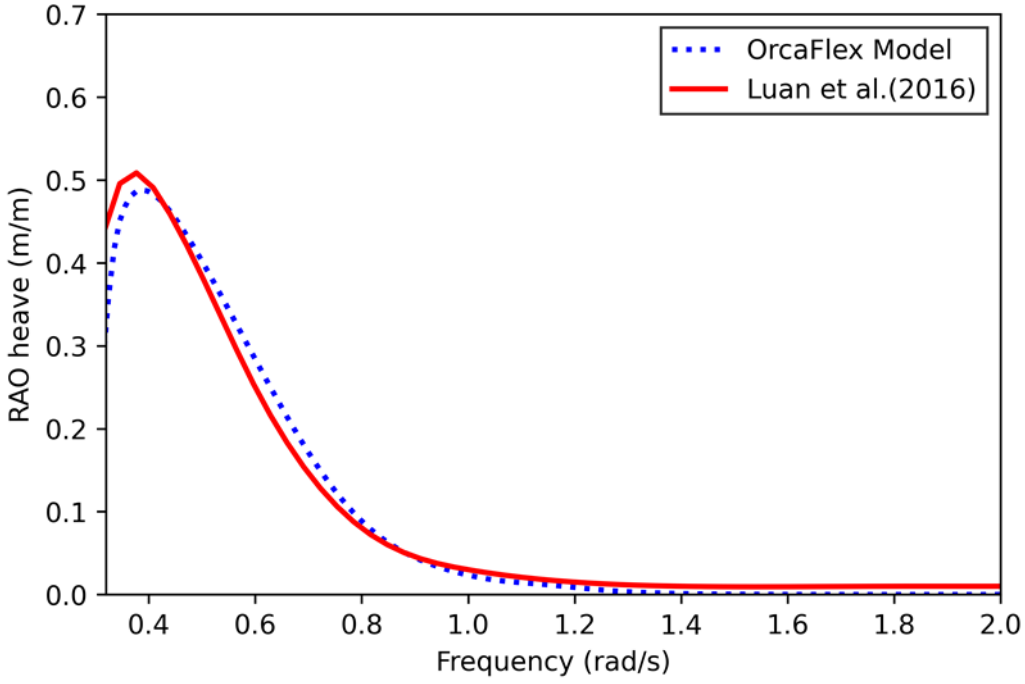

Figure 4-15: CSC Heave RAO comparison.

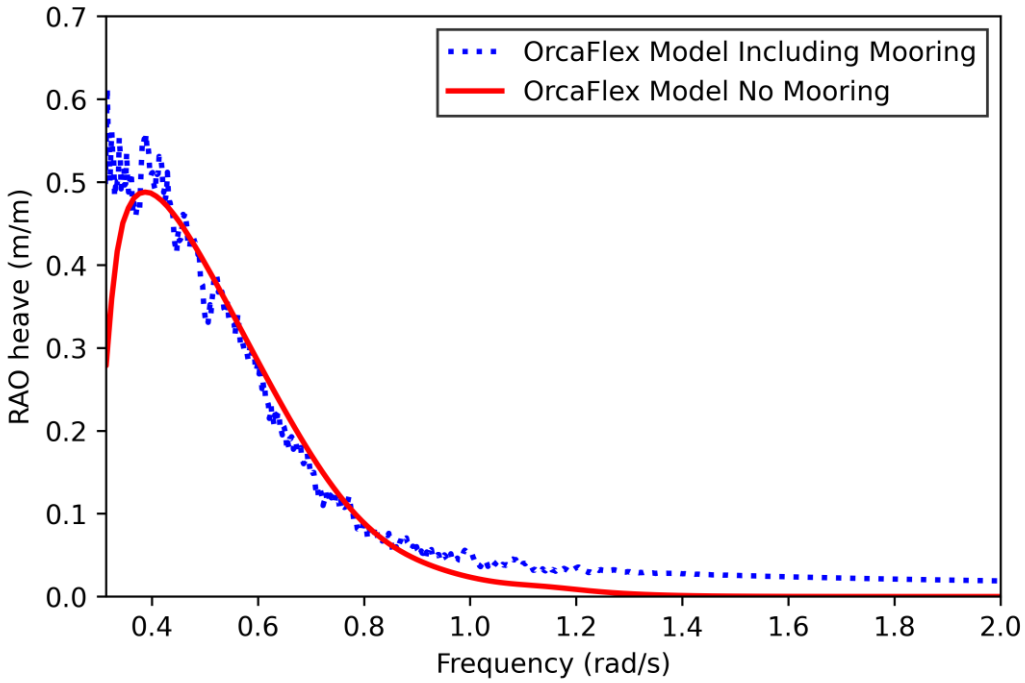

Figure 4-16: Mooring effects on the heave RAO.

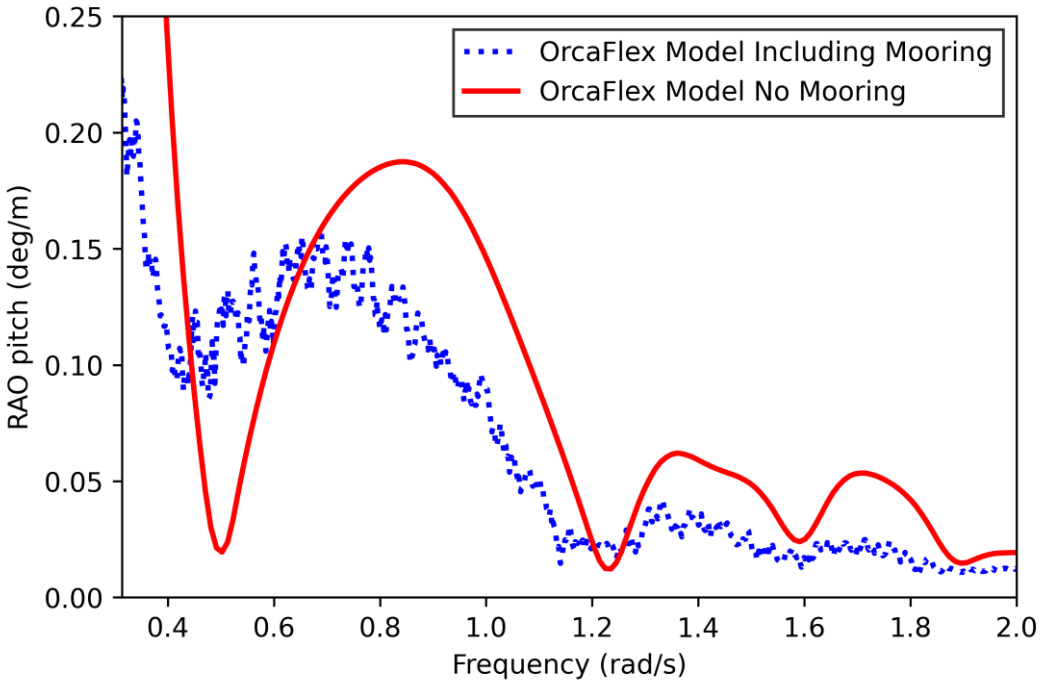

Figure 4-17: Mooring effects on the pitch RAO.

4.3.3 Suspended Power Cable Configuration Study

This section describes the parametric study on different suspended power cable configurations connecting two OC3-Hywind FOWTs. As defined in the case study procedure, an initial steady-state analysis of the system is conducted for both marine growth states. In this part, only Direction 1 is considered, with constant current and wind velocity profiles applied. Out of the 36 cases, only 10 successfully passed this stage of the configuration study. Table 4-13 gives an overview of the reasons for failure. The differences between the two marine growth states appear to be small for the static analysis since all cases that pass the Start of Life (SOL) assessment also pass the End of Life (EOL) assessment. The most common reason for a failure is that the cable is getting too close to the seabed, followed by insufficient surface clearance. No setup failed due to a small bending radius, which can be explained by the relatively high bending stiffness of the power cable. Figure 4-18 shows the vertical excursion of the SOL setup with 9 buoys and a cable length of 1220 m for different spacings. Smaller spacing between the buoys leads to the cable floating at the sea surface, while larger spacing results in cable sections touching the seabed. For all considered cable lengths and numbers of buoys, only the setups with spacings of 90 m and 100 m passed the static analysis. The highest tension along the power cable occurs at one of the hang-off points for nearly all configurations. The fitness factor approach detailed in Section 2.7 is applied to the EOL state investigation results to select the three setups included in the dynamic simulations. The resulting fitness factors are shown in Figure 4-19. The axial tension is a more critical parameter than bending for the cable considered in the present study. An increase in the number of buoys seems to reduce the maximum tension but slightly increases bending. The configurations with 10 buoys and 100 m spacing, as well as the configuration with 9 buoys, 100 m spacing, and a 1220 m cable length, exhibit the best fitness factors. As a result, these configurations are subject to more detailed analysis in the dynamic simulations.

Table 4-13: Static Analysis Results.

Marine Growth State	Total Tested Cases	Successful cases	Causes of Failure			
			MBL	MBR	Surface clearance	Seabed clearance
SOL	36	10	2	0	6	18
EOL	10	10	0	0	0	0

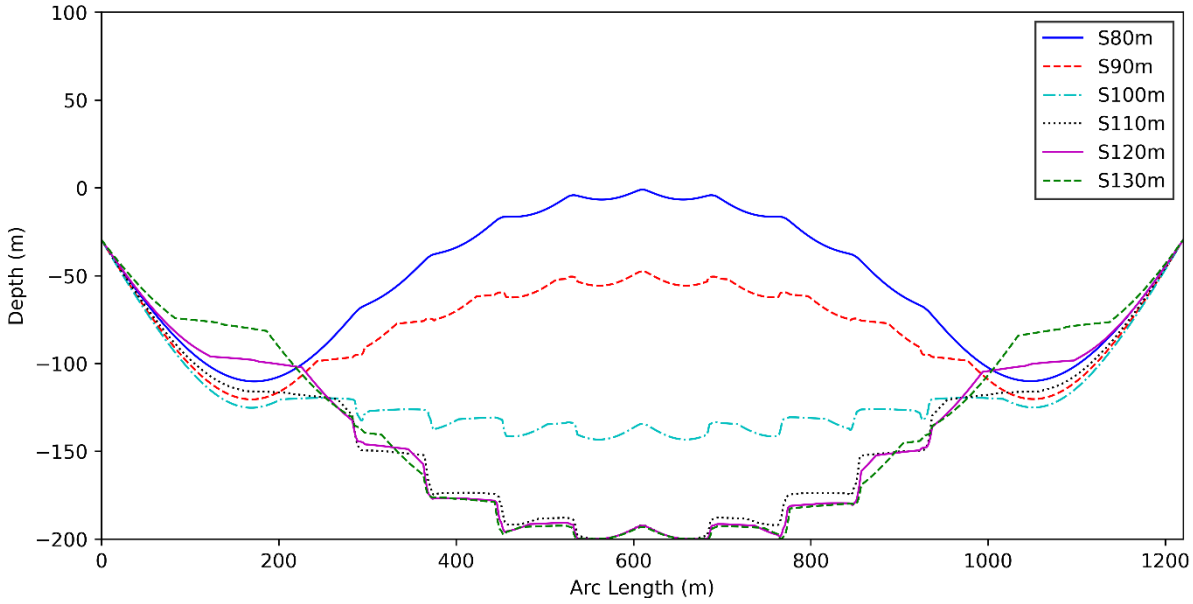

Figure 4-18: Vertical excursions for different buoy spacings.

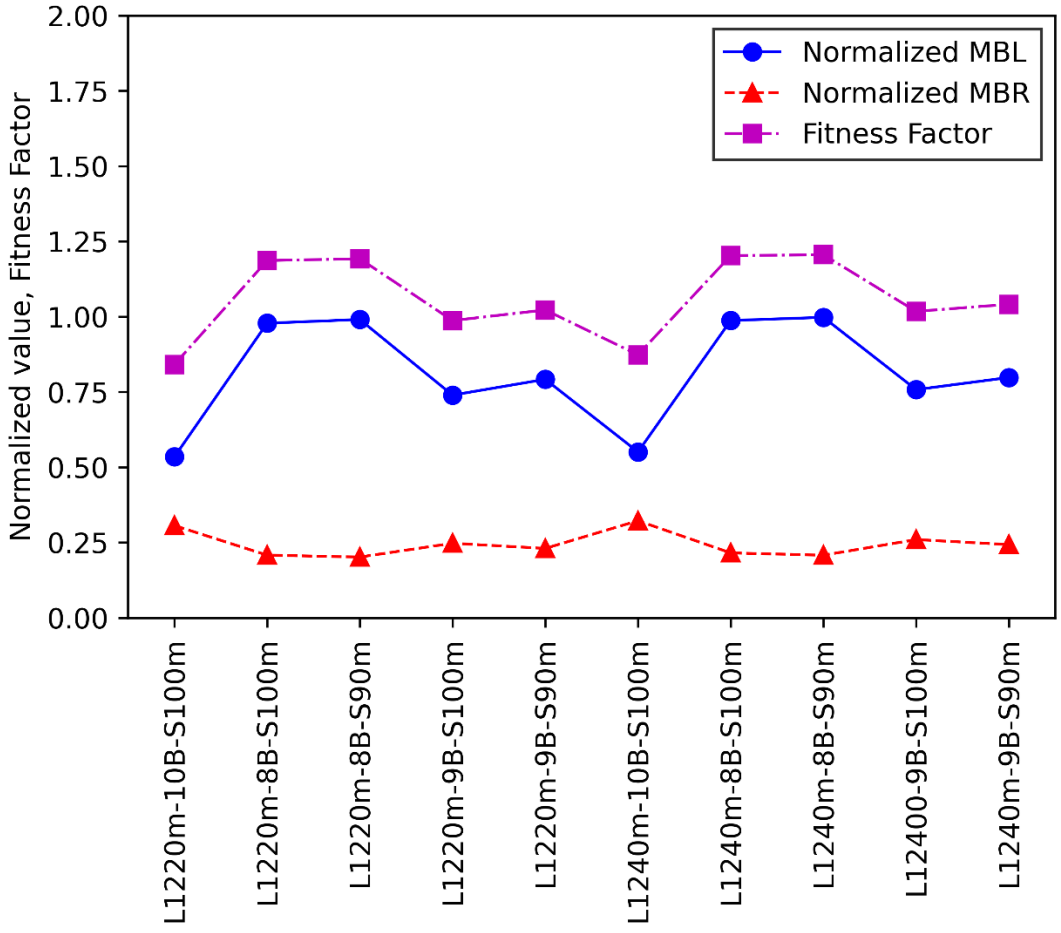

Figure 4-19: Fitness Factors for the static analysis EOL setups.

Table 4-14 shows the maximum effective tensions of the power cable obtained by dynamic analyses with different load directions, environmental conditions, and marine growth states. The configuration with 9 buoys exhibits considerably higher maximum tensions than the other two configurations across all load cases, suggesting that the number of buoys primarily influences the tension. Generally, EC2 and the inline flow (Direction 3) represent the most critical load cases. The same behavior was also observed by Ahmad et al. (2023). The EOL state simulations yield higher maximum tensions than the SOL state simulations for all load cases. The influence of different cable lengths in the 10-buoy configurations on maximum effective tensions is very small. Figure 4-20 shows the maximum effective tensions along the power cable for the L1220m-10B-S100m case in the SOL state. The highest tensions consistently occur at the hang-off points. In the middle section of the power cable, maximum tensions are almost identical for all environmental conditions and load directions.

Table 4-14: Maximum effective tensions obtained from dynamic simulations.

		Maximum Effective Tension (kN)					
Environmental Condition	Load Direction	L1220m-10B-S100m		L1220m-9B-S100m		L1240m-10B-S100m	
		SOL	EOL	SOL	EOL	SOL	EOL
EC1	1	46.8	48.6	66.1	67.1	49.0	50.0
	2	49.4	51.3	68.7	69.7	51.1	52.2
	3	49.2	51.2	68.9	70.0	51.0	52.1
EC2	1	47.7	49.6	67.1	68.1	49.9	51.0
	2	50.6	53.3	70.6	72.2	52.5	54.1
	3	52.9	55.6	73.1	74.6	54.3	55.9

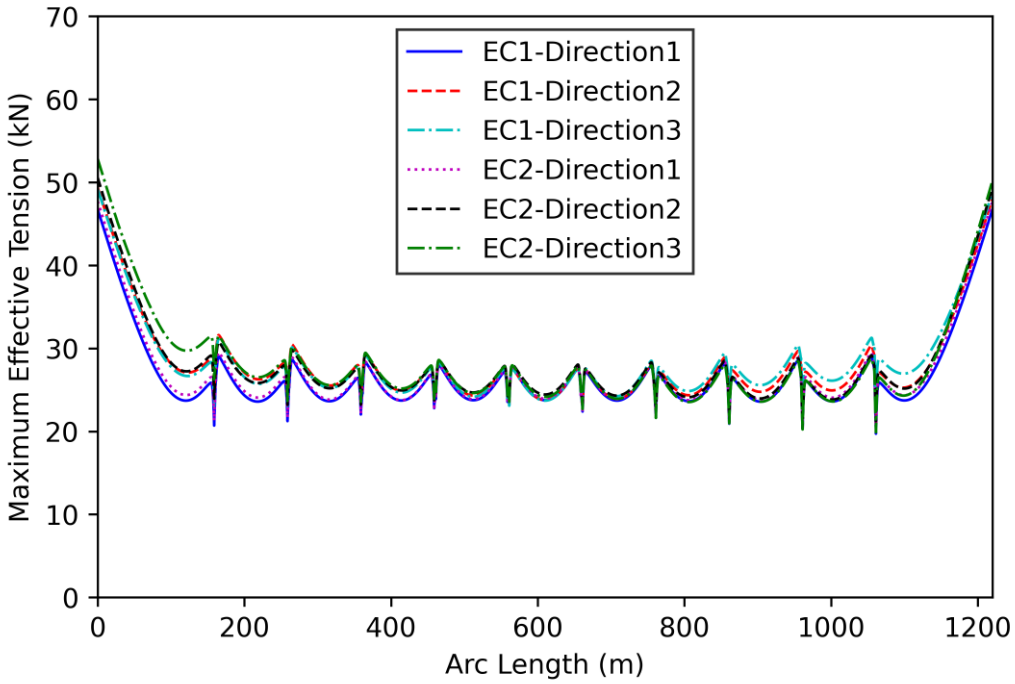

Figure 4-20: Maximum effective tensions along the power cable.

Table 4-15 shows the minimum bending radii of the power cable for the different configurations, load directions, and load parameters. The setup with 9 buoys has higher MBR compared to the setup with 10 buoys, indicating that it is less critical. MBR values are slightly reduced for the EC2 compared to EC1, which is consistent with the findings of Ahmad et al. (2023). Moreover, the MBR for the SOL cases are lower than those for the EOL cases. Shorter power cables have a higher MBR than longer cables. According to Ahmad et al. (2023), this can be attributed to the varying amounts of cable sag.

Table 4-15: Minimum bending radii obtained from dynamic simulations.

		Minimum Bending Radius (m)					
Environmental Condition	Load Direction	L1220m-10B-S100m		L1220m-9B-S100m		L1240m-10B-S100m	
		SOL	EOL	SOL	EOL	SOL	EOL
EC1	1	7.9	8.1	9.9	10.0	7.6	7.7
	2	7.5	7.6	9.6	9.6	7.2	7.2
	3	7.5	7.6	9.5	9.6	7.2	7.2
EC2	1	7.9	8.1	9.8	9.9	7.6	7.6
	2	7.4	7.5	9.4	9.5	7.2	7.2
	3	7.4	7.6	9.3	9.4	7.1	7.2

Figure 4-21 shows the maximum horizontal excursions of the three power cable configurations in the EOL states for Direction 1. An increasing number of buoys leads to a larger horizontal excursion of the power cable, which can be attributed to the increased drag area. Moreover, a longer cable also increases the horizontal excursion. The load case EC2 leads to a significantly higher horizontal excursion than EC1 due to its much larger current and wave loads. However, the FOWT experiences larger drift for EC1 than for EC2, as the turbine blades are pitched to feather at higher wind speeds, resulting in a reduced drag area.

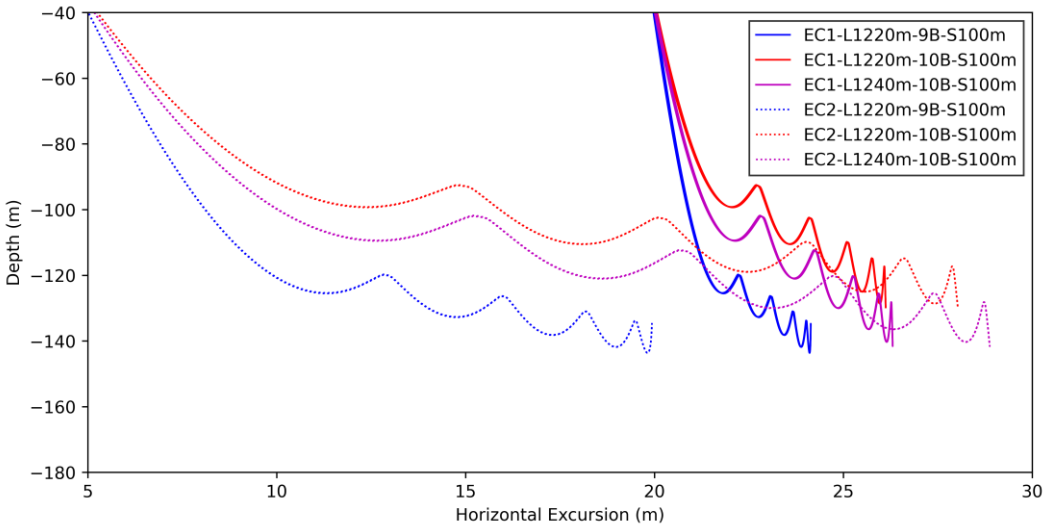

Figure 4-21: Horizontal excursions for different cable configurations.

The most suitable suspended power cable configuration is selected based on the fitness factors obtained for the most critical case. Since the EOL state simulations for Direction 3 and EC2 lead to higher tensions than the other cases, this load combination is selected for further investigations. Table 4-16 lists the obtained fitness factors. The L1220m-9B-S100m configuration has a significantly higher value of normalized MBL, while the other two configurations have approximately 29% lower values. Due to the slightly lower tension and slightly higher MBR in the critical load case, the L1220m-10B-S100m configuration is selected for further analysis.

Table 4-16: Fitness Factors for EOL state simulations of EC2 and Direction 3.

	L1220m-10B-S100m	L1220m-9B-S100m	L1240m-10B-S100m
Normalized MBL	0.62	0.83	0.62
Normalized MBR	0.33	0.27	0.35
Fitness Factor	0.95	1.10	0.97

4.3.4 Suspended Power Cable at the CSC FOWT

In this section the influence of the floater type on the suspended power cable is investigated by comparing the results of the dynamic simulations employing the OC3-Hywind spar and the CSC semi-submersible floater types. Table 4-17 lists the maximum effective tensions for the cable connecting two CSC FOWTs and the deviation compared to the tensions obtained using OC3-Hywind FOWTs. Generally, the differences between the two setups are very small. For Direction 1 the CSC setup has higher maximum tensions for both environmental conditions, while for Direction 3 the tensions are higher for the cable between the spar FOWTs. EC2 appears to have a more significant impact on the semi-submersible floater response, as the maximum effective tensions increase more when compared to the spar-type floater than they do for EC1. The marine growth effect is similar for both FOWT types. Figure 4-22 shows the effective tensions along the cable for both types of FOWTs for EC1 and Direction 1. As for the absolute maximum tension values, the effective tensions along the entire power cable are very similar and follow the same pattern. The highest effective tensions occur for both setups at the hang-off points. These cable behaviors can be observed for all environmental conditions, load directions, and marine growth states.

Table 4-17: Comparison of maximum effective tensions.

Environmental Condition	Load Direction	Maximum Effective Tension (kN)		Deviation to simulations with Spar FOWTs	
		SOL	EOL	SOL	EOL
EC1	1	47.2	49.2	+0.9%	+1.2%
	2	47.8	49.9	-3.2%	-2.7%
	3	47.9	49.9	-2.6%	-2.5%
EC2	1	48.9	51.1	+2.5%	+3.0%
	2	51.8	54.3	+2.4%	+1.9%
	3	52.9	55.4	+0.0%	-0.4%

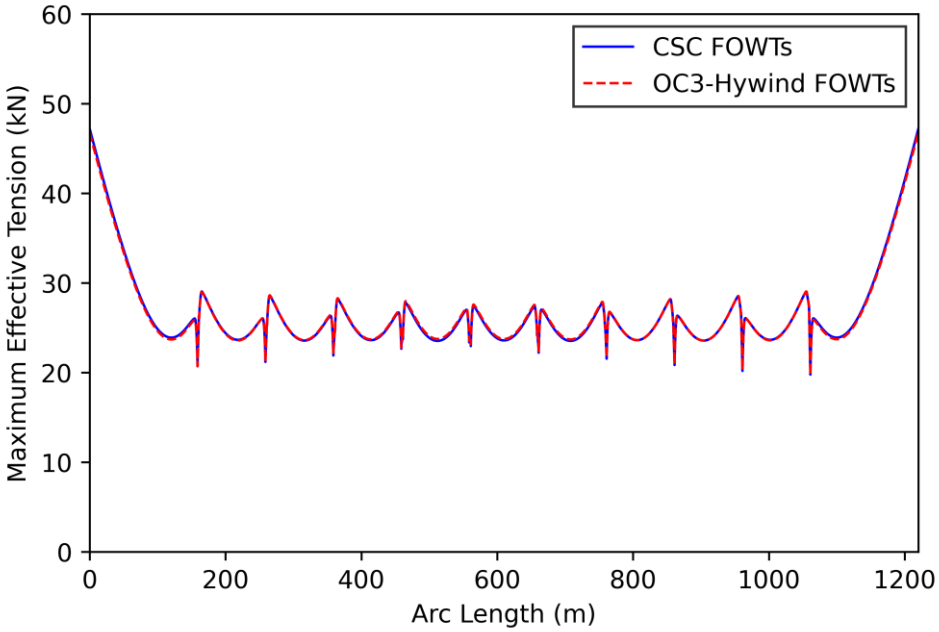

Figure 4-22: Comparison of maximum tensions for SOL state cables, EC1 and Direction 1.

Table 4-18 lists the minimum bending radii for the CSC setups, along with the differences compared to the MBR obtained using spar FOWTs. For EC2, the MBR values are almost identical for all load directions, while for EC1, the cables connecting two CSC FOWTs have larger bending radii for Directions 2 and 3. Consistently with previous observations, marine growth does not yield any differences between the two setups. Figure 4-23 shows the bending radii along the cable for both types of FOWTs for EC1 and Direction 1. The bending radii for both setups are very similar along the entire cable length. Under all investigated conditions, the cable MBR for setups using CSC FOWTs and spar FOWTs are almost the same.

Table 4-18: Comparison of minimum bending radii.

Environmental Condition	Load Direction	Minimum Bending Radius (m)		Deviation to simulations with Spar FOWTs	
		SOL	EOL	SOL	EOL
EC1	1	7.9	8.0	+0.0%	-1.2%
	2	7.9	8.0	+5.3%	+5.3%
	3	7.8	8.0	+4.0%	+5.3%
EC2	1	7.8	7.9	-1.3%	-2.5%
	2	7.4	7.5	+0.0%	+0.0%
	3	7.4	7.5	+0.0%	-1.3%

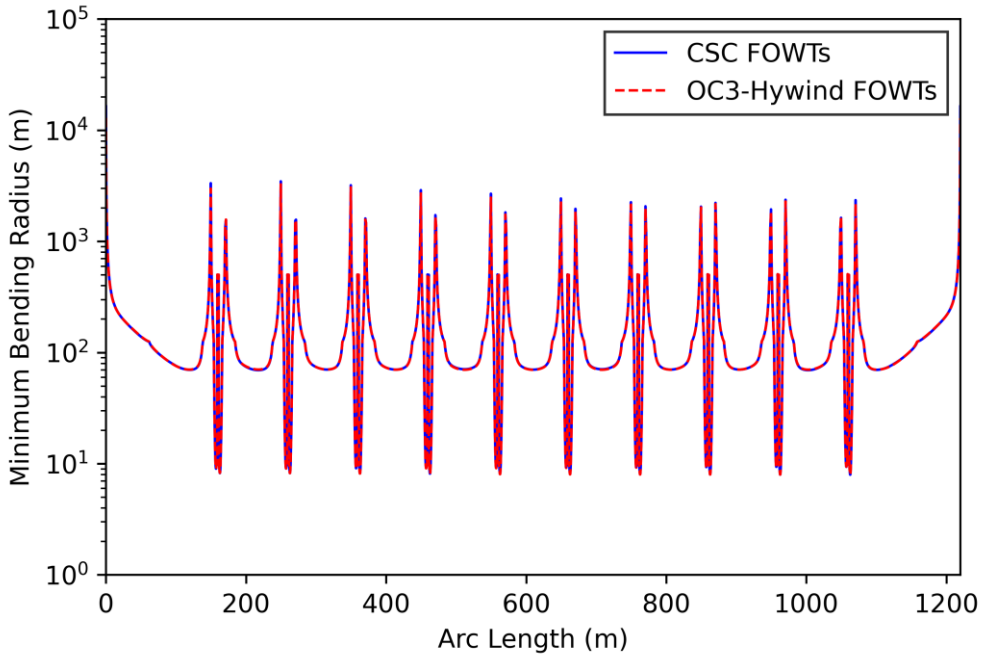

Figure 4-23: Comparison of MBR for SOL state cables, EC1 and Direction 1.

4.3.5 Power Cable Behavior in a Wind Farm

Floating wind farms consisting of three and four OC3-Hywind FOWTs are modeled to investigate the effect of multiple turbines on the effective tension of connecting power cables. Figure 4-24 shows the effective tensions of power cables with the same load angle in both the three-turbine and two-turbine wind farm layouts for EC1. The differences between the two investigated layouts are very small. Moreover, the differences in cable curvature and horizontal excursion between these setups are also negligible. Figure 4-25 shows the maximum tensions of the power cables in the rectangular wind farm layout. The results for power cables 1 and 3, which face the same load angle, are nearly identical, while the results for power cable 2 differ due to varying angles relative to the environmental loads direction. Based on the obtained results, the array effects of the turbines do not impact the suspended power cables, and a two-turbine layout with different load angles can be considered representative of entire wind farms as it provides conservative estimates of maximum effective tensions in the power cable. Based on the aforementioned results for the OC3-Hywind FOWT farm, it can be foreseen that similar results and conclusions will be attained for the cases of CSC FOWTs at wind farm level.

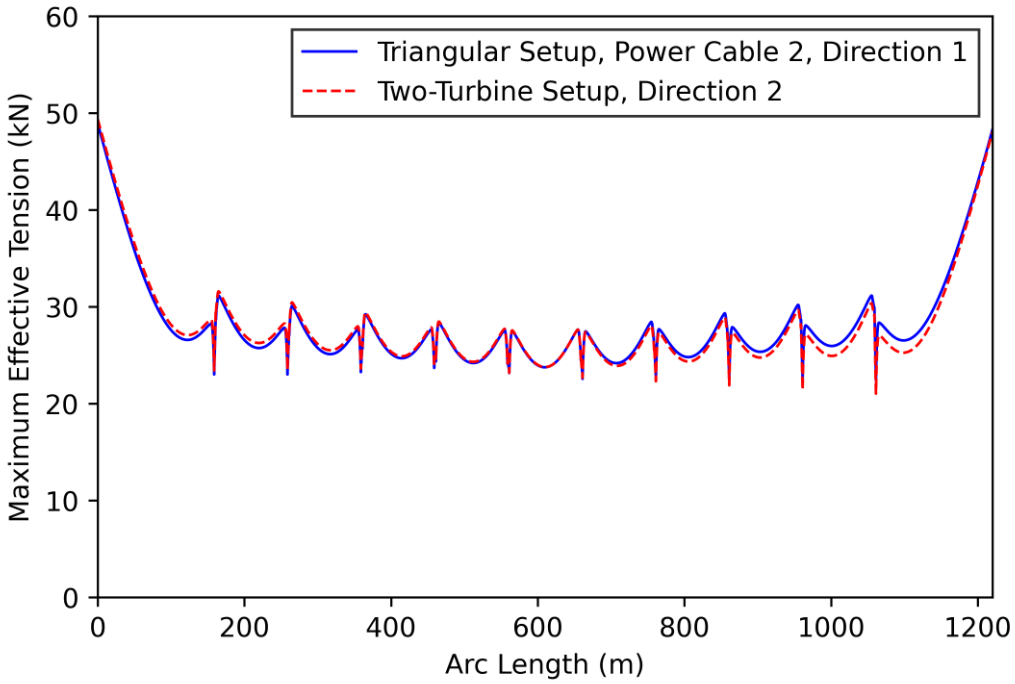

Figure 4-24: Maximum tensions of power cables under the same load angle for different windfarm layouts during EC1.

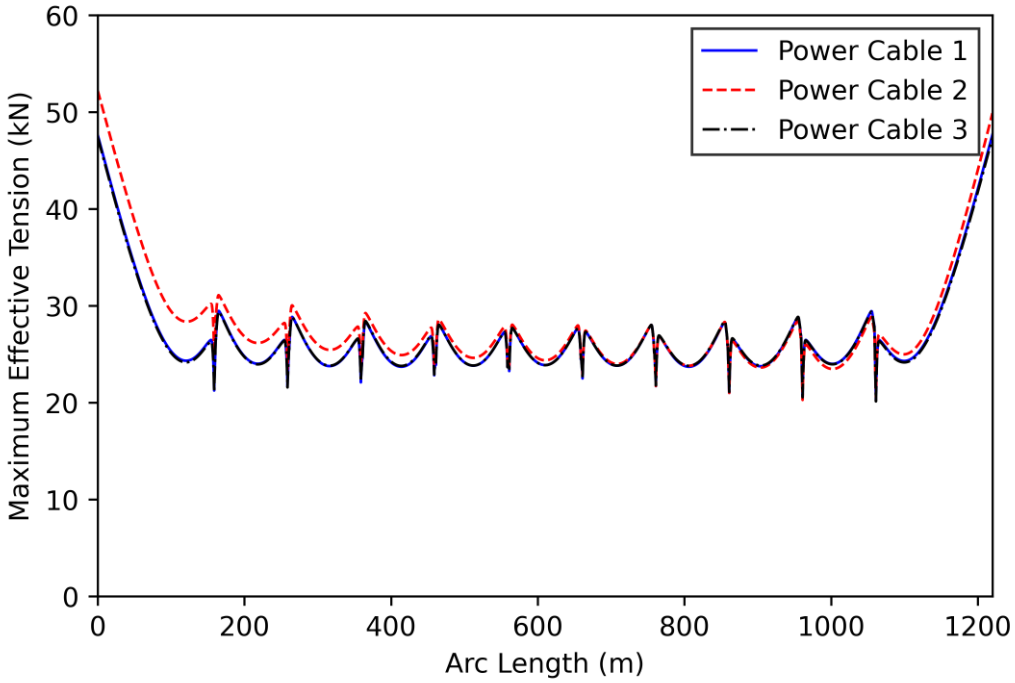

Figure 4-25: Maximum effective tensions of the power cables in the rectangular layout during load conditions EC2 and Direction 1.

4.4 Conclusion

Global responses of two different types of FOWTs are modelled. Several suspended inter-array power cable configurations with varying numbers of buoys, cable lengths and buoy spacings are defined. The marine growth effects on the power cables are included in the analyses. Static and dynamic analyses of multiple combinations of environmental loads and power cable configurations are performed to determine the most suitable configuration based on maximum effective tension, minimum bending radius as well as vertical and horizontal excursions. The influence of the selected FOWT type on the suspended inter-array power cable is investigated. Wind farms consisting of three and four turbines are modelled to analyze possible effects of multi-turbine layouts on the power cables. The main conclusions obtained by this study are summarized below:

- In terms of the best suspended power cable configuration between two spar FOWTs, an increasing number of buoys seems to reduce the effective tension in the cable. Cable length has only a very small impact on tension and curvature, and the MBR is less critical for this power cable than tension. The buoy spacing determines whether the cable touches the seabed, floats fully submerged, or floats on the sea surface. A spacing of 100 m yields the best results for the considered setup.
- The most critical environmental load is EC2, where the larger current load and floater motions directly affect the power cable. Direction 3 (inline flow) results in the largest tensions and the smallest bending radii.
- The differences between the cables in the SOL and EOL states are small, with EOL states leading to slightly larger maximum tensions, while SOL states show smaller minimum bending radii.
- Concerning the application of the power cable between different types of floaters, the differences in the cable tensions and curvature are negligible when comparing the OC3-Hywind FOWT with the CSC FOWT. Between these two setups, the results differ slightly close to the hang-off points, while the cable behavior in the remaining part is nearly identical. Therefore, a cable proven suitable for one type of floater can likely be used for another FOWT floater type.
- In terms of the application of suspended power cables in entire offshore wind farms, the behaviors of a cable in a multiple FOWT wind farm layout and an analogous cable

in a two FOWT layout are nearly identical under the same loading condition and the same load direction. Furthermore, parallel cables connecting FOWTs in a wind farm show the same motion responses, so array effects are negligible for the suspended power cable design. Performing simulations of the setup between two FOWTs for different loading directions and conditions is considered representative of entire wind farms as it provides conservative estimates of maximum effective tensions in the power cable.

Acknowledgments

The authors acknowledge The Research Council of Norway and the industry partners of ImpactWind SouthWest – RCN project number 332034 – for their support. The authors would like to thank Izwan Bin Ahmad from IKM Ocean Design for his technical assistance.

Chapter 5 - Fatigue Assessment of Suspended Inter-Array Power Cables for Floating Offshore Wind Turbines

Dennis Beier [a], Marek Jan Janocha [a], Naiquan Ye [b], Muk Chen Ong [a]

[a] Department of Mechanical and Structural Engineering and Materials Science, University of Stavanger, Stavanger, Norway

[b] SINTEF Ocean, Trondheim, Norway

This content is under review in Engineering Structures as:

Beier, D., Janocha, M. J., & Ye, N., Ong, M. C. (2023). Fatigue Assessment of Suspended Inter-Array Power Cables for Floating Offshore Wind Turbines.

Abstract

The present paper aims to investigate the fatigue behavior of suspended inter-array power cables connecting two floating offshore wind turbines (FOWTs). Two spar FOWTs interconnected with a dynamic power cable are chosen as the base configuration for the present investigation. The base configuration is modeled in the dynamic analysis software OrcaFlex. The relationship between the axial tensions and curvatures of the power cable and its stresses is obtained by cross-section analysis in UFLEX (special purpose Finite Element program for nonlinear stress analysis of complex umbilical and cable cross-sections). Several different environmental conditions and load directions are applied. A fatigue life of 85 years is determined for the base configuration, with curvature-induced stresses being identified as the main contributor to the fatigue damage. Effects of marine growth on the fatigue life of the power cable are investigated. It is observed that marine growth negatively affects the fatigue life of the power cable. A parametric study on the effect of the number of buoys attached to the cable on the fatigue life is performed. Decreasing the number of buoys below the optimal value leads to an increase in fatigue life due to lower curvatures. In addition to the base configuration, an alternative configuration using semi-submersible floaters is investigated under the same metocean conditions and cable geometry. The power cable fatigue life is higher for semi-submersible floaters compared to the spar floaters. The present findings reveal that the main reason is the reduced number of large amplitude curvature cycles. The critical component prone to fatigue failure for all evaluated cases is the armor layer, and the largest fatigue damage always occurs at buoy-cable connection points. The critical direction of environmental load resulting in the highest fatigue damage is found to be the load case where waves, wind and current approach the suspended cable in a crossflow direction.

Keywords: Suspended power cable, inter-array cable configuration, floating offshore wind turbine, OC3 Hywind, CSC FOWT, fatigue analysis

5.1 Introduction

Offshore wind farms are developed to capture the extensive renewable energy resources available in the wind above the oceans. Recently, FOWTs have been designed to enable energy production in areas with deeper water. The first commercial FOWTs are already installed in the wind farms Hywind Scotland (Eldøy, 2017), Kincardine (Principle Power Inc., 2023), and Hywind Tampen (Equinor ASA, 2019). In all these projects, the inter-array power cables are laid on the seabed. However, as a possible improvement measure for FOWT farms, a submerged installation of the power cables without seabed contact has been proposed (Rapha & Domínguez, 2021). This suspended installation shortens the power cable's length, lowering investment costs and reducing inter-array energy loss (Ahmad et al., 2023).

Several studies have been performed to find the optimal suspended power cable configuration between two FOWTs taking into account cable tensions and curvatures (Ahmad et al., 2023; Beier et al., 2023a; Shi et al., 2022). Schnepf et al. (2023) examined several suspended power cable designs between two FOWTs. They found that compared to cables with buoyancy modules, cables with buoys experience much lower effective tensions. Shi et al. (2022) investigated the performance of short dynamic power cables linking two FOWTs under harsh environmental conditions. The power cables were equipped with buoyancy modules. They determined that the key factor affecting the curvature and stress of the power cable was the buoyancy module arrangement. Schnepf et al. (2022) evaluated the behavior of suspended power cables coupling a FOWT with floating production storage and offloading unit (FPSO). By comparing a power cable configuration that was hanging freely and a power cable configuration with buoys attached to its middle part, their investigation revealed that buoys equally spaced along the power cable can reduce its axial tensions. A design methodology for suspended inter-array power cable arrangements between two FOWTs was developed by Ahmad et al. (2023). They proposed a solution to lower the maximum tensions in the power cable by attaching numerous buoys along the cable span. Furthermore, copper conductors were found to be superior to aluminum conductors for dynamic offshore power cables used in suspended configurations. Beier et al. (2023b) investigated the application of a suspended power cable in offshore wind farms with spar and semi-submersible FOWTs. They found that the influence of the floater type on the power cable tensions and curvatures is negligible and

that analyzing two-turbine setups with different environmental load directions is representative also for multi-turbine wind farm layouts.

Marta et al. (2015) investigated dynamic power cables installed at multiple floating offshore renewable energy projects. They reported that fatigue was the main failure mode in all of their simulations. They found that fretting leading to cracks in copper conductors is a significant contributor to the fatigue damage. Nasution et al. (2012) obtained a stress-cycle (S-N) curve for a copper conductor of a dynamic offshore power cable through finite element simulations and experiments. The impacts of bending and tension loads on copper conductors were analyzed by Nasution et al. (2014), who identified the inter-layer friction effects resulting from bending as the main cause of fatigue damage of conductors used in dynamic power cables. Thies et al. (2012) studied the fatigue life and effective tensions of dynamic power cables in lazy-wave and catenary configurations attached to a wave energy converter. The lazy-wave configuration was found to have a lower maximum tension and fewer fatigue cycles than the catenary configuration. When lowering the maximum effective tension, a significant increase in the fatigue life of the dynamic power cable was observed in their study. The fatigue life of a dynamic power cable connecting a FOWT to the transition joint was calculated by Bakken (2019). The lowest fatigue life of the copper conductor in the power cable was observed at the location of the largest tension range. Local friction was identified as the main factor contributing to fatigue damage. Hu et al. (2022) investigated the bending behavior of a dynamic offshore power cable with a copper conductor. They concluded that the nonlinear bending of the power cable is the main contributor to fatigue damage. Svensson (2020) used simulations and experiments to establish prediction models for the fatigue life of dynamic power cables. Interlayer friction forces were identified as the main parameter influencing the fatigue life. Zhao et al. (2021) analyzed the behavior and fatigue of power cables connected to a FOWT in lazy-wave and double-wave configurations in shallow water. They discovered that the hang-off point was the most important location in terms of the tension and fatigue of the power cable for both configurations. The lower buoyancy section of the double-wave setup was identified as another critical point regarding fatigue damage. Ballard et al. (2022) assessed the fatigue life of a lazy-wave dynamic power cable connecting a wave energy converter to the seabed. Cyclic curvature variation of the cable was identified as the critical fatigue cause in their setup. The fatigue life of an exemplary suspended power cable installed

between two spar FOWTs has been evaluated by Beier et al. (2023a). They determined a very long fatigue life for their setup and identified cable curvature as the main contributor to fatigue damage.

To the best of authors' knowledge, no prior research has been performed to determine the influence of different parameters, such as marine growth, cable configuration, and floater type, on the fatigue behavior of suspended inter-array power cables connecting two FOWTs. This study aims to fill this gap by evaluating the fatigue life of a realistic suspended power cable for different setups.

This work is organized as follows. The setup of the FOWTs, the applied environmental conditions, the dynamic offshore power cable properties and configurations, and the fatigue assessment procedure are described in Section 2. Section 3 presents and discusses the results of the fatigue analyses. In Section 4, conclusions of the present study are drawn.

5.2 Methodology and Numerical Setup

This chapter describes the numerical setup of the two different FOWTs, the applied environmental conditions, the suspended power cable configurations, properties, and the fatigue assessment procedure. The numerical software OrcaFlex version 11.2d (Orcina Ltd, 2022) is used for the dynamic analysis of the setup, and the numerical software UFLEX (SINTEF, 2018) is used to determine the power cable cross-sectional properties.

5.2.1 OC3-Hywind FOWT

The 5 MW OC3-Hywind FOWT is used in the present study as a representative spar FOWT. Jonkman (2010) and Jonkman et al. (2009) provided detailed characteristics of this FOWT. The general parameters of the OC3-Hywind FOWT are listed in Table 4-1, and Figure 4-1 depicts its geometry. The water depth is reduced from the 320 m specified by Jonkman (2010) to 200 m to facilitate direct comparison with the semi-submersible CSC FOWT. Table 4-2 lists the standard mooring line characteristics optimized for the shallower water depth of 200 m.

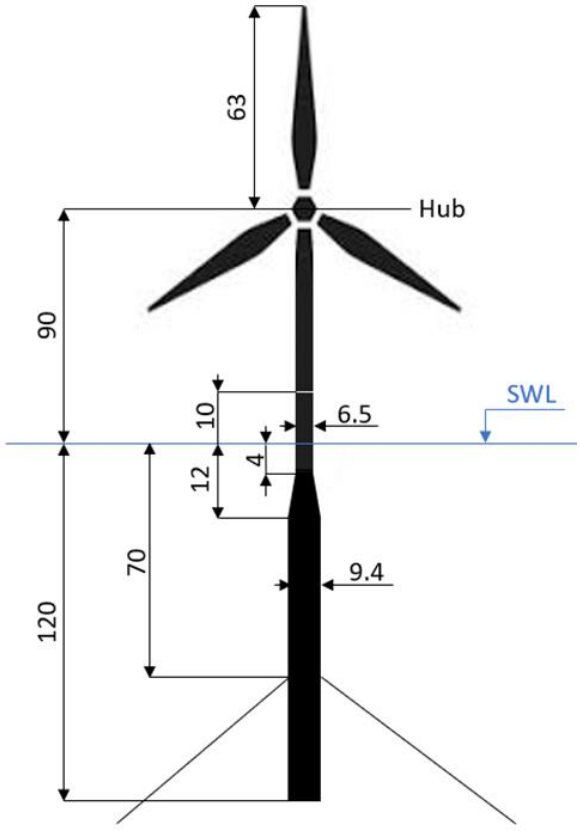

Figure 5-1: OC3-Hywind FOWT geometry. Dimensions in m.

Table 5-1: OC3-Hywind FOWT specifications (based on Jonkman et al. (2009) and Jonkman (2010)).

Rotor orientation, configuration	-	Upwind, 3 blades
Rotor diameter	m	126
Hub diameter	m	3
Hub height	m	90
Cut-in, rated, cut-out wind speed	m/s	3, 11.4, 25
Platform diameter	m	6.5 to 9.4 (tapered)
Rotor mass	kg	110000
Nacelle mass	kg	240000
Tower mass	kg	249718
Platform mass, including ballast	kg	7466330
Spar COG[1] below SWL[2] along platform centerline	m	89.9155
Platform total draft	m	120
Water depth	m	200

[1] COG = Center of gravity, [2] SWL = Still water level

Table 5-2: OC3-Hywind FOWT mooring line properties.

Number of mooring lines	-	3
Angle between mooring lines	°	120
Mass per unit length	kg/m	152.9
Mooring line length	m	502.2
Depth to fairleads below SWL	m	70.0
Radius to fairleads from platform centerline	m	5.2
Radius to anchors from platform centerline	m	473.8
Mooring line diameter	m	0.09
Mooring Line Extensional Stiffness	N	384243000
Additional Yaw Spring Stiffness	Nm/rad	98340000

5.2.2 CSC FOWT

In the present study, the 5 MW CSC braceless steel FOWT (Luan et al., 2016) is selected as a representative semi-submersible FOWT. The hull comprises a central column, three lateral columns, and three pontoons. The CSC FOWT's geometry is shown in Figure 4-2, and its general features are listed in Table 4-3. The same 5 MW NREL wind turbine used in the OC3-Hywind FOWT is mounted on the CSC floater. Table 4-4 lists the mooring line characteristics for the CSC FOWT.

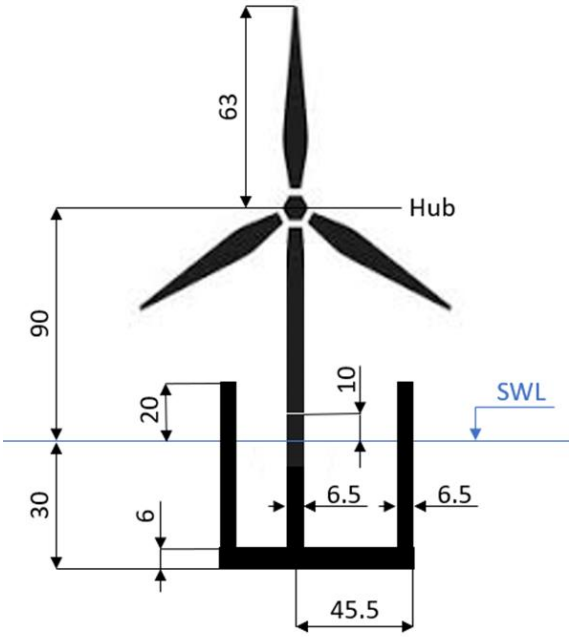

Figure 5-2: CSC FOWT geometry, dimensions in m.

Table 5-3: CSC FOWT specifications (based on Luan et al. (2016) and Jonkman et al. (2009)).

Rotor orientation, configuration	-	Upwind, 3 blades
Rotor diameter	m	126
Hub diameter	m	3
Hub height	m	90
Cut-in, rated, cut-out wind speed	m/s	3, 11.4, 25
Column diameter	m	6.5
Pontoon height	m	6
Pontoon width	m	9
Rotor mass	kg	110000
Nacelle mass	kg	240000
Tower mass	kg	249718
Platform mass, including ballast	kg	9738000
Platform COG below SWL along centerline	m	24.36
Platform total draft	m	30
Water depth	m	200

Table 5-4: CSC FOWT mooring line properties (based on Luan et al. (2016)).

Number of mooring lines	-	3
Angle between mooring lines	°	120
Mass per unit length	kg/m	115
Mooring line length	m	1073
Depth to fairleads below SWL	m	18
Radius to fairleads from platform centerline	m	44.3
Radius to anchors from platform centerline	m	1084.4
Mooring line diameter	m	0.137
Clump weight in water	kg	15000
Distance from the attachment point of the clump weight to the fairlead (along the mooring line)	m	240

5.2.3 Environmental Conditions

The environmental conditions applied in this study are representative of a typical location in the North Sea. Table 4-5 lists the wave, wind, and current data for the six load cases included in the present work. The environmental case (EC) 6 is an extreme weather case where the wind turbine is in a parked position. Three different load directions are considered, as shown in Figure 5-3. In all load cases, waves, wind, and current have the same direction. The JONSWAP spectrum is applied to model irregular waves, and the NPD spectrum is used to simulate wind conditions (Norwegian Petroleum Directorate (NPD), 1995). The tidal current velocity at the still water level $v_{c,tide}$ is based on NORSOK (Standards Norway, 2007), while the wind generated current at the still water level $v_{c,wind}$ is estimated based on the reference wind speed (DNV, 2010):

$$v_{c,wind}(0) = 0.03 * U_{1\ hour,10m} \tag{5-1}$$

where $U_{1\ hour,10m}$ is the 1-hour mean wind speed at a height 10 m above the sea level.

The overall current profile is determined through the following formula given by DNV (2010):

$$v_c(z) = v_{c,tide}(0)\left(\frac{d+z}{d}\right)^{\frac{1}{7}} + v_{c,wind}(0)\left(\frac{d_0+z}{d_0}\right) \tag{5-2}$$

where z is a specific height above the seabed, d is the water depth and d_0 is the reference depth for wind generated current. This reference depth is specified as 50 m. The wind generated current is assumed to be negligible below this depth.

Table 5-5: Environmental data.

Load case	Wave H_s (m)	Wave T_p (s)	Tidal current at SWL (m/s)	Windspeed at hub height (m/s)
EC1	2.10	9.74	0.1	5
EC2	2.88	9.98	0.1	10
EC3	3.62	10.29	0.15	14
EC4	4.44	10.66	0.15	18
EC5	5.32	11.06	0.2	22
EC6	6.02	11.38	0.2	26

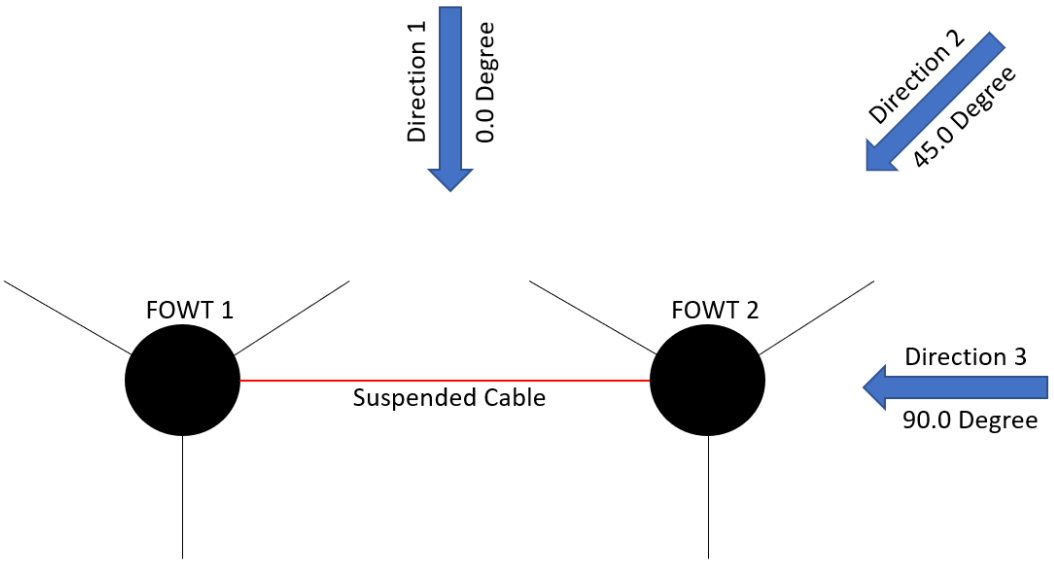

Figure 5-3: Directions of the loads towards the inter-array power cable.

5.2.4 Power Cable Properties

In the present study, the power cable characteristics are taken from Ye and Yuan (2020). The power cable has 9 copper conductors, 19 copper wires per conductor, and a total copper cross-section of 1053 mm^2. Two layers of armor steel wires with a diameter of 5 mm stabilize the cable. Table 4-6 lists the power cable properties. The cross-section of the power cable is shown in Figure 5-4. The cable's nonlinear bending behavior obtained through FE-simulations in UFLEX is represented by the bending moment vs. capacity curve shown in Figure 5-5.

Table 5-6: Power cable properties.

Core main material	–	Copper
Voltage rating	kV	6-10
Outer diameter	m	0.158
Mass per unit length	kg/m	54.0
Torsional stiffness	kNm^2	375
Axial stiffness	MN	750
Drag coefficient	–	1.2
Added mass coefficient	–	1.0

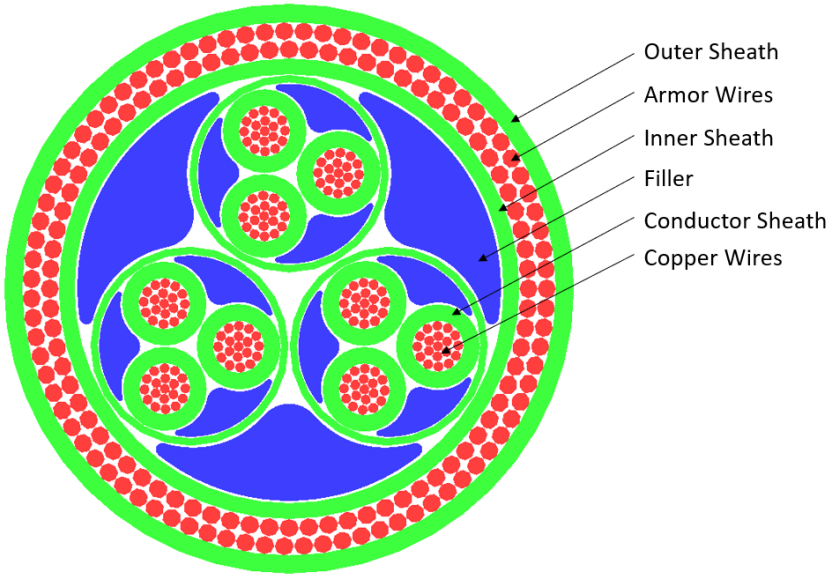

Figure 5-4: Power cable cross section.

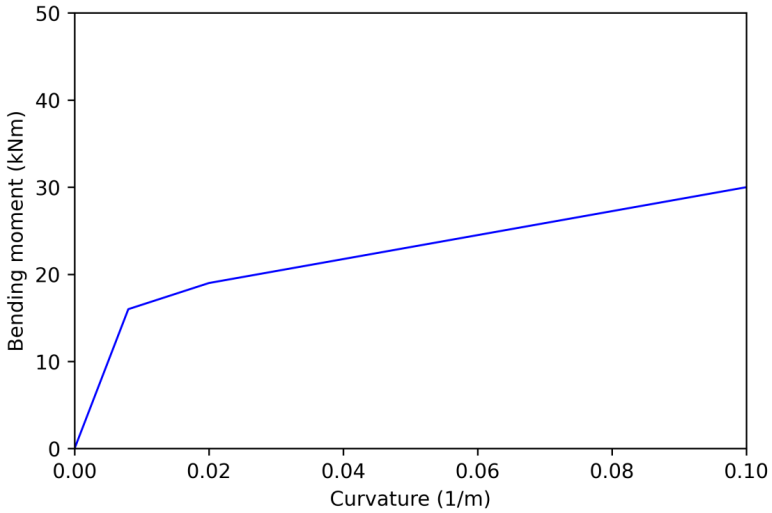

Figure 5-5: Nonlinear bending behavior of the power cable.

Figure 5-6 shows the S-N curves of the power cable components utilized in this study. The S-N curve for the copper wires is based on Nasution et al. (2014), and the S-N curve for the armor wires is based on the information provided by DNV (2014).

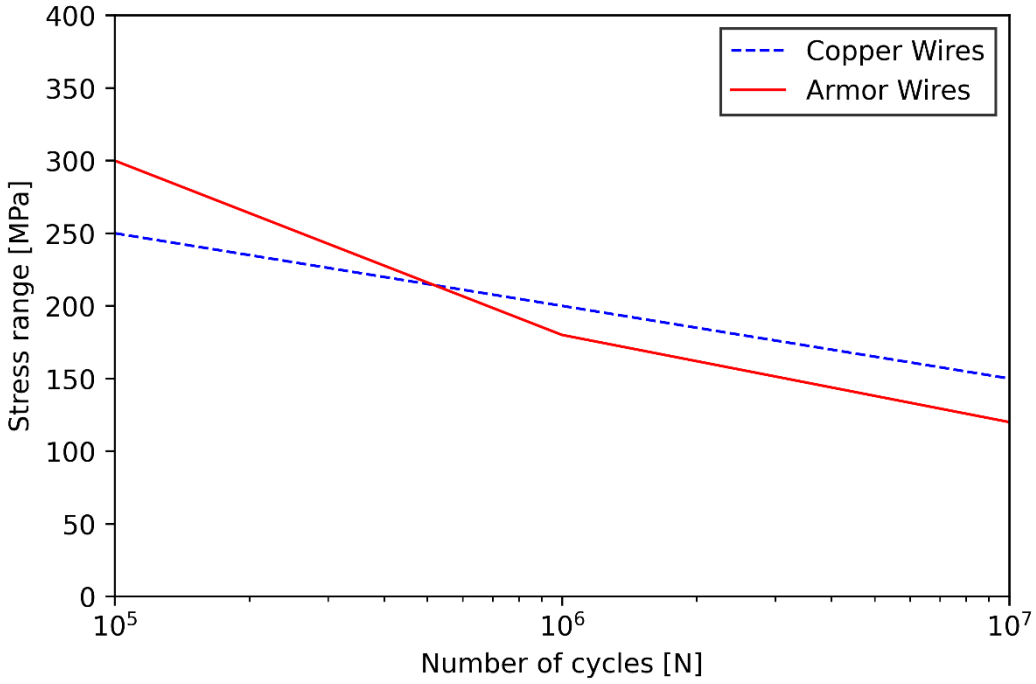

Figure 5-6: S-N curves for the copper and armor wires in the power cable.

The diameter and weight of the power cable change throughout its lifetime due to marine growth. Marine growth parameters are water depth dependent. The information provided by NORSOK (Standards Norway, 2007) and DNV (2010) is used to determine the marine growth effects in this study. The power cable properties in its Start-of-Life (SOL) state and End-of-Life (EOL) state are listed in Table 4-7.

Table 5-7: Power cable properties with marine growth.

Marine growth state	Water depth (m)	Outer diameter (m)	Mass per unit length (kg/m)
SOL	Below -100	0.158	54.0
EOL1	-100 to -60	0.198	66.3
EOL2	-60 to -40	0.218	73.5
EOL3	-40 to -30	0.258	89.9

5.2.5 Suspended Inter-Array Power Cable Setup

The inter-array power cable that connects the two FOWTs is suspended, which means that the cable touches neither the seafloor nor the sea surface. Figure 5-7 shows an example of a suspended power cable configuration. The base configuration in the present study has a cable length of 1220 m and 10 buoys attached to the cable. Beier et al. (2023a) identified this configuration as the most suitable in terms of cable tension and curvature. The properties of the buoys are described in Table 4-8. Each buoy has bend stiffeners attached to both ends to reduce excessive cable bending. The bend stiffeners and buoys are equipped with an anti-marine growth coating. The buoys are equally distributed with a spacing of 100 m. The alternative setup has 9 buoys and the same cable length and spacing as the base configuration. The two power cable configurations were selected based on extensive screening study by Beier et al. (2023a) who employed optimization method in the parameter space of minimum breaking load, minimum bending radius, seabed and surface clearances. The power cable model is discretized into elements in the dynamic analysis software. The size of the elements depends on the location along the cable. The free-hanging cable sections are discretized using a 1.0 m element length, and a segment of 10 m from the hang-off point has an element length of 0.1 m. The cable is separated into elements with sizes of 0.12 m at the bend stiffeners and 0.31 m at the subsea buoy connections. The hang-off point of the power cable is placed 30 m below the still water level (SWL) and on a radius of 5.2 m from the column center axis. In the present simulations, the wind turbines are always facing the incoming wind direction.

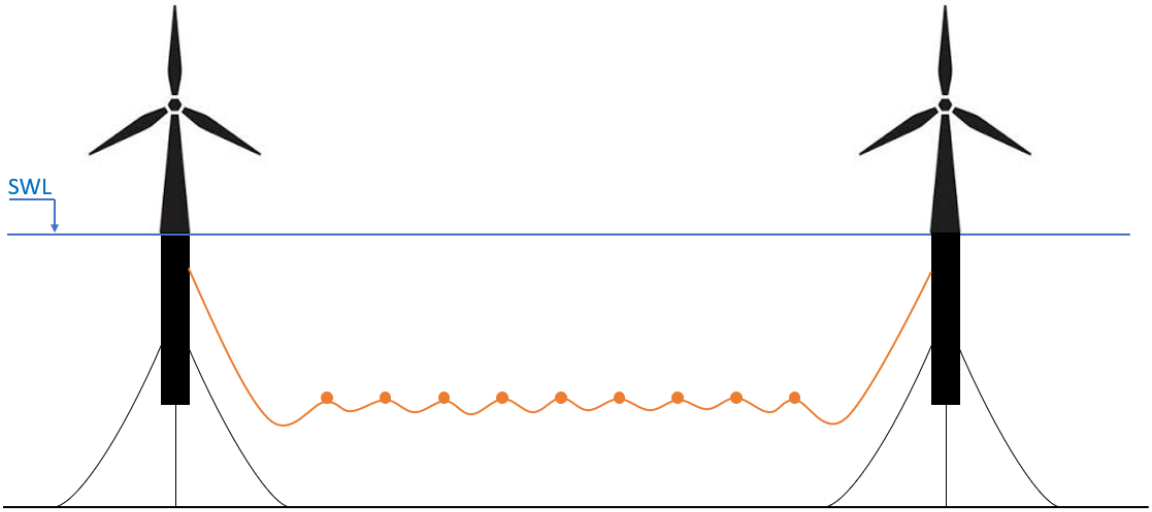

Figure 5-7: Concept of two FOWTs with a suspended power cable.

Table 5-8: Properties of the buoys (Ahmad et al. (2023)).

Length	m	2.170
Volume	m^3	8.615
Mass	kg	2700
Equivalent buoy outer diameter (cylinder shape)	m	2.248
Drag coefficient (normal)	–	0.209
Drag coefficient (axial)	–	1.000
Added mass coefficient (normal)	–	0.459
Added mass coefficient (axial)	–	0.600

5.2.6 Fatigue Assessment Procedure

The fatigue assessment is carried out in several steps. First, dynamic analyses of all load cases are performed in OrcaFlex. The simulations have one hour duration for each load case and a time step of 0.1 s. Random seeds are used to create independent irregular wave and wind conditions. Next, the relationships between the curvature and axial tension of the power cable and its stresses are obtained using UFLEX. Several cases, including the typical curvature and tension values, are computed. Based on these relationships, the time histories of the cable stresses are determined. The Rainflow counting method (ASTM, 2011) is applied to determine the stress cycles. In this method, several stress ranges are defined to group the stress reversal points. Four reversal points are considered to find the stress cycles. If the outer points bind

the inner points, a cycle is counted, and the difference between the stress ranges of the inner points is used as the cycle's amplitude. This method assumes that the fatigue damage caused by one cycle in a constant amplitude test is comparable to the fatigue damage caused by a closed cycle in an irregular amplitude loading. Because there are so few half-cycles in every practical scenario, this procedure ignores the damage caused by them. The accumulated damage is calculated according to the Miner-Palmgren rule (Kauzlarich, 1989). In this theory, constant damage during a given stress range is assumed. The Miner-Palmgren rule is given by:

$$D = \sum_{i=1}^{k} \frac{n_i}{N_i} \tag{5-3}$$

where *D* comprises the accumulated damage, *i* is an individual stress range, *k* is the total number of stress ranges, *n* is the number of cycles counted in an individual stress range, and *N* is the number of cycles until damage occurs in a specific stress range. This amount of cycles *N* can be obtained from the S-N curves for the different power cable components. Based on this procedure, the fatigue damage and the fatigue life of the dynamic power cable is determined.

Four different setups are included in the present study. One setup with 10 buoys in the SOL state, one setup with 10 buoys in the EOL state and one setup with 9 buoys in the SOL state all connecting two OC3-Hywind FOWTs. Also, one setup with 10 buoys in the SOL state connecting two CSC FOWTs is considered. For all these setups, the fatigue analysis procedure is repeated in exactly the same way. All environmental load cases are assumed to have the same occurrence probability.

5.3 Results and discussion

This section presents the results of the curvature-stress relationship and tension-stress relationship investigations as well as the outcomes of the fatigue analyses for the different numerical setups.

5.3.1 Curvature-Stress and Tension-Stress Relationships

The relationships between the cable curvatures and effective tensions to the corresponding stresses of the power cable components are obtained by modelling the cable cross-section in UFLEX. Figure 5-8 shows the stresses caused by cable tension. For both components, the stresses increase linearly with higher applied tensions. The armor steel wires have slightly higher tension-induced stress compared to the copper wires. Figure 5-9 shows the curvature-stress relationships for the power cable components. For larger bending, the curvature-induced stresses increase linearly. However, the armor steel wires have significantly higher stresses than the copper wires. A small axial tension of 1 kN is applied to facilitate the simulations with the different curvatures. The results of this study indicate that under the investigated combinations of tension and curvature loading, the applied tension has a negligible impact on curvature-induced stresses. However, it should be noted that this observation is valid for low tension levels examined in this study. The obtained relationships are used to determine the fatigue life based on the tension and curvature results of the dynamic analyses.

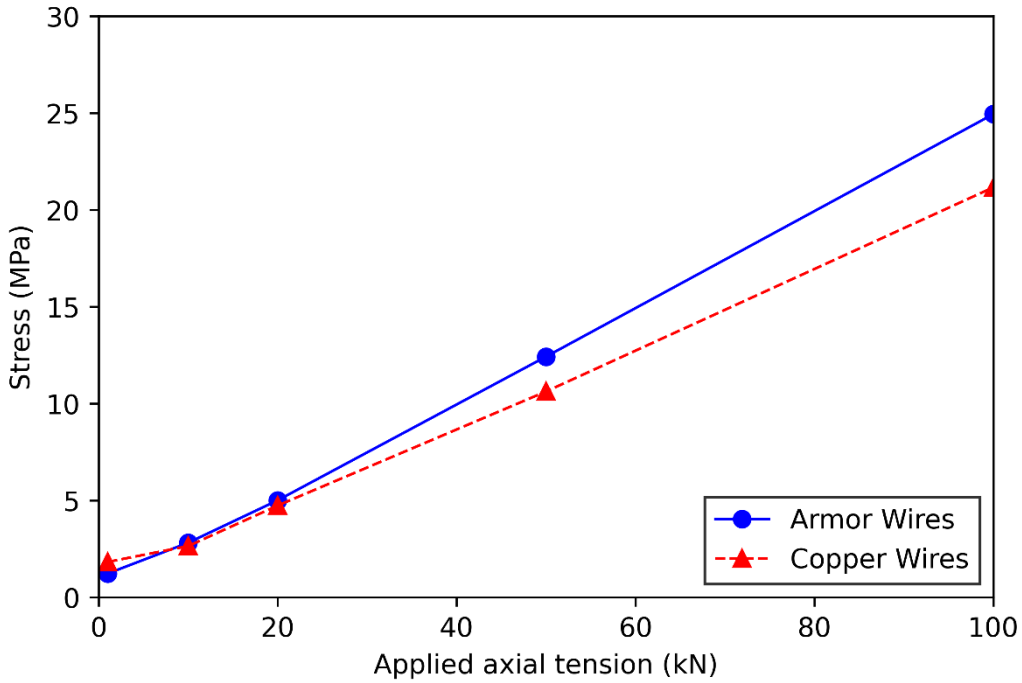

Figure 5-8: Tension-Stress relationship for the power cable components.

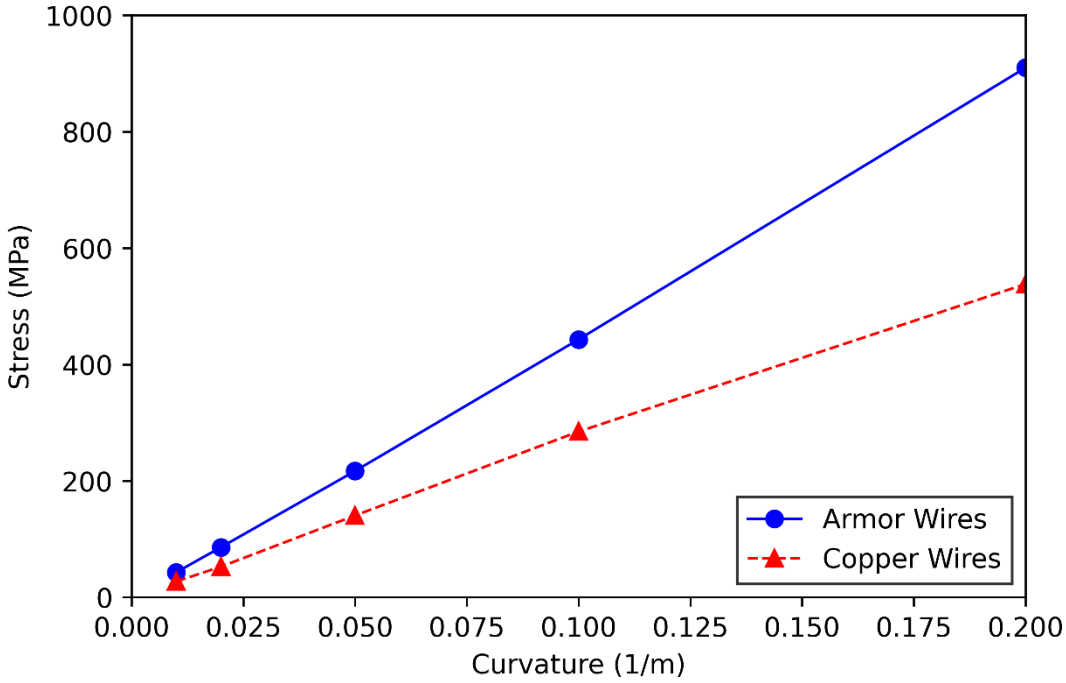

Figure 5-9: Curvature-Stress relationship for the power cable components.

5.3.2 Fatigue Life of the Power Cable between two Spar FOWTs

Table 5-9 lists the results of the fatigue analysis for the setup with 10 buoys in the SOL state. The critical cable components governing the fatigue damage are the armor wires. The most critical location is close to one of the buoys, directly outside the bend stiffener. Figure 5-10 shows the fatigue life along the power cable for the two different cable components. It can be observed that the fatigue life is always lowest in proximity of the buoys, while it is highest in the areas within the bend stiffeners. Upon examining the impact of various environmental factors, it becomes evident that Direction 1 results in the highest fatigue damage at the critical location. Moreover, more severe environmental conditions, characterized by stronger wind, wave, and current loads, have a greater influence on fatigue damage than milder cases.

Table 5-9: Fatigue analysis results for the power cable with 10 buoys in the SOL state.

Minimum Fatigue Life (Years)	Critical Component	Location (m)	Location (Angle)
85.57	Armor Wires	962.7	157.5°

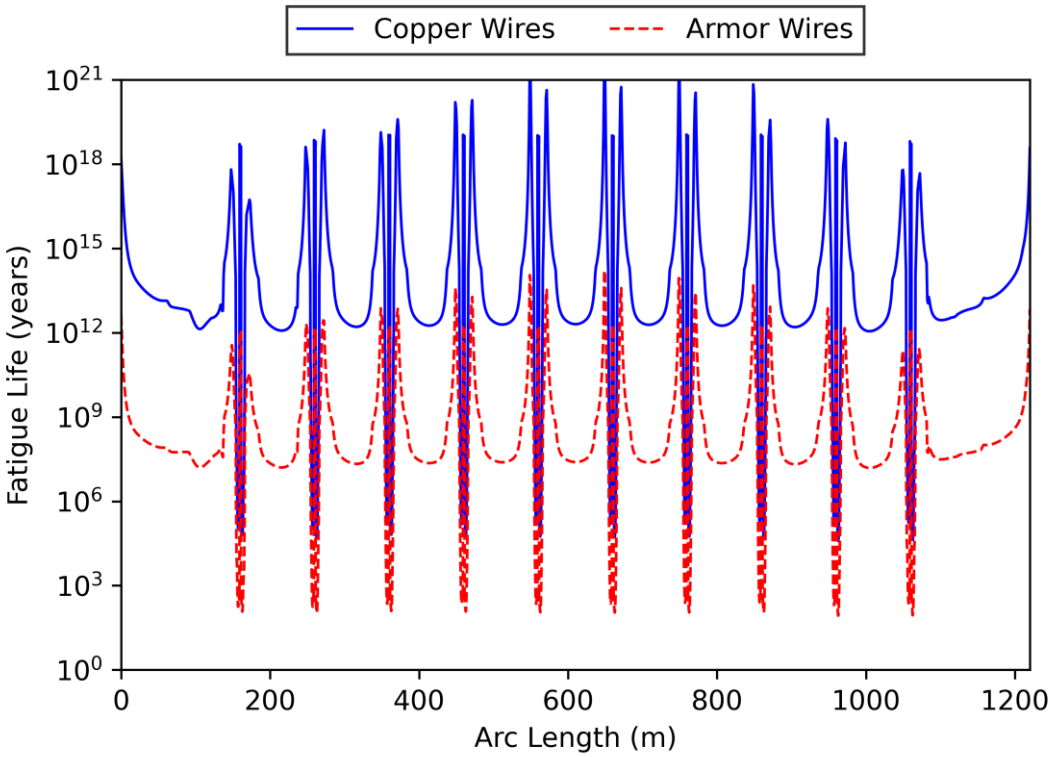

Figure 5-10: Fatigue life along the power cable with 10 buoys in the SOL state.

The following part analyzes the contributors leading to fatigue damage. Figure 5-11 shows the curvatures along the power cable during the simulation of EC5 and Direction 1. The curvatures are highest close to the buoys, and the differences between the minimum and maximum curvatures seem to be small. Figure 5-12 shows the curvatures along the cable in the area with the lowest fatigue life for the same load case. The range of curvatures occurring during the simulation is largest at the location of the highest fatigue damage. Figure 5-13 shows the effective tensions along the power cable for the same simulation case. The tensions are largest at the hang-off points, and the differences between the minimum and maximum tensions are similar along the entire cable. These patterns are the same for all performed simulations. Therefore, bending-induced stresses seem to be the main factor causing power cable fatigue in this setup, while the contribution of the effective cable tension seems to be small.

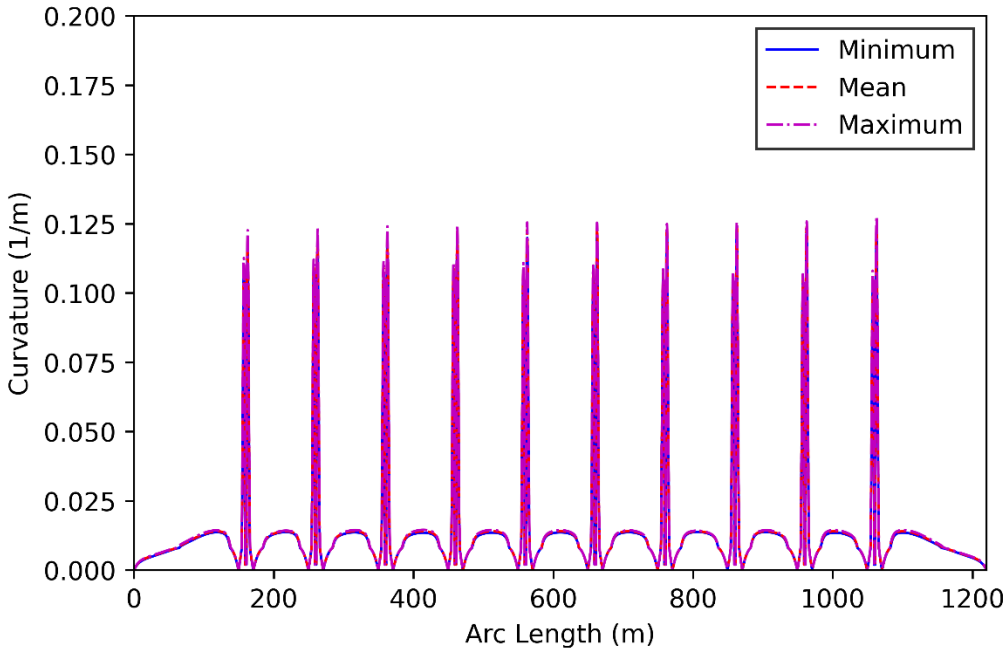

Figure 5-11: Curvature along the power cable for EC5 and Direction 1.

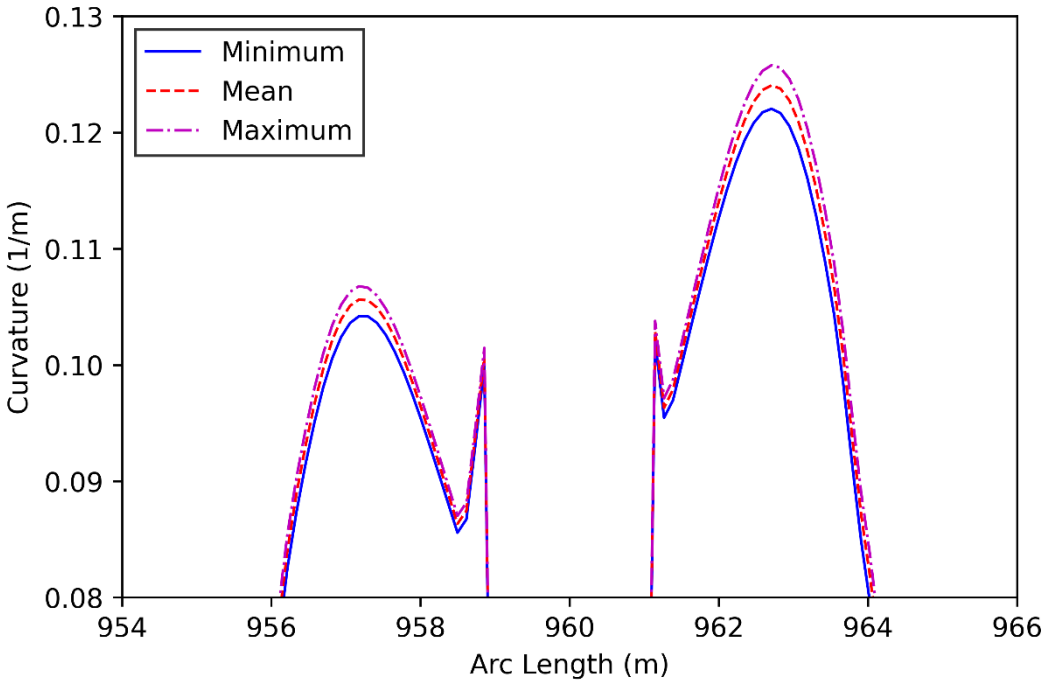

Figure 5-12: Curvature envelope in the area with the lowest fatigue life for EC5 and Direction 1.

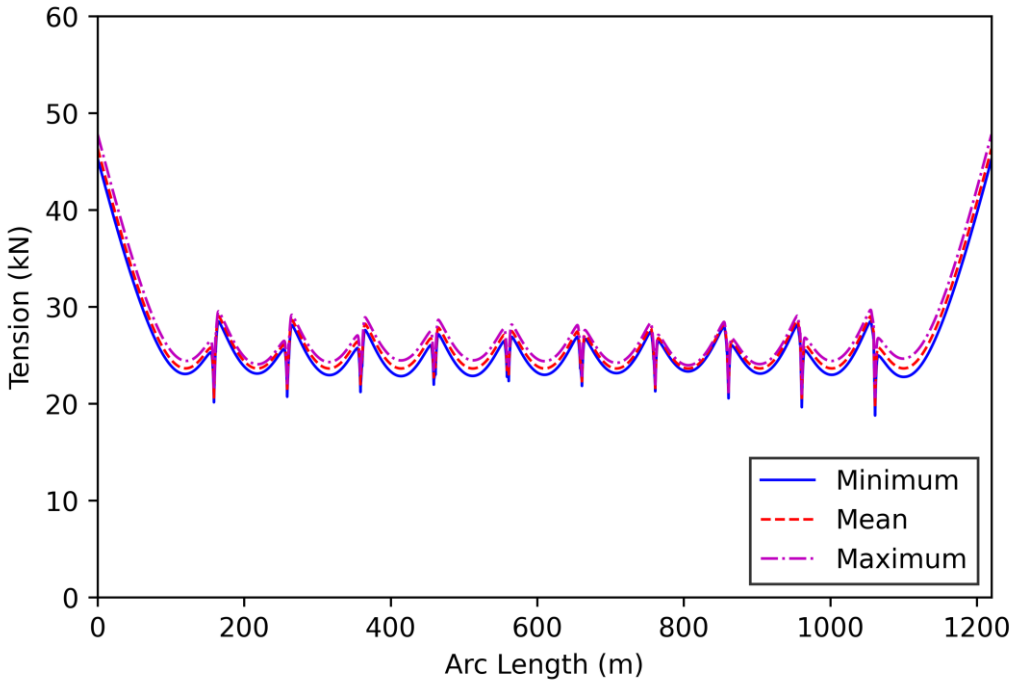

Figure 5-13: Effective tension along the power cable for EC5 and Direction 1.

5.3.3 Influence of the Marine Growth State on the Fatigue Life

In this section, the influence of the marine growth state on the fatigue life of the power cable is investigated. Table 5-10 lists the results of the fatigue analysis in the EOL state. The largest fatigue damage occurs at exactly the same location as observed for the SOL state. However, the fatigue life is reduced by one-third due to the marine growth effects. The heavier cable leads to larger sag bends between the buoys, and the increased external diameter causes more motion due to wave and current loads. These two factors result in the reduction of the expected power cable lifetime. Figure 5-14 shows the fatigue life along the power cable for the copper and armor wires. Along the entire cable, the armor wires are the critical components. The fatigue lives for the SOL and the EOL states follow the same pattern.

Table 5-10: Fatigue analysis results for the power cable with 10 buoys in the EOL state.

Minimum Fatigue Life (Years)	Deviation to the SOL state	Critical Component	Location (m)	Location (Angle)
56.04	-34.5%	Armor Wires	962.7	157.5°

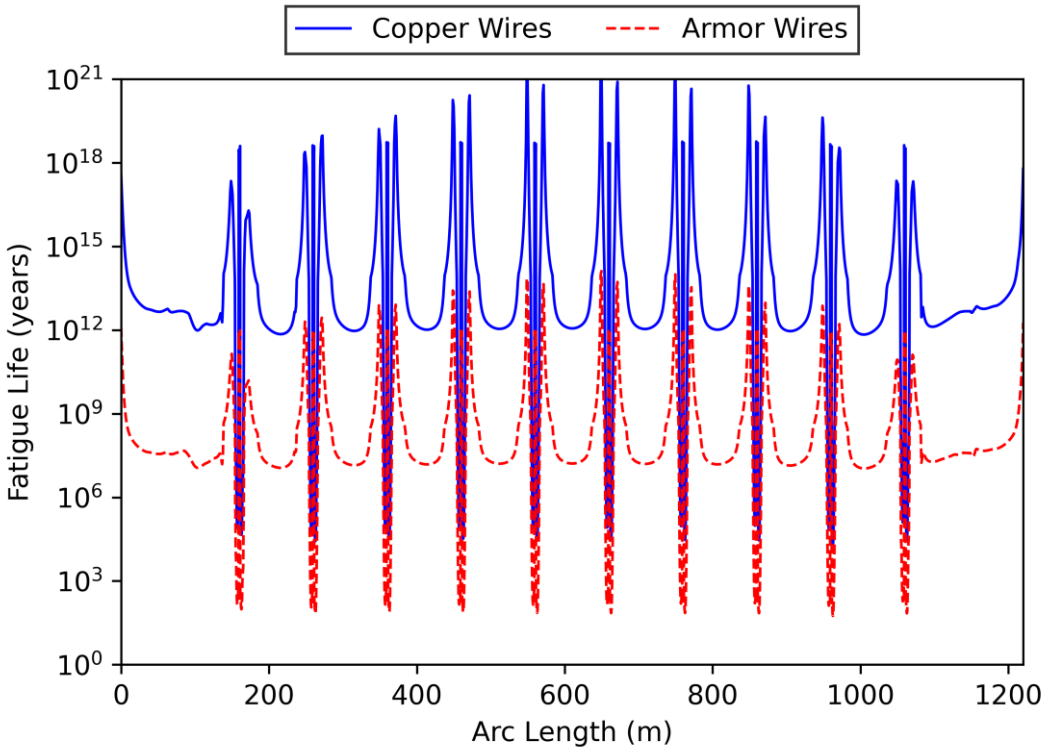

Figure 5-14: Fatigue life along the power cable with 10 buoys in the EOL state.

5.3.4 Influence of the Cable Configuration on the Fatigue Life

This section evaluates the influence of the number of buoys on the fatigue life of the suspended power cable. Table 5-11 lists the results of the fatigue analysis of the setup with 9 buoys. The fatigue life increases significantly compared to the results obtained for the 10-buoy setup. The location of the largest fatigue damage has changed due to the different setups, but it is still located next to the second outermost buoy. The armor wires remain the critical component governing the fatigue life. Figure 5-15 shows the fatigue life along the power cable. The minimum fatigue life consistently appears near the buoys, coinciding with the locations in the 10-buoy configuration. The increased fatigue life in configurations with fewer buoys can be attributed to reduced cable curvature and a smaller range of curvature. Figure 5-16 illustrates the curvature envelope at the most critical location for the 9-buoy setup. When comparing curvature envelopes in the areas with the lowest fatigue life of the 10-buoy and 9-buoy setups, as shown in Figure 5-17, the decreased mean curvature and curvature range are clearly visible. However, a larger number of buoys reduces the maximum tension of the inter-array power cable. Figure 5-18 shows the maximum tensions along the power cable for the two different setups. These results align with the findings of Ahmad et al. (2023) and Beier et al. (2023a). Consequently, when choosing a suspended power cable configuration, a balance must be struck between the axial tension that could result in ultimate limit state failures and the curvature that may cause fatigue damage.

Table 5-11: Fatigue analysis results for the power cable with 9 buoys in the SOL state.

Minimum Fatigue Life (Years)	Deviation to the 10 buoys setup	Critical Component	Location (m)	Location (Angle)
440.18	+414.4%	Armor Wires	912.5	180°

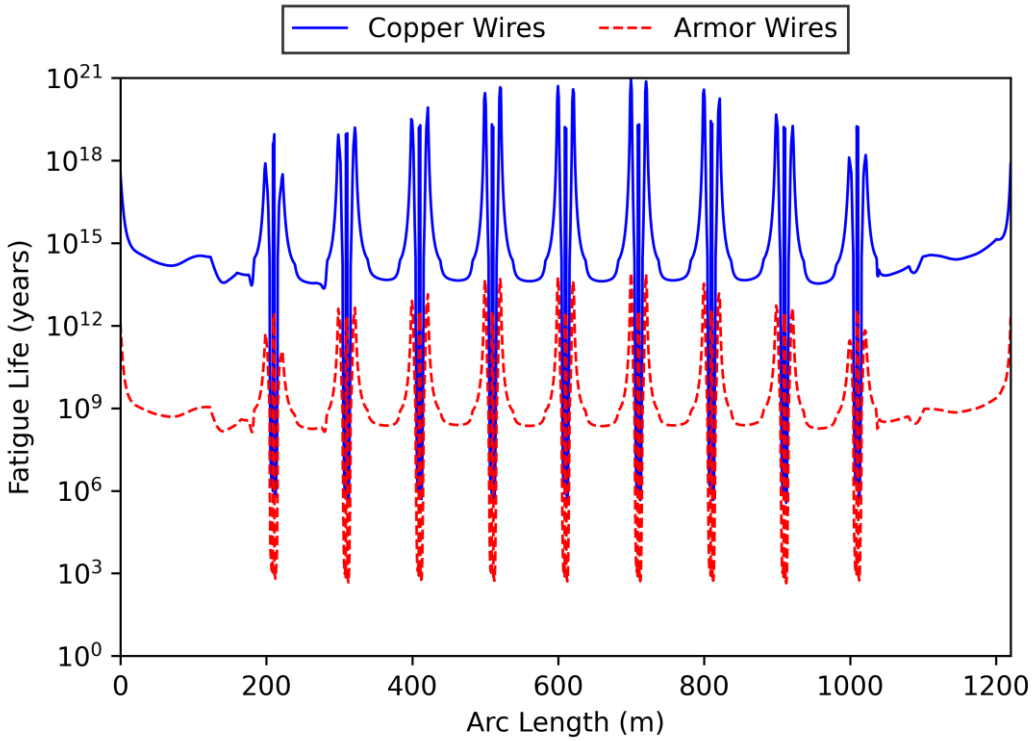

Figure 5-15: Fatigue life along the power cable with 9 buoys in the SOL state.

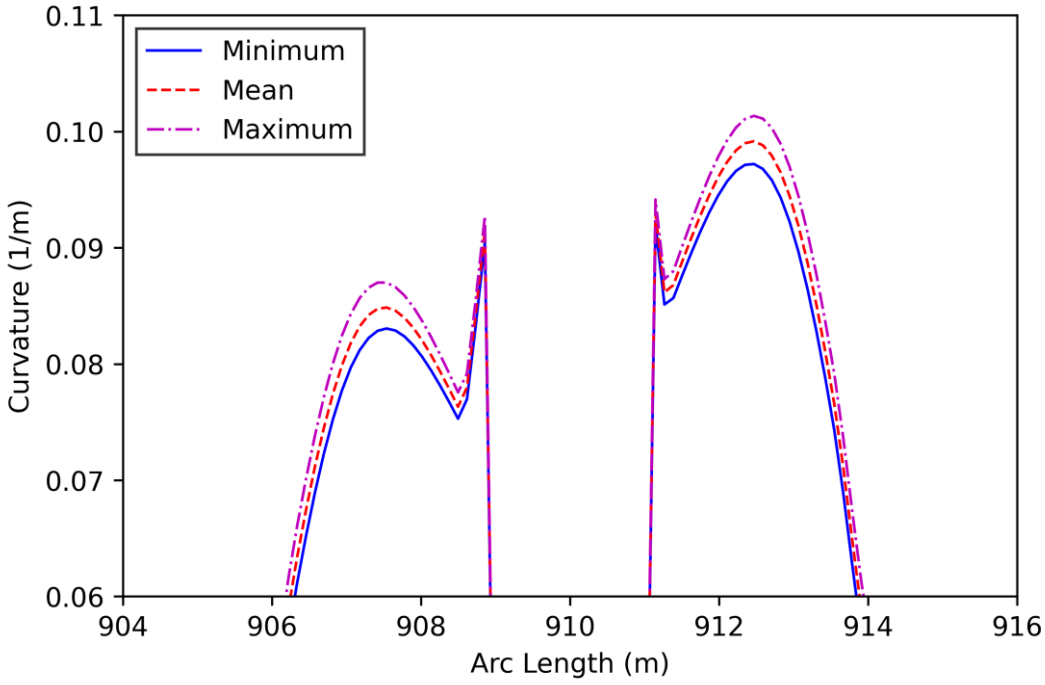

Figure 5-16: Curvature envelope in the area with the lowest fatigue life of the 9-buoy setup for EC5 and Direction 1.

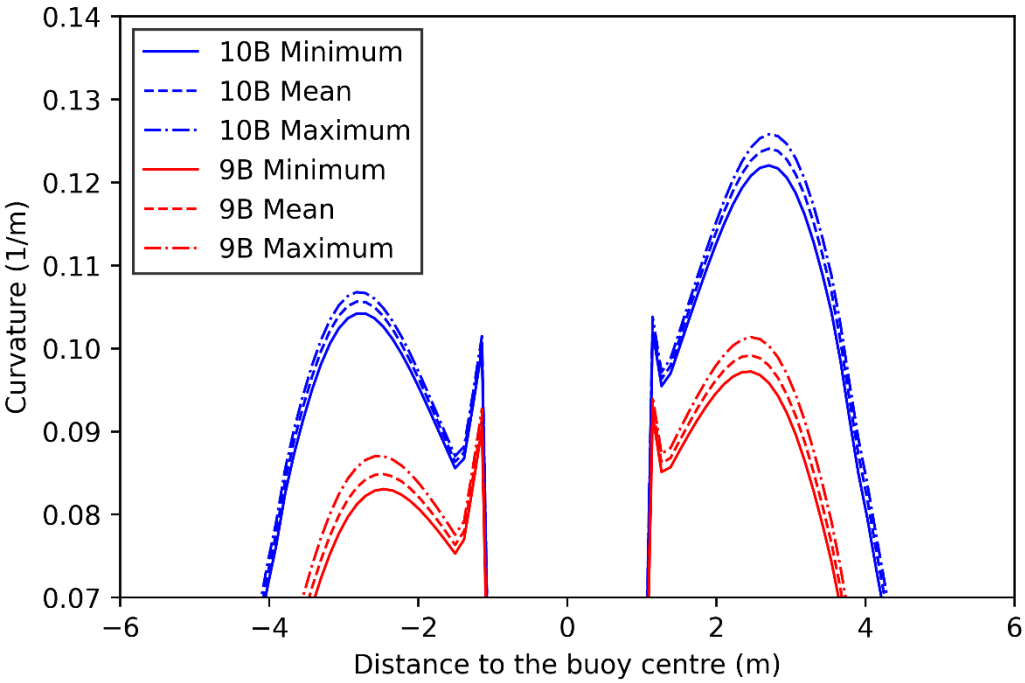

Figure 5-17: Comparison of curvature envelopes in the areas with the lowest fatigue life of the 10-buoy and 9-buoy setups for EC5 and Direction 1.

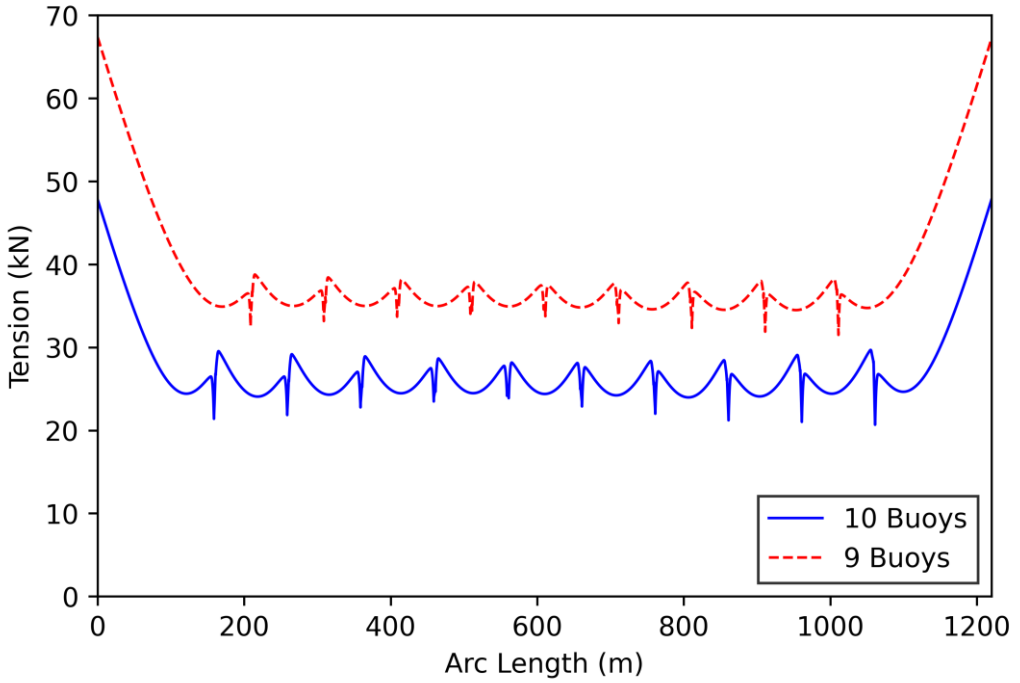

Figure 5-18: Comparison of the maximum tensions for EC5 and Direction 1.

5.3.5 Influence of the FOWT type on the Fatigue Life

The OC3-Hywind spar FOWTs are replaced with semi-submersible CSC FOWTs to evaluate the impact of the floater type on the fatigue behavior of the suspended power cable. Table 5-12 lists the outcomes of the fatigue analysis for the setup with the semi-submersible platforms. Compared to the spar setup, the power cable's fatigue life improves substantially, with the critical location now situated near the buoy closest to the FOWT. The armor wires remain the critical component in this configuration as well. **Fehler! Verweisquelle konnte nicht gefunden werden.**19 illustrates the fatigue life distribution along the power cable, revealing a consistent pattern concerning areas with the most significant fatigue damage, as seen in other fatigue calculations. This setup results in a mean curvature approximately equal to that of the spar setup, and an even broader curvature range at the critical location, as demonstrated in **Fehler! Verweisquelle konnte nicht gefunden werden.**20. The enhanced fatigue life in the semi-submersible setup can be attributed to the fewer large-amplitude load cycles, stemming from the distinct floater motions. **Fehler! Verweisquelle konnte nicht gefunden werden.**21 presents the time history of cable curvature at the critical locations for different FOWT types. It is evident that the spar setup results in greater curvature amplitude cycles compared to the semi-submersible setup.

Table 5-12: Fatigue analysis results for the power cable connecting two CSC FOWTs.

Minimum Fatigue Life (Years)	Deviation to the spar setup	Critical Component	Location (m)	Location (Angle)
235.22	+174.9%	Armor Wires	1062.7	180°

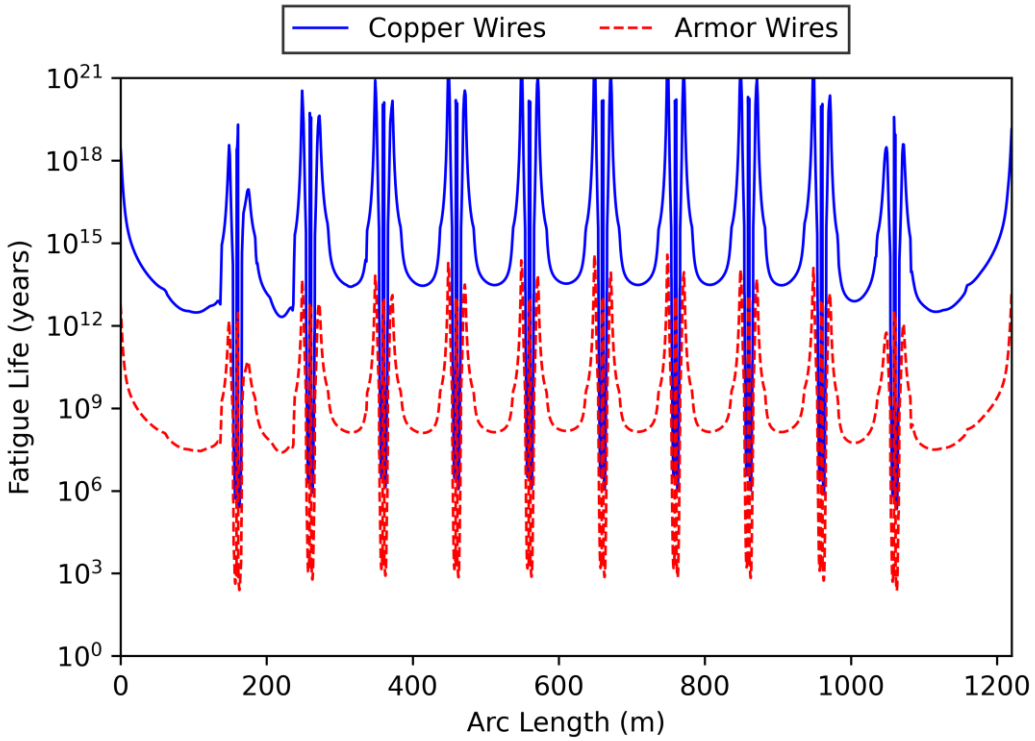

Figure 5-19: Fatigue life along the power cable between two CSC FOWTs.

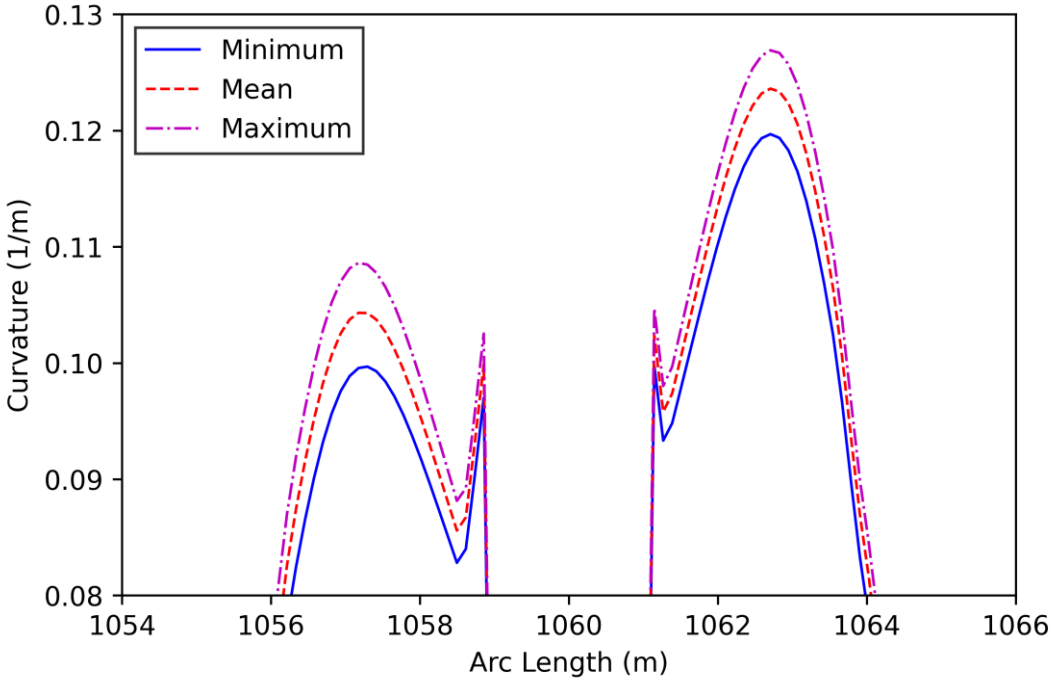

Figure 5-20: Curvature envelope in the area with the lowest fatigue life of the CSC setup for EC5 and Direction 1.

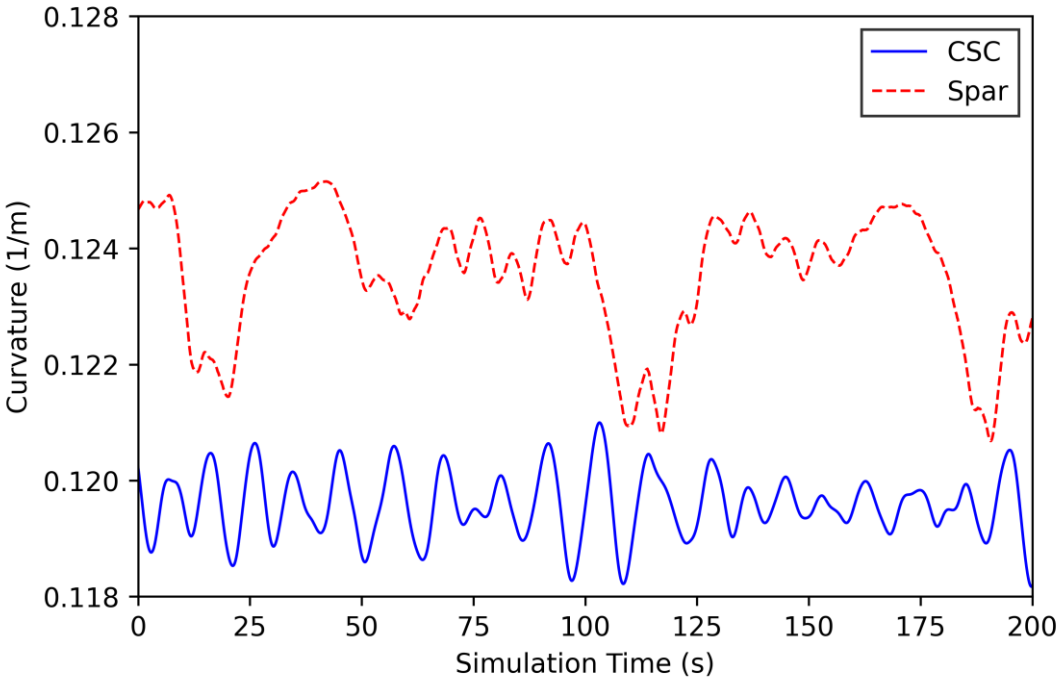

Figure 5-21: Curvature time history for the most critical locations of the different setups for EC3 and Direction 1.

5.4 Conclusion

A suspended inter-array power cable connecting two FOWTs is modelled in OrcaFlex. The curvature-stress and tension-stress relationships of the power cable are determined in UFLEX. The fatigue life is calculated for a base configuration between two spar FOWTs. The contributors leading to the fatigue damage are investigated. Setups including marine growth effects, a different number of attached buoys, and semi-submersible instead of spar platforms are created, and the influence of these parameters on the fatigue life of the suspended power cable is investigated. The main conclusions obtained by the present study are summarized below:

- In this study, the base configuration of the suspended inter-array power cable demonstrates adequate durability for typical design life (20 – 25 years) under the given environmental conditions. Fatigue damage is the most critical near the subsea buoys. The armor wires are the critical component governing the fatigue life of the power cable investigated in the present study.
- Curvature is identified as the primary factor contributing to fatigue damage, with the location exhibiting the highest curvature range also having the lowest fatigue life. The Direction 1 (cross-flow) results in the highest fatigue damage across all load cases, and fatigue damage intensifies with harsher environmental conditions.
- Marine growth on the power cable over its lifespan reduces the fatigue life of the base configuration by approximately 30%. The critical location and component remain the same as in the SOL setup.
- Decreasing the number of buoys connected to the suspended power cable significantly enhances its fatigue life. However, fewer buoys also lead to increased axial tensions. Thus, a compromise between fewer buoys (reducing curvature and fatigue damage) and more buoys (minimizing maximum tensions) is necessary in the suspended power cable design.
- Replacing the OC3-Hywind spar FOWTs with semi-submersible CSC FOWTs increases the fatigue life of the suspended power cable by around 170%. The extended fatigue life is due to fewer large amplitude load cycles resulting from different floater motions. The tensions and curvatures for the two different floater setups are very similar.

Acknowledgments

The authors acknowledge The Research Council of Norway and the industry partners of ImpactWind SouthWest – RCN project number 332034 – for their support.

Chapter 6 - Conclusions

Dynamic responses of suspended inter-array power cables connecting FOWTs are analyzed with regards to the influence on cable effective tensions, curvatures, horizontal and vertical excursions of the cable as well as the power cable fatigue life. The present study is performed in three stages. First, the most suitable suspended power cable configuration between two spar FOWTs is determined using an optimization criterion called Fitness Factor. Several configurations with different numbers of buoys, buoy spacings and power cable lengths are evaluated, and the marine growth effects are included in the analysis. Static analyses are carried out to check the seabed and sea surface clearances as well as the maximum tensions and curvatures that are included in the Fitness Factors. For the three best configurations completing the static analysis, dynamic analyses are performed for different environmental conditions and load directions. Again, the different configurations are assessed based on their Fitness Factors to determine the optimum cable setup. The main conclusions from this power cable configuration study are summarized below:

- A larger number of buoys attached to the power cable seems to reduce the effective tension in the cable. The impact of the cable length on tensions and curvatures is very small. For the power cable used in the present study, the MBR is less critical than the maximum tension.
- The spacing of the buoys determines whether the cable touches the seabed, floats fully submerged, or floats on the sea surface. A spacing of 100 m leads to the best results for the considered setup for all investigated buoy arrangements.
- The case with the harshest environmental conditions is the most critical load case since the larger current load and more floater motions directly affect the power cable. Direction 3 (inline flow) results in the largest tensions and the smallest bending radii.
- Considering the marine growth on the power cable, the differences between the cables in the SOL and EOL states are small. EOL state simulations yield slightly larger maximum tensions, while SOL state simulations result in smaller minimum bending radii.

The second stage of this study investigates the application of suspended power cables in different floating wind farms. The cable configuration determined in the first stage is used between two semi-submersible FOWTs as well as in wind farms consisting of three and four spar FOWTs. The main findings of the analysis of the application of power cables in floating wind farms are listed below:

- Comparing the results of the simulations with the different floater types, the cable tensions and curvature are very similar for the OC3-Hywind spar FOWT and the CSC semi-submersible FOWT. Between these two setups, the results differ slightly close to the hang-off points, while the cable behavior in the remaining part is nearly identical. Therefore, a cable proven suitable for one FOWT type can probably also be installed for another FOWT type.
- Regarding the application of suspended power cables in entire offshore wind farms, the behaviors of a cable under the same environmental condition and load direction in a multiple FOWT wind farm layout and an analogous cable in a two FOWT layout are almost identical. Moreover, parallel cables connecting FOWTs in a rectangular wind farm show the same motion responses. Therefore, array effects seem to be negligible for the suspended power cable design and performing simulations of the setup between two FOWTs for different loading directions and conditions is considered representative of entire wind farms as it provides conservative estimates of the maximum effective tensions and the MBR in the power cable.

As the last stage of the present study fatigue analyses of the power cable for different setups are performed. The influences of the marine growth state, the number of buoys attached to the cable and the floater type on the fatigue life are evaluated. Six different environmental conditions and three load directions are included in the investigation. The power cable stresses are determined through tension-stress and curvature-stress relationships and the Rainflow Counting method is used to determine the fatigue damage. The main conclusions from the fatigue assessment are summarized below:

- The optimum suspended inter-array power cable configuration determined in the first stage of this study survives a sufficient number of years under the applied environmental conditions. The largest fatigue damage occurs next to the subsea buoys and the armor wires are identified as the critical component for the used power cable.

- The main contributor to fatigue damage is curvature. The location where the largest curvature range occurs is identical to the location where the lowest fatigue life occurs.
- Direction 1 (cross-flow) leads to the largest fatigue damage for all load cases, and the fatigue damage is increasing for harsher environmental conditions.
- Marine growth effects on the power cable reduce the fatigue life by around 30%. The analyses of the setups with and without marine growth lead to the same critical locations and critical components (e.g. the armor wires).
- A reduction in the number of buoys attached to the suspended power cable increases the fatigue life significantly in the limit of the investigated configurations. However, as stated previously, fewer buoys also cause higher axial tensions. Therefore, a compromise between fewer buoys reducing the curvature as well as the fatigue damage and more buoys reducing the maximum tensions is necessary for the suspended power cable design.
- Using semi-submersible CSC FOWTs instead of OC3-Hywind spar FOWTs increases the fatigue life of the suspended power cable by around 170%. A reduced amount of large amplitude load cycles due to the different floater motions is identified as the reason for the higher fatigue life.

Chapter 7 - Recommendations for Future Work

The present study focuses on the different parameters affecting the dynamic response and the fatigue life of a suspended inter-array power cable in floating offshore wind farms. Further studies can be performed to extend the research on this topic. In the following, some recommendations for future works related to this topic are summarized:

- The motions affecting the power cable are dependent on the location of the hang-off point along the vertical axis of the spar platform. To find the best setup, different power cable hang-off points and their influence on the power cable tensions, curvatures and fatigue life can be investigated.
- Different failure scenarios of the suspended power cable setup can be evaluated, for example if the connection of one buoy to the power cable gets lost.
- An overall Fitness Factor can be developed, considering both the maximum effective tension and MBR as well as the fatigue life of the suspended power cable.
- A detailed fatigue analysis can be performed including more environmental cases and load directions. Also, different occurrence probabilities for each load case can be considered.
- A cost analysis can be done to determine the benefits of a suspended inter-array power cable configuration to a configuration with a static cable laid on the seabed for different water depths.

References

Ahmad, I. B., Schnepf, A., & Ong, M. C. (2023). An optimisation methodology for suspended inter-array power cable configurations between two floating offshore wind turbines. *Ocean Engineering*, *278*, 114406. https://doi.org/10.1016/j.oceaneng.2023.114406

ASTM International. (2011). *Practices for Cycle Counting in Fatigue Analysis*. https://doi.org/10.1520/E1049-85R11E01

Bakken, K. (2019). Fatigue of Dynamic Power Cables Applied in Offshore Wind Farms. *Master Thesis, NTNU*.

Ballard, B., Yu, Y.-H., Rij, J. V., & Driscoll, F. (2020). Umbilical Fatigue Analysis for a Wave Energy Converter. *OMAE 2020*.

Beier, D., Ong, M. C., Janocha, M. J., & Ye, N. (2023a). Application of a Suspended Inter-Array Power Cable in Floating Offshore Wind Farms. *Under Review*.

Beier, D., Schnepf, A., Van Steel, S., Ye, N., & Ong, M. C. (2023b). Fatigue Analysis of Inter-array Power Cables between Two Floating Offshore Wind Turbines Including a Simplified Method to Estimate Stress Factors. *Under Review*.

Crown Estate Scotland. (2023). *ScotWind offshore wind leasing delivers major boost to Scotland's net zero aspirations*. https://www.crownestatescotland.com/news/scotwind-offshore-wind-leasing-delivers-major-boost-to-scotlands-net-zero-aspirations

DNV. (2010). *DNV-RP-C205: Environmental Conditions and Environmental Loads*.

DNV GL AS. (2014). *DNVGL-RP-0005 RP-C203: Fatigue design of offshore steel structures*.

Dowling, N. E. (2012). *Mechanical behavior of materials: Engineering methods for deformation, fracture, and fatigue*. Pearson Education.

Eldøy, S. (2017). *Hywind Scotland Pilot Park Project Plan for Construction Activities*.

Equinor ASA. (2009). *StatoilHydro inaugurates floating wind turbine*. https://www.equinor.com/news/archive/2009/09/08/InnovativePowerPlantOpened

Equinor ASA. (2019). *PUD Hywind Tampen*.

ESDU. (2007). *ESDU 80025: Mean forces, pressures and flow field velocities for circular cylindrical structures: Single cylinder with two-dimensional flow.*

GWEC Global Wind Energy Council. (2022a). *Floating Offshore Wind Report 2022—A Global Opportunity*.

GWEC Global Wind Energy Council. (2022b). *GLOBAL OFFSHORE WIND REPORT 2022*.

Hansen, M. O. L. (2015). *Aerodynamics of wind turbines*. Routledge.

Hasselmann, K., Barnett, T. P., Bouws, E., Carlson, H., & Hasselmann, D. E. (1973). Measurements of Wind-Wave Growth and Swell Decay during the Joint North Sea Wave Project (JONSWAP). In *Ergaenzungsheft zur Deutschen Hydrographischen Zeitschrift Reihe A (8), Nr. 12*.

Hu, H., Yan, J., Sævik, S., Ye, N., Lu, Q., & Bu, Y. (2022). Nonlinear bending behavior of a multilayer copper conductor in a dynamic power cable. *Ocean Engineering*, *250*. https://doi.org/10.1016/j.oceaneng.2022.110831

Ikhennicheu, U., Lynch, M., Doole, S., Borisade, F., Wendt, F., Schwarzkopf, M.-A., Matha, D., Vicente, R. D., Tim, H., Ramirez, L., & Potestio, S. (2020). *D3.1 Review of the state of the art of dynamic cable system design*.

Jonkman, J. (2010). *Definition of the Floating System for Phase IV of OC3* (NREL/TP-500-47535, 979456; p. NREL/TP-500-47535, 979456). https://doi.org/10.2172/979456

Jonkman, J., Butterfield, S., Musial, W., & Scott, G. (2009). *Definition of a 5-MW Reference Wind Turbine for Offshore System Development* (NREL/TP-500-38060, 947422; p. NREL/TP-500-38060, 947422). https://doi.org/10.2172/947422

Jonkman, J., Hayman, G. J., Jonkman, B. J., Damiani, R. R., & Murray, R. E. (2017). AeroDyn v15 User's Guide and Theory Manual. *Renewable Energy*.

Jonkman, J., & Musial, W. (2010). Offshore Code Comparison Collaboration (OC3) for IEA Task 23 Offshore Wind Technology and Deployment. *Renewable Energy*, 74.

Journée, J. M. J., & Massie, W. W. (2001). *Offshore Hydromechanics*. Delft University of Technology.

Karlsen, S., Slora, R., Heide, K., Lund, S., Eggertsen, F., & Osborg, P. A. (2009). Dynamic Deep Water Power Cables. *RAO / CIS OFFSHORE*.

Kauzlarich, J. J. (1989). The Palmgren-Miner rule derived. In *Tribology Series* (Vol. 14, pp. 175–179). Elsevier. https://doi.org/10.1016/S0167-8922(08)70192-5

Luan, C., Gao, Z., & Moan, T. (2016). Design and Analysis of a Braceless Steel 5-MW Semi-Submersible Wind Turbine. *Volume 6: Ocean Space Utilization; Ocean Renewable Energy*, V006T09A052. https://doi.org/10.1115/OMAE2016-54848

Marta, M., Mueller-Schuetze, S., Ottersberg, H., Isus Feu, D., Johanning, L., & Thies, P. R. (2015). *Development of dynamic submarine MV power cable design solutions for floating offshore renewable energy applications*.

Nasution, F. P., Sævik, S., & Gjøsteen, J. K. Ø. (2012). Fatigue Analysis of Copper Conductor for Offshore Wind Turbines by Experimental and FE Method. *Energy Procedia*, *24*, 271–280. https://doi.org/10.1016/j.egypro.2012.06.109

Nasution, F. P., Sævik, S., & Gjøsteen, J. K. Ø. (2014). Finite element analysis of the fatigue strength of copper power conductors exposed to tension and bending loads. *International Journal of Fatigue*, *59*, 114–128. https://doi.org/10.1016/j.ijfatigue.2013.09.009

Nielsen, F. G. (2017). *Hywind – From idea to world's first wind farm based upon floaters*. https://www.uib.no/sites/w3.uib.no/files/attachments/hywind_energy_lab.pdf

Norwegian Petroleum Directorate (NPD). (1995). *Regulations relating to loadbearing structures in the petroleum activities*.

Olje- og energidepartementet. (2023). *Regjeringen går videre i sin satsing på havvind*. https://www.regjeringen.no/no/aktuelt/regjeringen-gar-videre-i-sin-satsing-pa-havvind/id2949762/

Orcina Ltd. (2022). *OrcaFlex*. https://www.orcina.com/webhelp/OrcaFlex/

Principle Power Inc. (2022). *WindFloat Atlantic*. https://www.principlepower.com/projects/windfloat-atlantic

Principle Power Inc. (2023). *Kincardine Offshore Wind Farm*. https://www.principlepower.com/projects/kincardine-offshore-wind-farm

Ramachandran, G. K. V., Robertson, A., Jonkman, J. M., & Masciola, M. D. (2013). *Investigation of Response Amplitude Operators for Floating Offshore Wind Turbines: Preprint*. 10.

Rapha, J. I., & Domínguez, J. L. (2021). Suspended cable model for layout optimisation purposes in floating offshore wind farms. *Journal of Physics: Conference Series*, *2018*(1). https://doi.org/10.1088/1742-6596/2018/1/012033

Rentschler, M. U. T., Adam, F., & Chainho, P. (2019). Design optimization of dynamic inter-array cable systems for floating offshore wind turbines. *Renewable and Sustainable Energy Reviews*, *111*, 622–635. https://doi.org/10.1016/j.rser.2019.05.024

Rentschler, M. U. T., Adam, F., Chainho, P., Krügel, K., & Vicente, P. C. (2020). Parametric study of dynamic inter-array cable systems for floating offshore wind turbines. *Marine Systems & Ocean Technology*, *15*(1), 16–25. https://doi.org/10.1007/s40868-020-00071-7

Sævik, S., & Bruaseth, S. (2005). Theoretical and experimental studies of the axisymmetric behaviour of complex umbilical cross-sections. *Applied Ocean Research*, *27*(2), 97–106. https://doi.org/10.1016/j.apor.2005.11.001

Sarpkaya, T. "Sarp." (2010). *Wave Forces on Offshore Structures* (1st ed.). Cambridge University Press. https://doi.org/10.1017/CBO9781139195898

Schaffarczyk, A. (2014). Aerodynamics and Blade Design. In A. Schaffarczyk (Ed.), *Understanding Wind Power Technology* (pp. 126–161). John Wiley & Sons, Ltd. https://doi.org/10.1002/9781118701492.ch4

Schnepf, A., Lopez-Pavon, C., Devulder, A., Johnsen, Ø., & Ong, M. C. (2022, June). Suspended Power Cable Configurations For Floating Offshore Wind Turbines In Deep Water Powering An FPSO. *OMAE2022-80071*. OMAE2022.

Schnepf, A., Lopez-Pavon, C., Ong, M. C., Yin, G., & Johnsen, Ø. (2023). Feasibility study on suspended inter-array power cables between two spar-type offshore wind turbines. *Ocean Engineering*, *277*, 114215. https://doi.org/10.1016/j.oceaneng.2023.114215

Shi, L., Yang, W., Chen, K., Yu, G., Jin, C., Ni, L., Jing, B., & Hu, Z. (2022). Performance Evaluation of W Shape Dynamic Inter-Array Cable Configuration for Floating Offshore Wind Turbine. *Day 2 Wed, March 23, 2022*, D021S013R002. https://doi.org/10.4043/31344-MS

SINTEF. (2018). *Uflex2D Version 2.8 Theory Manual*.

Spraul, C., Arnal, V., Cartraud, P., & Berhault, C. (2017). Parameter Calibration in Dynamic Simulations of Power Cables in Shallow Water to Improve Fatigue Damage Estimation. *Volume 3A: Structures, Safety and Reliability*, V03AT02A037. https://doi.org/10.1115/OMAE2017-61821

Srinil, N. (2016). Cabling to connect offshore wind turbines to onshore facilities. In *Offshore Wind Farms* (pp. 419–440). Elsevier. https://doi.org/10.1016/B978-0-08-100779-2.00013-1

Standards Norway. (2007). *NORSOK N-003—Actions and action effects*.

Svensson, G. (2020). Fatigue prediction models of Dynamic Power Cables by laboratory testing and FE analysis. *Master Thesis, NTNU*.

Thies, P. R., Harrold, Johanning, L., Grivas, K., & Georgallis, G. (2019). *Load and fatigue evaluation for 66 kV floating offshore wind submarine dynamic power cable*.

Thies, P. R., Johanning, L., & Smith, G. H. (2012). Assessing mechanical loading regimes and fatigue life of marine power cables in marine energy applications. *Proceedings of the Institution of Mechanical Engineers, Part O: Journal of Risk and Reliability*, *226*(1), 18–32. https://doi.org/10.1177/1748006X11413533

United Nations. (2015). *Paris Agreement*.

Vaz, M. A., de Lemos, C. A. D., & Caire, M. (2007). A Nonlinear Analysis Formulation for Bend Stiffeners. *Journal of Ship Research*, *51*(03), 250–258. https://doi.org/10.5957/jsr.2007.51.3.250

Ye, N., & Yuan, Z. (2020). On Modelling Alternatives of Non-critical Components in Dynamic Offshore Power Cables. *Proceedings of the Thirtieth (2020) International Ocean and Polar Engineering Conference Shanghai, China*.

Zhao, S., Cheng, Y., Chen, P., Nie, Y., & Fan, K. (2021). A comparison of two dynamic power cable configurations for a floating offshore wind turbine in shallow water. *AIP Advances*, *11*(3). https://doi.org/10.1063/5.0039221